אוניברסיטת תל אביב

Tel-Aviv University

Computational investigation of selected human ion channels

Thesis submitted for the Degree “Doctor of Philosophy” by

Yana Gofman

Submitted to the senate of Tel-Aviv University

May 2012

This work was carried out under the supervision of

Prof. Nir Ben-Tal

Acknowledgments

I would like to express my gratitude to all who helped on the research for my thesis.

Special thanks to my supervisor, Prof. Nir Ben-Tal, whose support, knowledge and patience throughout all stages of my work were essentially limitless.

Thanks to Prof. Turkan Haliloglu for her careful and pleasant guidance.

Thanks to Prof. Bernard Attali for his kindness and support.

Thanks to all the current and the former members of the Ben-Tal lab.

Thanks to all the current and the former members of the Attali lab.

Thanks to the members of my doctoral accompanying committee: Dr. Joel Hirsch, Prof. Ilana Lotan and Prof. Nathan Dascal.

Table of contents

Abstract

The voltage-gated-like (VGL) ion channels superfamily is one of the largest groups of signal transduction proteins. Each member of the superfamily contains a pore domain with a unique architecture; some members also feature regulatory domains that respond to the changes in membrane voltage, intracellular signaling molecules, or other stimuli. In addition, the activity of the ion channels can be modulated by regulatory proteins. Mechanisms of VGL channels modulation are investigated extensively not only to understand the basic principles underlying the process, but also to facilitate drug development in order to overcome disease-causing dysfunction of the channels. During my research, I focused on two VGL families: voltage-gated potassium channels and cyclic nucleotide-gated (CNG) ion channels. In my first project I investigated the human voltage-gated potassium channel Kv7.2. This channel is expressed in neurons and plays an important role in regulation of neuronal excitability; activators of Kv7.2 are developed for treatment of epilepsy and pain. I modeled the transmembrane (TM) region of Kv7.2 and performed docking of a small molecule-activator named NH29 into the obtained structure. The docking model was tested experimentally, and NH29 action mechanism was proposed. In another project I studied the interaction between the human Kv7.1 channel and its regulatory subunit KCNE1. Kv7.1 is also a voltage-dependent potassium channel, and its association with KCNE1 significantly alters its functionality. I constructed a three-dimensional (3D) structure of the TM region of the complex, which agreed with previous disulfide mapping studies. The model-structure suggested molecular interpretations of electrophysiological recordings of two KCNE1 mutations designed to test the model. I also conducted elastic network analysis of Kv7.1 fluctuations in the presence and absence of KCNE1, proposing mechanistic perspectives on the known modulatory effects of KCNE1. In the last project, I modeled the 3D structure of the

human cone CNG channel; mutations in the cone channel can cause achromatopsia, characterized by color blindness, photophobia, nystagmus, and reduced visual acuity. The model-structure can facilitate studies of these disease-causing mutations, and I utilized it to provide molecular interpretation of several known mutations. In addition, I investigated the global motions of the cone CNG channel, employing elastic network models. The analysis revealed interesting insights on channels gating.

List of publications related to this thesis

1. Gofman, Y., Haliloglu, T. and Ben-Tal, N. Model-structure of the human nucleotide-gated cone channel: implications on clinical mutations and gating. (In preparation)
2. Gofman, Y., Haliloglu, T. and Ben-Tal, N. (2012) How does KCNE1 regulate the Kv7.1 potassium channel? Model-structure and dynamics of the Kv7.1-KCNE1 complex. *Structure,* **20**, 1343–1352.
3. Gofman, Y.[*], Peretz, A.[*], Pell, L.[*], Haitin, Y., Patrich, E., Ben-Tal, N. and Attali, B. (2010). Targeting the voltage sensor of Kv7.2 channels with a new gating-modifier. *Proc. Natl. Acad. Sci. USA*, **107**, 15637–15642.

[*] - equal contributors.

1. Introduction

Voltage-gated-like (VGL) ion channels are integral membrane proteins that can mediate efficient and selective passage of ions across the membrane. These channels facilitate a diverse range of physiological processes, including signal transmission in the nervous system, muscle contraction, sensory perception, hormone secretion, gene expression, cell division and more. The VGL ion channels superfamily is the third in size group of signal transduction proteins, succeeding the G protein–coupled receptors and the protein kinases in number (1). The common structural theme of the VGL channels is the four-fold symmetry organization of the pore domain (1). However, the VGL ion channels are regulated by different stimuli (that induce channels' opening or closure), including membrane voltage, extracellular or intracellular ligands, temperature, and membrane tension. Consequently, the members of the VGL superfamily differ from each other by the structural domains adapted to "sense" a particular stimulus and to mediate the corresponding gating response.

The first crystal structure revealing the architecture and organization of the pore domain was determined in 1998 by the group of Roderick MacKinnon (2). The importance of the discovery was acknowledged by awarding the 2003 Nobel Prize for Chemistry to MacKinnon (3). The bacterial potassium channel KcsA was formed by four identical subunits, each containing two TM helices, M1 and M2 (Figure 1.1A) (2). The short re-entrant loop between the two TM helices consisted of a pore helix and an evolutionarily conserved stretch of five residues TVGYG (Figure 1.1B). The conserved stretch from each subunit co-assembled the selectivity filter, with the carbonyl groups of TVGYG lining the narrowest part of the pore (2). Since then, several other bacterial ion channels were solved, expanding our understanding of ion channels (4-6). The next major breakthrough was determination of a mammalian (rat) voltage-gated

potassium channel Kv1.2 (7). However, this structure did not allow identification of all side chains, and have been recently refined (8). The next structure of the rat Kv1.2/Kv2.1 chimera channel had higher resolution, so that identification of all residues in the density map was possible (9). Both structures are composed of four monomers, each containing six TM regions, named S1 to S6 (Figure 1.1C). The first four transmembrane helices, namely S1, S2, S3, and S4, in each subunit make up a voltage-sensor domain (VSD). The last two transmembrane helices of all subunits (S5 and S6, corresponding to KcsA M1 and M2, respectively) jointly assemble the central pore domain (Figure 1.1C). S4 usually carries several evolutionarily conserved, positively charged residues, known to "sense" the membrane potential and to drive the responding conformational change (10). In the structures of both mammalian channels, these "voltage-sensing" residues are accessible to the extracellular solvent, as expected for the depolarized state of the channels (Figure 1.1C).

The largest family among the VGL superfamily is potassium voltage-gated ion channels. These channels sense changes in the voltage across the cell membrane and respond by allowing potassium ions out with high selectivity and efficiency. In excitable cells, such as neurons and muscle cells, the Kv channels allow efflux of K^+ ions across the membrane restoring the resting potential (1,11). In non-excitable cells, i.e. lymphocytes, the Kv channels are the driving force for Ca^{2+} ions entry, which is important for the regulation of various cell functions (1,11). In humans, 12 subfamilies of the potassium voltage-gated ion channels exist, named Kv1-12 (1).

The voltage-gated potassium channels are primarily regulated by the changes in the membrane potential. However, many of these principal subunits associate with auxiliary subunits that modify their electrophysiological properties (12). For instance, the members of Kv1 subfamily are modulated by the intracellular Kvβ subunits (13). Kvβ subunits have tetrameric

structure, and they interact specifically with the cytosolic domain of Kv1 channels (Figure 1.2A) (1,12). K^+ channel interacting proteins (KChIPs) represent another family of auxiliary subunits (Figure 1.2B). In contrast to the Kvβ subunits, they do not form tetramers, but interact specifically with the cytoplasmic domain of Kv4 channels as monomers (Figure 1.2B) (14). A rather distinct family of auxiliary subunits includes KCNE1 (MinK) and so-called MinK-related proteins (12). KCNEs are small proteins, generally interacting with members of the Kv7 channels. KCNEs differ from the Kvβ and KChIP subunits, as they feature one membrane-spanning segment and thus interact with the TM domain of Kv7 channels.

Many members of the VGL superfamily are voltage-gated channels, "sensing" the membrane potential with their VSDs. However, some of them are regulated, additionally or even exclusively, by other signals. The "sensing" in these cases is usually completed by a cytoplasmic regulatory domain connected to the carboxyl terminus of the S6 helix. The regulatory domains bind the regulatory molecules, e.g., ions, small molecules or even proteins, and transfer the signal to the pore domain. For instance, calcium-activated potassium channels are modulated by the concentration of Ca^{2+} in the cytosol (Figure 1.3C); inwardly rectifying potassium channels feature a cytoplasmic domain that can interact with a number of regulatory molecules, such as G-proteins, ATP, PIP_2 and Na^+ (Figure 1.3A); cyclic nucleotide–gated (CNG) and hyperpolarization-activated cyclic nucleotide–gated channels are regulated by cyclic nucleotides binding to their cytoplasmic domains (Figure 1.3B) (1).

Undoubtedly, the crystal structures allowed the structure-function studies and the atomic level understanding of the VGL ion channels. However, in order to manage dysfunctions of ion channels in humans and to facilitate drugs development, high-resolution structures of the human ion channels are required. These tasks are still challenging, since human TM proteins are

particularly complex targets for structure determination. Therefore, homology (comparative) modeling techniques are often employed to produce model-structures of the human ion channels (or other TM proteins). This currently leading computational approach for generating model-structures utilizes structures of proteins, homologous to human, determined experimentally at high-resolution (15). Recent studies showed that comparative modeling is an efficient methodology that can be successfully applied even when the sequence identity between the query protein and the high-resolution template is extremely low (15).

The key to an accurate homology model is the alignment of sequences of the query (target protein) and the template (crystal structure). This is especially challenging when the sequence identity between the two is low, as in most cases of modeling of a protein from mammalian origin using a crystal structure of a prokaryotic homolog. However, given a correct alignment, the predicted backbone of the protein's core, i.e., the backbone of the TM segments, is presumably accurate (15). The loop regions are usually more flexible in structure and more variable in sequence, and their modeling may not be based on the existing structural template. Consequently, the predicted loops conformations are imprecise, both in terms of the backbone and the side chains (15,16). In contrast, the side chains conformations in the protein core can be reliable, if they are conserved between the query and the template. As functionally important sites are often highly conserved among homologous proteins, their 3D structure in the model can be accurate. Interestingly, a recent study showed that homology model-structures of G protein-coupled receptors are suffice for computational virtual screening of possible ligands, a procedure that normally requires accurate, high-resolution structures (17). Additional pitfall of comparative modeling is possible structural changes between the query and the template, which could be expressed even in different number of TM segments (18). However, the fold of the voltage-gated-

like channels, the focus of the current thesis, is essentially preserved among the whole superfamily (1).

The evaluation of the model-structures is an important step in modeling. Although a number of computational methodologies have been developed for model-structures of soluble proteins, their performance on model-structures of TM proteins was not established (15). In the absence of such methodologies, model-structures of TM proteins can be validated by inspecting their general characteristics. The first general characteristic is the hydrophobicity profile of the model-structures of TM proteins (Figure 1.4A). The expectation is that hydrophobic residues would be exposed to the lipid, while charged and polar amino acids would be buried in the protein core or located in the loop regions. An additional general feature of proteins structure is the evolutionary conservation profile. It is anticipated that evolutionarily conserved amino acids would be buried in the protein core and that variable residues would be exposed to the lipid or located in the loop regions (Figure 1.4B). The validity of the evolutionary conservation pattern have been recently verified on a large dataset of experimentally determined high-resolution structures (19).

During my PhD studies, I focused on human ion channels and modeled 3D structures of selected human VGL channels. First, I modeled the voltage-gated potassium channel Kv7.2 and investigated its modulation by a small molecule. Next, I modeled a 3D structure of the Kv7.1-KCNE1 complex, where the former is a voltage-gated potassium channel, and the latter is its auxiliary protein. I inspected the effects of KCNE1 on the functionalities of Kv7.1. Both projects were complemented by experimental studies performed by the lab of Prof. Bernard Attali (Tel-Aviv University). Finally, I focused on the human cone cyclic nucleotide-gated ion channel. I further utilized the resultant model-structure to elaborate on the gating of the channel.

1.1 Pharmacological studies of the Kv7.2 channel

Voltage-gated cation channels play crucial roles in brain and cardiac excitability. Mutations of ion channel genes in humans lead to severe inherited neurological, cardiovascular or metabolic disorders, called 'channelopathies' (20). So far, the medicinal toolbox has focused on the pore domain and its gate, in an attempt to cure ion channel-related dysfunctions by channel blockers or openers (21). In contrast, the VSD of voltage-gated cation channels was virtually not exploited for therapeutic purposes. VSDs are found in voltage-dependent cation channels and other voltage-regulated proteins (10). In addition, VSDs have been recently characterized in voltage-regulated proteins that lack associated ion channel pores (22-24). A voltage-sensitive phosphatase, Ci-VSP, has a VSD that is coupled to a phosphatase domain (22). In the human voltage-activated proton channel (Hv1), the VSD itself functions as a proton channel (23-25).

The charge-bearing S4 helix together with the C-terminal part of the S3 helix, also called S3b, form a helix–turn–helix structure, often termed the paddle motif (Figure 1.1C) (7,26). Recent data indicate that the VSD paddle motif can drive channel opening when transplanted from the archaebacterial Kv channel (KvAP) or voltage-sensing domain proteins (Hv1 and Ci-VSP) into eukaryotic voltage-gated K^+ channels (10,27). Thus, VSD paddle motifs are modular and transferable structures, whose functions are conserved in voltage sensing proteins (10).

The Kv7 potassium channel family, encoded by the *KCNQ* genes, comprises five members in humans, Kv7.1–Kv7.5, four of which (Kv7.2–Kv7.5) are expressed in the nervous system (28). In quest to target neuronal M-type K^+ channels, encoded by Kv7.2 and Kv7.3 subunits assembly, novel diphenylamine carboxylates were recently designed as powerful openers or blockers of the Kv7.2 channel (29). M-channels generate subthreshold, non-

inactivating voltage-gated K^+ currents that play an important role in controlling neuronal excitability (30,31). In collaboration with the lab of Prof. Attali (Tel-Aviv University), we showed that the novel opener compound, NH29, acts as a non-toxin gating modifier, which robustly increases Kv7.2 K^+ currents. Experimental and modeling data suggest that in the Kv7.2 channel open state, NH29 docks to the external surface of the VSD at the interface of helices S1, S2 and S4. NH29 stabilizes the interaction between two conserved residues in S2 and S4, known to interact electrostatically in voltage-gated K^+ channels. Intriguingly, NH29 is also a potent blocker of TRPV1 channels, a feature similar to that described for tarantula toxins (32,33). The results indicate that NH29 may operate via a voltage-sensor trapping mechanism similar to that depicted for various gating-modifier toxins (34). Thus, the VSD represents a novel and important pharmacological target for the treatment of major hyperexcitability disorders like epilepsy, migraine or neuropathic pain.

1.2 Regulation of the Kv7.1 channel

As mentioned above, Kv7.1 is the only member of the Kv7 channels that is expressed mostly in heart tissues (28). The main function of Kv7.1 is repolarization of the cardiac cells following action potential. This function is accomplished by assembly with KCNE1. In comparison to the kinetics of the isolated Kv7.1 channel, the KCNE1-Kv7.1 complex manifests slower activation and deactivation of voltage-gated currents (called I_{Ks}) (35,36). Mutations in both proteins can lead to cardiac long QT syndrome LQTS, which in turn can cause arrhythmias, ventricular fibrillation and cardiac arrest (31,35,36).

Despite the biological significance of the Kv7.1-KCNE1 interaction, its exact nature has yet to be elucidated. In fact, even the stoichiometry of the complex remains a subject of debate. Some experiments have shown that two KCNE1 molecules associate with each Kv7.1 tetramer

(37,38), while others point to multiple stoichiometries (39,40). Kang and co-authors (41) used a homology model of Kv7.1 (42) and the nuclear magnetic resonance (NMR) structure of KCNE1 to predict the structure of the complex. However, the preliminary analysis has shown that this model-structure is incompatible with evolutionary data in that the most conserved amino acids of KCNE1 are exposed to the lipid, and the variable residues are buried at the interface with Kv7.1, in contrast to the typical conservation pattern (Figure 1.5). Therefore, I attempted to provide further insight into the Kv7.1-KCNE1 interaction, using the available model-structure of Kv7.1 (42) and various computational protein-protein docking techniques in combination with conservation data. To test the structural model, the electrophysiological properties of Kv7.1 co-expressed with two KCNE1 mutants were examined in the lab of Prof. Attali (Tel-Aviv University). Overall, the experimental findings are consistent with my model-structure of the complex.

Analysis, using elastic network models, suggested a molecular basis for alterations observed in the dynamics of the Kv7.1-KCNE1 complex in comparison to the isolated Kv7.1 channel. KCNE1-induced slow deactivation is attributed to the lower mobility of the voltage sensor domains of the channel upon KCNE1 association. Abolishment of voltage-dependent inactivation could result from the decreased fluctuations in the external vestibule of the channel upon interaction with KCNE1; Kv7.1 residues D317 and E295 could play a role in the regulation of voltage-dependent inactivation of the channel. KCNE1 association induces changes in the motion of residues G272, V310 and T311 of Kv7.1, changes that could be associated with the channel's enhanced conductivity upon complex formation.

1.3 Cyclic nucleotide-gated (CNG) ion channels

CNG ion channels are nonselective cation channels, crucial for visual and olfactory sensory transduction in vertebrates (1,43-46). Like other members of the voltage-gated-like ion channel superfamily (1), the CNG channels are composed of four (identical or homologous) monomers, each containing the TM helices S1–S6 (43,44). In spite of the presence of the VSD, CNGs display very little voltage-dependent activity (1,43-45). Rather, each monomer in the CNG channel contains a cytosolic cyclic nucleotide–binding domain (CNBD), connected by a so-called C-linker to the C-terminus of the S6 helix, and the channel is gated by cyclic nucleotide binding to the CNBDs (1,43-45).

Structural studies of the bacterial homolog MlotiK1 from *Mesorhizobium loti* have revealed the 3D structures of the CNBD (47-50) and of the TM domain (51). In mammals, structures of CNBDs have been determined in hyperpolarization-activated cyclic nucleotide-gated (HCN) channels (46,52-56), which are closely related to CNGs and share a similar fold (44,57). However, despite extensive structural studies, the gating process in CNG (and in HCN) channels is not fully understood (45,58-60).

Over time, several different models describing the gating process of CNGs have been proposed (reviewed in (57-59,61)). The models differ from each other in the minimum number of bound nucleotides required for activation and in the cooperativity between the binding sites. The number of open and closed states of CNG channels is yet another discriminating parameter between various gating schemes. The simplest model, known as the “sequential” model, suggests that three ligand molecules bind to the closed channel, and binding of a fourth ligand causes the allosteric conformational change to the open state (62). The sequential model was found insufficient, since it does not account for the experimentally confirmed opening of unliganded or partially liganded CNG channels (63). The Monod, Wyman, and Changeux (MWC) model (64)

postulates that the channel can open with any number of bound ligands, i.e., 0 to 4; the higher the number of bound ligands, the more favorable the transition from the closed to the open state. This model is limited by the notion that all four binding sites are identical. Moreover, it does not account for the existence of sub-conductance states, allowing only one open state (61). A third model, the "dimer-of-dimers" model, describes the tetramer as a dimer of dimers, in which each dimer acts as an MWC unit, meaning that there is cooperativity between the monomers within the dimers (65). For the channel to open, both dimers must be activated independently, meaning there is no cooperativity between the dimers. Lastly, the modular gating model defines the following modules within the channel: the VSD, the pore, the C-linker and the CNBD (66). Each module is in equilibrium between two possible conformations: the VSD and the C-linker can either be resting or activated, the pore can be closed or open, and the CNBD can be ligand-free or -bound. The modules are coupled to each other, so that the state of each module affects the states of other modules.

In vertebrates, each of the six known members of the CNG family is classified into A and B subunits, which can coassemble in several combinations to produce functional heterotetrameric channels (1,43-45,57,67). In cone photoreceptors, for example, functional CNG channels are composed of two CNGA3 subunits and two CNGB3 subunits, with like subunits positioned next to each other (68). The activity of the cone CNG channels is controlled by cyclic guanosine monophosphate (cGMP) binding to CNBD. In the dark, the concentration of cGMP is high, and the cone CNG channel is maintained in its open state, allowing influx of Na^+ and Ca^{2+} ions. Light absorption by visual pigments leads to hydrolysis of cGMP and closure of the cone CNG channel (43,44,67). The cone system confers color vision; mutations in CNGA3 and CNGB3 subunits cause achromatopsia, characterized by color blindness, photophobia, nystagmus and reduced visual acuity (43). Tens of disease-causing mutations have been identified so far in the

genes encoding for CNGA3 and CNGB3 (Tables 1.1 and 1.2)(43), although most of them have not been analyzed functionally (69).

Here I employed comparative (homology) modeling techniques to produce an approximate full-length 3D model-structure of the human cone channel in its resting state, with the CNBDs in ligand-free (apo) or ligand-bound (holo) conformation. The modeling was challenging because the structure was derived from two templates: a template for the TM domain and a template for the cytosolic domain (including the CNBD). Moreover, the sequence identity between the template and the query in the TM region was approximately 10%, which is rather low. Still, the resultant model-structure was compatible with the typical evolutionary conservation pattern and the available experimental data. In addition, I utilized the model-structure to propose molecular interpretations for several disease-causing mutations. To elucidate the mechanism of the allosteric signal transduction through the CNG channels, I analyzed the dynamics of the apo- and holo-states of the homotetrameric CNGA3 channel using coarse-grained elastic network models. I suggest that the slowest mode of motion of the CNG channel is related to gating. In this motion type, the TM and cytosolic domains rotate around the membrane normal in opposite directions. This deduction is supported by existing experimental evidence. I carried out a similar analysis of the modes of motion of the prokaryotic KirBac3.1 channel, which has a known gating mechanism and resembles the CNG channel in terms of the architecture of the pore domain as well as the function of the cytoplasmic domain, and obtained further support for this proposition. Investigation of the next-slowest modes of motion of the CNG channel revealed that either the TM domain or the CNBDs of the CNG (but not both domains together) fluctuate in each mode, with inter-domain cooperativity between the mobile and immobile domains. This observation corroborates the modular gating model of the CNG

channels (66). Lastly, the dynamics of the channel in the apo- and holo-states were, essentially, indistinguishable, in agreement with the demonstrated opening of unliganded channels (63,70).

2. Research aims

My main research goal is to suggest insight into the structure-function relationship of selected human voltage-gated-like ion channels by means of various computational methodologies. Using structural modeling, both comparative and *ab initio*, I investigated the transport mechanism of the chosen human ion channels. I also explored the modulation mechanisms of the channels by small molecules, regulatory proteins and regulatory domains.

The specific goals of my research were as follows:

1. To model the 3D structure of the transmembrane domain of the human Kv7.2 channel and suggest the binding mode of a small molecule known to lock the channel in its open state.
2. To model the 3D structure of the human Kv7.1-KCNE1 complex and to reveal the mechanism(s) by which KCNE1 modulates Kv7.1 activity.
3. To model the 3D structure of the human cone CNG channel and to investigate the signal transduction mechanism from its CNBD to the pore domain.

3. Methods and materials

Structural modeling and docking of Kv7.2

I employed comparative (homology) modeling techniques to produce an approximate 3D model-structure of the human Kv7.2 transmembrane domain (residues 92-323). The possible templates were the X-ray structure of the rat Kv1.2 channel (Protein Data Bank (PDB) entry 2A79) (7) and its modified chimeric version containing the rat Kv2.1 paddle (PDB entry 2R9R) (9). The query human Kv7.2 channel, however, shares a very low sequence identity of about 22% with these structures, which complicates the modeling. Instead, as a template, I chose a model-structure of the human Kv7.1 channel, which was derived by homology from the X-ray structure of the rat Kv1.2 channel (7), and, therefore, essentially identical in the TM region to the latter (42). The chosen template shares about 60% sequence identity with the query, thus simplifying the modeling process. To increase the accuracy (15), the pairwise alignment between the sequences of the query and target (SwissProt entries KCNQ2_HUMAN and KCNQ1_HUMAN, respectively) was derived from a multiple alignment of 128 sequences. These were collected as KCNQ2_HUMAN homologs from the CleanUniProt database (71). Redundant (>99% sequence identity), and fragmented sequences were discarded. The full-length sequences of these proteins were then aligned using the MAFFT program (72). Next, I constructed a 3D model-structure of the human Kv7.2 channel based on the obtained pairwise alignment using NEST (73), with default parameters. I used the Plop program (74) to further optimize the model-structure, i.e., to eliminate steric clashes and improve side-chains packing in the protein core.

The refined model-structure was used for substrate docking, using the LigandFit tool (75) from the DiscoveryStudio 2.0 software (Accelrys, San Diego, CA). 41 docking cavities were

detected using the LigandFit site search utility. Of these, only one was in line with the mutagenesis data, and was selected as the seed binding site. The cavity was then expanded with the Discovery Studio site editing tool to a distance of 1.5Å in all directions and edited manually to remove points protruding far outside the main cavity. To improve the search in conformational space the binding pocket was partitioned into 3 regions. The docking of the NH29 ligand into each of the three regions was conducted using the Dreiding force field (76) and putative NH29/channel complexes were selected. These complexes were minimized using the Smart Minimizer algorithm and evaluated with the DockScore (75), LigScore (77) and PMF04 (78) modules of the Discovery Studio software.

Modeling of the Kv7.1 - KCNE1 complex

KCNE1 has an extracellular N-terminus, a single TM segment between residues 44-66, and a cytoplasmic C-terminus (35,36). The available 3D structure of human KCNE1 (PDB entry 2K21) has a major curve in the TM segment consistent with the radius of the lipid micelles used to determine the structure (41). Since the TM conformation may differ significantly from the one observed in micelles (79,80), I modeled the 3D structure of residues 36–75 using the Rosetta Membrane *ab-initio* protocol (81). I obtained 10,000 decoys and clustered them, with a root mean square deviation cutoff of 2Å. The ten lowest-energy candidates in the largest cluster were selected for further analysis. The decoys, all α-helical with a slight kink around residues 56–58, differed from each other in the extent of curvature. I docked these decoys into the symmetric model-structure of the human Kv7.1 (42), using PatchDock (82), and collected the 20 highest-scoring complexes for each candidate. The resulting 200 complexes were filtered manually based on the membrane topology of KCNE1 (35), and 27 remained. These were evaluated according to their hydrophobicity profiles. The expectation was that hydrophobic residues would be exposed

to the lipid, while charged and polar amino acids would be buried in the protein core and/or protein-protein interface. I examined each model-structure visually to verify this.

I also evaluated the complexes' evolutionary conservation profiles. It was anticipated that evolutionarily conserved amino acids would be buried in the protein core or protein-protein interface, and that variable residues would be exposed to the lipid. I used ConQuass, which assigns scores to model-structures based on the degree to which they adhere to this pattern (19). The conservation profile was constructed using the ConSurf server (83). The homologs were collected from the non-redundant (NR) database (84) using PSI-BLAST (85). Redundant sequences (>99% sequence identity) were discarded, and the resultant 76 sequences were aligned using MUSCLE (86) (Figure 3.1). The complex with the highest ConQuass score was chosen for further docking with the Rosetta docking protocol in high-resolution mode (87). The 1,000 complexes obtained through this procedure were clustered using a root mean square deviation cutoff of 3Å and assessed with ConQuass again. The model with the highest ConQuass score from the largest cluster was chosen.

I also performed independent Kv7.1-KCNE1 docking using the GRAMMX software (88), and the best model-structure of the complex was essentially the same (data not shown).

The final model-structure of the complex was evaluated against the available data from disulfide mapping studies (89-91). In principle, for a disulfide bond to form between a pair of residues, the two residues must be very close to each other, with Cβ-Cβ distance of approximately 4.6Å (92,93). However, when the residues are in mobile regions, e.g. loops or helix termini, a bond may form even if the residues are up to 15Å apart (92). The pairs taken into account were G40/T144, G40/I145, G40/Q147, K41/T144, K41/I145, K41/Q147, L42/V324, E43/W323 and A44/V141, where in each pair the first amino acid is from KCNE1 and the second

from Kv7.1 (89-91). The distances between the residues in each pair in the final model are listed in Table 3.1. I also determined the distances separating the pairs verified as not interacting by the disulfide mapping studies (Table 3.3). In most cases the residues in each pair were separated by a distance of more than 15Å in the final model. Still, some pairs are separated by a distances of less than 15 Å; an inspection of the model-structure of the complex revealed that only three pairs, namely L45/L142, D39/I145, A44/I145, can be in physical contact to create an disulfide bond.

Modeling of CNGA3 and CNGB3 subunits

Each subunit of any CNG channel contains two domains: the TM domain and the cytosolic CNBD (which also contains the C-linker). In the absence of a high-resolution structure comprising both domains, I focused on the existing structures of the individual domains. A variety of high-resolution structures of mammalian CNBDs from HCN channels is available (46,52-56). CNGs and HCN channels are closely related in structure (57); thus, HCN CNBDs can serve as templates for modeling the CNBDs of CNGs. For the apo-state template, the only available structure of a ligand-free CNBD was from the mouse HCN2 (mHCN2) channel (PDB entry 3FFQ (54)). In order to model the ligand-bound state of the cone CNG channel, I used as a template the only available holo-state structure of mHCN2 in complex with cGMP (PDB entry 1Q3E (46)). To derive the structures of the CNGA3 and CNGB3 CNBDs from the selected templates by homology, pairwise alignment between the queries and the templates was required. The CNBD of the mHCN2 channel shared sequence identity of 33% and 29% with the CNBDs of CNGA3 and of CNGB3, respectively. When a query and a template display sequence identity of 30% or more, a simple pairwise alignment is sufficient to produce a reliable model-structure (15). However, extraction of the pairwise alignment from a multiple sequence alignment improves the accuracy (15). Therefore, I searched for mHCN2 homologs in the CleanUniProt database (71)

and aligned their sequences using the MUSCLE program (86). Both subunits, CNGA3 and CNGB3, were detected as homologs, and their alignment with mHCN2 was extracted from the multiple sequence alignment (Figure 3.2).

The crystal structure of the bacterial MlotiK1 channel in its closed state (51) (PDB entry 3BEH) served as the template for modeling the TM domains of CNGA3 and CNGB3. The sequence identity between the TM domain of MlotK1 and those of CNGA3 and of CNGB3 was 10% and 12.5%, respectively. Consequently, the sequence alignment between the queries and the template was quite challenging. In cases of such low identity between a query and a template, it is recommended to use a variety of tools in order to produce a reliable pairwise alignment (15). I exploited the secondary structure prediction algorithm PsiPred (94), several methods for the identification of TM segments (namely MEMSAT(95) and HMMTOP (96)), the FFAS03 server for fold-recognition (97), and a methodology for profile-to-profile alignment HHpred (98) (Figure 3.3). All tools traced the TM segments in similar locations within the sequences, with some deviations (Figure 3.3). Additionally, I created a multiple sequence alignment that included the sequences of the queries and the template. To this end, I searched for MlotK1 homologs in the SwissProt database (99) using CS-BLAST (100); 3 iterations were performed with maximal e-value of 0.00001. The collected homologs were aligned using the MUSCLE program (86). The final alignment between the queries and the template took into account the outputs of all methodologies used (Figure 3.3).

The initial 3D models of the CNGA3 and CNGB3 subunits were constructed using the Modeller software, version v9.10 (101). The loops were refined with the Rosetta loop modeling application (87,102).

The conservation profile was calculated using the ConSurf server (83). I used CS-BLAST (100) to collect homologous sequences of CNGA3 and of CNGB3 from the CleanUniProt database (71). Redundant (>99% sequence identity) and fragmented sequences were discarded. The sequences were aligned using the MUSCLE program (86).

Elastic network models

I analyzed the Kv7.1-KCNE1 model-structure and the model-structure of homotetrameric CNGA3 channel using elastic network models. These models have provided insights on the dynamics and function of potassium channels (103-106). A detailed description of the GNM is available in (107,108) and of ANM in (109,110). Here I provide a short summary.

In the GNM calculations the protein structure was simplified into α-carbon atoms and treated as an elastic network of nodes connected by hookean springs of uniform force constant γ. Two nodes i and j were assumed to display Gaussian fluctuations around their equilibrium position if the distance between them was below the (commonly used) cutoff of 10 Å. The inter-node contacts were then defined by an $N \times N$ Kirchhoff matrix $\boldsymbol{\Gamma}$, where N is the number of amino acids in the protein. The correlation between the fluctuations of two nodes i and j, $\Delta\mathbf{R}_i$ and $\Delta\mathbf{R}_j$, respectively, was calculated as follows:

$$<\Delta\mathbf{R}_i\Delta\mathbf{R}_j> = (3k_BT/\gamma)[\boldsymbol{\Gamma}^{-1}]_{ij} = (3k_BT/\gamma)\sum_k[\lambda_k^{-1}\mathbf{u}_k\mathbf{u}_k^T]_{ij} \quad (1)$$

where $\mathbf{u}_k$ and λ_k are, respectively, the k-th eigenvector and k-th eigenvalue of $\boldsymbol{\Gamma}$, k_B is the Boltzmann constant, and T is the absolute temperature; k_BT/γ was taken as 1 Å^2. Overall, Eq. 1

predicts the mean-square displacement of each residue (node) when $i = j$, and when $i \neq j$ it predicts the correlations between the fluctuations of residues i and j as a superimposition of N-1 eigenmodes.. λ_k is proportional to the k-th mode frequency, the inverse of which gives the relative contribution of this mode to the protein's overall structural motion. The minima in the obtained fluctuation profile for a given mode suggest possible hinge points that coordinate the cooperative motions between structural elements in this mode.

In contrast to isotropic GNM, ANM determines the direction of fluctuations. Here $\boldsymbol{\Gamma}$ is replaced by the $3N \times 3N$ Hessian matrix $\boldsymbol{H}$, the elements of which are the second derivatives of the inter-node potential described by Eq. 1, with a cutoff of 15 Å. The correlation between $\Delta\mathbf{R}_i$ and $\Delta\mathbf{R}_j$ was decomposed into 3N-6 modes and calculated as follows:

$$<\Delta\mathbf{R}_i\Delta\mathbf{R}_j> = (3k_BT/\gamma)\mathrm{tr}[\boldsymbol{H}^{-1}]_{ij} = (3k_BT/\gamma)\sum_k \mathrm{tr}[\lambda_k^{-1}\mathbf{u}_k\mathbf{u}_k^T]_{ij} \quad (2)$$

where $\mathrm{tr}[\mathrm{H}^{-1}]_{ij}$ is the trace of the ij-th submatrix $[\mathbf{H}^{-1}]_{ij}$ of $\mathbf{H}^{-1}$. The eigenvectors allowed me to identify alternative conformations sampled by the individual modes, simply by adding/subtracting the eigenvectors to/from the equilibrium position in the respective modes. Thus, being an anisotropic model, ANM provides information on the directions of the motions in 3D, while GNM is more realistic with respect to the mean-square fluctuations and the correlation between fluctuations (106).

Several studies have demonstrated that the first few slowest GNM modes, assigned the lowest frequencies, are implicated in protein function (106,111). The least mobile residues suggested by these modes play key mechanical roles, such as being hinge centers or controlling the cooperative movements of domains. Therefore, while investigated the dynamics of Kv7.1

channel in the presence and absence of KCNE1, I focused on the eight GNM modes identified as slowest on the basis of the distribution of eigenvalues; these modes were responsible for approximately 22% of the overall motion (Figure 3.4). Investigating the CNG channel, for simplicity and to facilitate more convenient representation of the data, I studied a symmetric tetrameric channel composed of four identical CNGA3 subunits. I focused on the six GNM modes identified as slowest on the basis of the distribution of the eigenvalues (Figure 3.5); these modes were responsible for approximately 40% of the overall motion of the channel (Figure 3.5). The superimposition of the residues' mean square displacement predicted by GNM and ANM revealed the correspondence between the two elastic network models. Thus, using ANM, I was able to determine the direction of fluctuations characterized by GNM.

Cell cultures and electrophysiology experiments on the Kv7.2 channel (performed by the lab of Prof. Attali, Tel-Aviv University)

Chinese hamster ovary and primary hippocampal and dorsal root ganglion neuronal cultures were performed as described (112).Whole-cell patch-clamp recordings in Chinese hamster ovary cells, in dorsal root ganglion neurons and in hippocampal neurons were carried out as before (112). All data were expressed as mean ± SEM. Statistically significant differences were assessed by unpaired t-test (two-tail) assuming equal variances for comparing parameters of wild-type (*wt*) Kv7.2 with those of Kv7.2 mutants and by paired *t-test* (two-tail) for comparing parameters in the same cell without and with the opener.

Details concerning the synthesis of NH29 have been previously described as compound 6 in Peretz et al., 2007 (29).

Experimental procedures on the Kv7.1 channel (performed by the lab of Prof. Attali, Tel-Aviv University)

The mutations of human KCNE1 were constructed using standard PCR techniques, using the Pfu DNA polymerase (Promega). The mutants were entirely sequenced using a DNA automatic sequencer. Human KCNE1 DNA (*wt* and mutants) were linearized by BamH1 enzyme (Promega); human KCNQ1 DNA (*wt*) were linearized by Not1 enzyme (Promega). Capped complementary RNAs (cRNAs) were transcribed from linearized human KCNE1 by T3 RNA polymerases and from linearized human KCNQ1 with T7 RNA polymerases (mMessage mMachine, Ambion). The cRNAs were quantified by UV spectroscopy (Nanodrop), and its integrity and concentration were verified by running an aliquot on a formaldehyde agarose gel.

Channel expression into Xenopus oocytes and electrophysiology were performed as previously described (113). Current signals were filtered at 0.2 kHz and digitized at 1 kHz. The holding potential was - 80mV. The reversal potential of the membrane, according to the Nernst-equation, was calculated to be V_{rev} = -81.4mV.

$$E_{K^+} = \frac{RT}{ZF} \times ln \frac{[K^+]_o}{[K^+]_i} \qquad (3)$$

Where R = gas constant, T = temperature, Z = valence, F = Faraday's constant and $[K^+]_o$ = 4mM, $[K^+]_i$ = 100mM. In order to subtract the leak off line from the currents obtained in the *I-V* protocol, the resistance was changed at the - 80mV step pulse of the trace obtained (which is about the E_{rev}) in order to zero the current. Then, the other voltage-step currents were leak-subtracted accordingly, using the Ohm's law. Data analysis was performed using the Clampfit program (pCLAMP 10.2, Molecular Devices), Microsoft Excel (Microsoft), Prism (Graphpad).

For a measure of deactivation kinetics, a single exponential fit was applied to the tail currents and measured from + 40mV prepulse at -60 mV tail potential according to:

$$f(t) = \sum_{i=1}^{n} A_i e^{-t/\tau_i} + C \quad (4)$$

Because of the complex activation kinetics of the currents, including a sigmoidal delay, a rough estimate of the activation kinetics, $T_{1/2}$ act was calculated from the macroscopic current and measured at + 40mV. $T_{1/2}$ act is the time at which the current amplitude is half-activated. To analyze the voltage dependence of I_{KS} channel activation, a single exponential fit was applied to the tail currents (-60 mV tail potential) and extrapolated to the beginning of the repolarizing step. Chord conductance (G) was calculated by using the following equation:

$$G = I/(V - V_{rev}) \quad (5)$$

Where I corresponds to the current, and V_{rev} corresponds to the calculated reversal potential. G was estimated at various test voltages V and, then, normalized to a maximal conductance value, G_{max}, calculated at + 40 mV.

Voltage-dependent activation curves were fitted by the Boltzmann equation:

$$G/G_{max} = 1/\left(1 + exp^{(V_{50}-V)/s}\right) \quad (6)$$

Where V_{50} is the voltage at which the current is half-activated, and s is the slope factor. To analyze the voltage dependence of I_{KS} channel activation, G was deduced from tail currents as

above. All data were expressed as mean ± SEM. Statistically significant differences between the *wt* and the mutants were assessed by Student's t-test.

4. Results

4.1 Targeting the voltage sensor of Kv7.2 channel with a new gating-modifier (in collaboration with the lab of Prof. Attali; the experiments were performed by the lab of Prof. Attali)

Modeling of the TM region of Kv7.2

I generated a 3D model-structure of the TM domain of the human Kv7.2 channel, and examined its validity using different approaches. First, the evolutionary conservation profile of the model was calculated using ConSurf (83). As anticipated, the conserved residues were found at the inter-helical interfaces within the TM region (Figure 4.1A). In contrast, variable residues were positioned in the periphery, either in the loops or facing the lipid membrane. Next, I examined the location of titratable residues in the TM region. As expected (114), they were mostly buried in the protein core, while hydrophobic amino acids faced the membrane (Figure 4.1B). Interestingly, R198 and R201, which are part of the voltage sensor helix S4, were exposed to the lipid. This is in keeping with the suggestion that they interact with the lipids polar heads (10). In addition, I inspected the Lys and Arg content in the extra-membrane regions. It was previously shown that the intracellular side is enriched with the positively charged residues in the vast majority of TM proteins (115). This observation, termed the 'positive-inside' rule, can be used to predict and evaluate the topology of membrane proteins (15). Indeed, the analysis of the Kv7.2 3D model revealed 9 Lys/Arg residues in the cytoplasmatic side vs. only 3 lysine residues in the extracellular side of each monomer (Figure 4.1B).

I analyzed known disease-linked residues in light of the model-structure of Kv7.2's transmembrane region (Fig. 3). All the mutations occurred in evolutionarily conserved residues located in the key structural elements. Specifically, R207W(116)/Q(117) and R214W (118) are positioned in the voltage-sensing helix S4. These positively charged residues are involved in the transduction of changes in the membrane potential to conformational changes in the channel (10),

which would explain why their substitution with electrostatically-neutral amino acids is harmful. A306T (119) lines the ions funnel from the intracellular side (Figure 4.2). This is one of the most highly conserved residues, and I suggest that the substitution of Ala with the much larger and polar Thr residue could affect ion conductance. L243F (120), S247W (121) and G271V (120) are positioned in the tight interface between S5 and the pore helix (Figure 4.2). TM α-helices interactions often involve packing motifs, such as GxxxG and GxxxG-like, where small residues, such as Ala and Ser, appear in the Gly positions (122). I propose that G271 is the ultimate residue of an AxxxG motif (A267, L268, W269, W270 and G271). A267 and G271 of the pore helix face L243 and S247 of helix S5. This interface appears to be stabilized by Cα-H··O bonds between the backbone and tightened by the presence of the sterically-confined residues, L268 and L243 (Figure 4.2) (123).

Compound NH29 increases Kv7.2 currents and inhibits neuronal spike discharge and neurotransmitter release

The Attali lab have recently designed new derivatives of diphenylamine carboxylate, which act as potent M-channel openers or blockers (29). Along this series, the pharmacological properties and the target site of the Kv7.2 channel opener NH29 were characterized. The carboxylate group of the diphenylamine diclofenac was derivatized to an amide functionality with ethanolamine and the aromatic rings were substituted with nitro groups, yielding compound NH29 (Figure 4.3A). NH29 was initially examined on *wt* Kv7.2 homomeric channels expressed in Chinese hamster ovary cells. External application of NH29 rapidly increased Kv7.2 K^+ currents at threshold potentials. At -40 mV, NH29 (25 μM) enhanced by 3.5 ± 0.3 fold Kv7.2 current amplitude (n = 15, $p < 0.01$; Figure 4.3, C and E). However, at positive potentials, the effects of NH29 became much weaker (Figure 4.3B) and little change in maximal conductance (G_{max}) was observed. The

overall increase in *wt* Kv7.2 current amplitude mainly arose from a hyperpolarizing shift of the activation curve. At 25 μM, NH29 caused a left-shift of -15.5 mV from V_{50} = -25.4 ± 0.5 mV to V_{50} = -40.9 ± 0.6 mV (n = 15, $p < 0.01$; Figure 4.3D), while at 100 μM the shift was -31 mV. In addition, NH29 slowed down the kinetics of Kv7.2 activation and more noticeably those of deactivation (Figure 4.3F). The NH29-induced slowing of deactivation (4-fold) could be accounted for by only 33% the negative shift in the voltage dependence of activation (1.3-fold slowing for a 15 mV shift), suggesting that NH29 affects Kv7.2 gating by multiple mechanisms.

Next, the Attali lab examined the selectivity of NH29 on other Kv7 channels. NH29 increased the current amplitude of heteromeric Kv7.2/Kv7.3 channels with a similar potency compared to homomeric Kv7.2 channels with an EC_{50} = 14 ± 2 μM (n = 5). In contrast, NH29 was virtually ineffective on homomeric Kv7.3 channels. NH29 weakly increased homomeric Kv7.4 currents (1.3-fold at -40 mV) and did not affect homomeric Kv7.1 and heteromeric Kv7.1/KCNE1 channels. NH29 appeared to act on Kv7.2 both in the closed and open states. Indeed, when NH29 was first applied for 4 min at -90 mV, a potential where Kv7.2 channels were in the closed state, the opener increased by more than 3.5 -fold the currents at the first step depolarization to -40 mV, indicating a closed state interaction. In addition, when Kv7.2 channels were first opened by depolarization, subsequent application of NH29 significantly increased the currents, suggesting an open state interaction.

The Attali lab further characterized the properties of NH29 on central and peripheral neurons. NH29 (25 μM) hyperpolarized the resting membrane potential (from -56.0 ± 2.0 mV to -65.0 ± 2.2 mV, n = 9; $p < 0.01$) and reversibly reduced the number of evoked spikes of dorsal root ganglion neurons (from 9.0 ± 0.8 to 0.9 ± 0.1, n = 12; $p < 0.001$; Figure 4.3G). NH29 powerfully depressed synaptic transmission (Figure 4.3, H-K). It inhibited glutamate and GABA

release as shown from the depression of network-driven excitatory and inhibitory post-synaptic currents (EPSCs and IPSCs), which were recorded from primary cultures of hippocampal neurons (112). This inhibition was reflected by the reduced charged transfer and frequency of post-synaptic currents (Figure 4.3, H-K).

NH29 does not act at the target site of retigabine

We searched for the Kv7.2 residues involved in NH29 interaction. It has been previously shown that a parent template of NH29, meclofenamate, exhibits an additive effect with the M-channel opener retigabine, suggesting that the two drugs act via different mechanisms (124). Thus, the Attali lab checked whether NH29 interacted with the target site of retigabine, which involves a crucial tryptophan residue in S5 (125-127). The Kv7.2 W236L mutant led to currents insensitive to retigabine (126,127). While retigabine (5 μM) increased by 5.5-fold the current of *wt* Kv7.2 (at -40 mV), it did not affect that of the Kv7.2 W236L mutant (Figure 4.4, A-C). Interestingly, NH29 (25 μM) markedly enhanced the current amplitude of this retigabine-insensitive mutant W236L (by 3.6-fold at -40 mV; Figure 4.4, B and C) mainly by causing a left-shift of the activation curve from V_{50} = -26.6 ± 1.7 mV to V_{50} = -38.9 ± 1.6 mV (n = 4, $p < 0.01$). These data suggest that NH29 does not act at the target site of retigabine in the pore region.

Residues involved in Kv7.2 modulation by NH29

Next, we turned to the VSD to explore potential residues involved in Kv7.2 modulation by NH29. The Attali lab checked residues of helices S4 and S2 and of loop S1-S2 and characterized the biophysical properties of each mutant in the absence and presence of NH29 (25 μM). The sensitivity of each mutant channel to NH29 was quantified by measuring its ability to increase the current amplitude at a voltage yielding a normalized open probability of about 0.1 (Figure

4.4, D, E and G; Figure 4.5). In helix S4, mutant L200G demonstrated stronger stimulation by NH29 compared to *wt* Kv7.2 (5.5 ± 0.5 fold versus 3.5 ± 0.3 fold, n = 7-15, $p < 0.05$), while mutants L197G, R198A and two epilepsy-associated mutations, R207W and R214W (116), exhibited significantly weaker stimulation by 25 μM NH29 (1.4-, 1.6-, 1.5- and 1.1-fold, respectively; n = 8-15, $p < 0.001$) (Figure 4.4, D-H). Notably, NH29 produced a very weak left-shift, if any, of the activation curve of R198A and R207W mutant channels, compared to *wt* Kv7.2 (e.g., ΔV_{50} = +0.6 ± 2.6 mV and ΔV_{50} = -5.3 ± 0.9 mV for R198A and R207W, respectively, compared to ΔV_{50} = -15.5 ± 0.5 mV for *wt* Kv7.2, n = 8-15, $p < 0.01$; Figure 4.3D; Figure 4.4, E and F). In addition, in R198A and R207W mutants the kinetics of channel activation and deactivation were not appreciably affected by NH29, compared to *wt* Kv7.2 (Figure 4.4E, G and H). Noticeably, the S4 mutants, which were less sensitive to NH29, were highly responsive to other M-channel openers, retigabine (5 μM) and zinc pyrithione (10 μM) (128). In helix S2, mutant Y127A showed significant higher stimulation by NH29 compared to *wt* Kv7.2 (4.8-fold versus 3.5-fold increase, respectively; n = 8-15, $p < 0.01$; Figure 4.5A).

With these experimental constraints, I attempted to dock NH29 onto the 3D model-structure of Kv7.2 in an open conformation. The NH29 docking site was an external, water-exposed crevice within the VSD interface of helices S1-S4 (Figure 4.6A). Accordingly, I expected K120 in loop S1-S2, Y127 and E130 in helix S2, and R207 in helix S4, to affect the stability of the Kv7.2-NH29 complex, (Figure 4.6C and see Discussion). To further validate this docking model, the Attali lab checked the effects of NH29 on mutants K120A in loop S1-S2 and E130Q in helix S2. While NH29 induced similar left-shift of the activation curve of mutants K120A and E130Q compared to *wt* Kv7.2, it produced significant larger current amplitude stimulation compared to *wt* Kv7.2 (5.7- and 6.2-fold versus 3.5-fold, respectively, n = 8-15, $p < 0.01$; Figure 4.5), suggesting that the opener may also affect the channel conductance of these

mutants. In an attempt to explore the molecular basis for Kv7.2 specificity versus Kv7.1 for which NH29 does not act as an opener, the Attali lab transferred into Kv7.1 channel some relevant non-conserved Kv7.2 residues (K120, Y127 and L200). In addition, the paddle motif of Kv7.2, which includes the linker S4-S5 (Kv7.1-Kv7.2 S3b-S5), was swapped onto Kv7.1. NH29 (25 μM) did not significantly affect the chimera Kv7.1-Kv7.2 S3b-S5 and the single Kv7.1 mutants A150K and F157Y but inhibited by 38% the current amplitude of mutant Kv7.1 I230L (n = 3-8, $p< 0.01$). NH29 (25 μM) produced a strong inhibition (62%) of the chimera Kv7.1-Kv7.2 S3b-S5 bearing the double mutation A150K and F157Y (Kv7.1-Kv7.2 S3b-S5 double mutation) (n = 3-8, $p< 0.01$). The Attali lab attempted to generate chimeras where the entire VSD of Kv7.2 was swapped by that of Kv7.1 (Kv7.2-Kv7.1 S1-S4) and reciprocally (Kv7.1-Kv7.2 S1-S4). Unfortunately, these chimeras did not express functional channels to probe the impact of NH29.

To investigate the selectivity of NH29 for the VSD of Kv7.2 subunits within the M-channel heteromer complex Kv7.2/Kv7.3, the Attali lab co-expressed the Kv7.2 S4 mutants R198A and R207W with *wt* Kv7.3. Results indicate that despite co-expression with *wt* Kv7.3, the Kv7.2 S4 mutations dominate within the complex and lead to channels, which display significantly weaker stimulation by NH29 compared to *wt* Kv7.2/Kv7.3. These Kv7.2 S4 mutations were then introduced at homologous positions in helix S4 of Kv7.3 subunits (Kv7.3 R227A and Kv7.3 R236W, respectively) and were co-expressed with *wt* Kv7.2. NH29 potently increased the current amplitude of the latter channel complexes and produced significant left-shift of their activation curves similarly to *wt* Kv7.2/Kv7.3. These data suggest that NH29 mainly acts on the VSD of Kv7.2, but barely affect that of Kv7.3.

4.2 Model-structure, mutations and dynamics of the Kv7.1-KCNE1 complex (in collaboration with the lab of Prof. Attali; the experiments were performed by the lab of Prof. Attali)

The Kv7.1-KCNE1 complex

I modeled the 3D structure of an open state of the Kv7.1-KCNE1 complex. The KCNE1 TM helix is not uniformly conserved (Figure 4.7), and its interface with the Kv7.1 channel is expected to feature conserved amino acids, while its lipid-facing region should include variable residues. The model selected on the basis of this criterion (Figure 4.8) was correlated with experimental data regarding residue pairs that form disulfide-bonds when mutated to Cys (89-91). Indeed, these residue pairs, located in flexible regions in the model-structure, e.g., loops, resided at distances of less than 15Å from each other and could form disulfide links (92), overall supporting the predicted orientation of KCNE1 with respect to Kv7.1 (Figure 4.9; Table 3.1). Kang and colleagues' model of the Kv7.1-KCNE1 complex lacks KCNE1 residues 40-44 (41), preventing me from correlating it with the disulfide data.

Next, I used the model-structure of the Kv7.1-KCNE1 complex to investigate the effect of KCNE1 association on the intrinsic dynamics of the Kv7.1 channel. To this end, I analyzed the motion of the complex in comparison to the isolated channel. This was done using coarse-grained elastic network models, which are not sensitive to atomic details and are suitable for model-structures (106,129). Elastic network models are capable of exploring large-scale motions related to channel gating and inactivation (106).

Equilibrium dynamics of the isolated Kv7.1 channel

I used elastic network models to investigate global motions of the Kv7.1 channel using the available Kv7.1 model-structure (42). The Gaussian network model (GNM) was used to identify the dynamic domains and their cooperative motions. The eight slowest GNM modes of motion of the Kv7.1 tetramer emerged significantly above the rest in the eigenvalue spectrum (Figure 3.4) and represented the most important contributions to the overall motion of the channel. I analyzed

the shapes of the residues' mean square displacement plots in these modes and identified the minima, corresponding to hinge regions that coordinated the motion of dynamic domains in each mode. Hinges often mediate functionally-important motions in proteins (129), and, indeed, the majority of the hinge residues I identified are associated with various disease conditions, such as long QT syndrome and atrial fibrillation (Table 4.1).

GNM modes 1 and 2 shared the same eigenvalues (Figure 3.4) and were degenerate. The average shape of the residues' fluctuations in these two modes was very similar to that in the third mode (Figure 4.10). Thus, GNM modes 1–3 correspond to the same motion. Similarly, GNM modes 5–7 represented the same motion. Overall, I grouped GNM modes 1–8 into four types of motion (Table 4.2).

I then carried out anisotropic network modeling (ANM) analysis, which provides information on the directions of the motions in 3D-space. I looked for correspondence between the GNM and ANM modes, seeking to link the fluctuations (and correlations between fluctuations) detected by the GNM calculations to their directions, obtained from the ANM analysis. To this end, I compared the distributions of residue fluctuations in each mode (Figure 4.11; Table 4.2). I further validated the modes' associations by mapping the GNM-derived cross-correlations between residues on the conformations obtained via ANM (Figures 4.12, 4.13A and 4.14A).

Motions I and III described alternate slanting of VSD pairs from diagonally-opposite monomers towards the pore (Figure 4.12). The direction of slanting differed between motions I and III. Still, in both cases the slanting VSD pushed the external vestibule and P-loop of a neighbor chain towards the pore funnel (Figure 4.12). In motion II the VSDs were swinging, while the pore domain appeared to be essentially stationary (Figure 4.13A). In motion IV the

channel was divided into two dynamic domains, connected by hinges located approximately along the membrane mid-plane (Figure 4.14A). The two domains rotated in opposite directions, with the domain in the intracellular membrane leaflet rotating at significantly lower magnitude.

Equilibrium dynamics of the Kv7.1-KCNE1complex

To understand the effect of KCNE1 binding on the channel motion I conducted GNM and ANM analysis of the model-structure of the Kv7.1-KCNE1 complex. As the stoichiometry of the complex has not yet been definitively determined, I arbitrarily studied the (tetrameric) channel in complex with four KCNE1 molecules. I then matched the GNM and ANM modes of the complex to the motions of the isolated channel (Figure 4.11; Table 4.2). The matching was based mostly on the correspondence of the hinge regions of Kv7.1 in the presence and absence of KCNE1 (Figure 4.11). Overall, the patterns of the mean square displacement were essentially preserved upon KCNE1 binding, in all four motions and in both elastic models; complex formation primarily influenced the magnitude of the channel's fluctuations, i.e., relative mobility of residues. In addition, the cooperative dynamics of the complex resembled the dynamics of the isolated channel, supporting the match of the GNM and ANM modes in the presence and absence of KCNE1.

Comparison of GNM fluctuations revealed that for the most part the residue fluctuations were of lower magnitude in the KCNE1-Kv7.1 complex than in the isolated channel (Figure 4.11). The variations in the magnitude of the ANM fluctuations of the isolated channel versus the complex were more significant than those of the GNM fluctuations, especially in motions I, II and III (Figure 4.11). The decrease in fluctuation magnitude upon KCNE1 association was manifested mainly in the reduction of VSD fluctuations. In addition, motion III manifested

significant reduction in the fluctuations of the pore domain (Figure 4.11C). In contrast, the fluctuations of the S2-S3 linker in motions I, II and IV increased upon KCNE1 binding (Figure 4.11).

I also studied the influence of KCNE1 on the cooperative dynamics between structural elements. While only minor alterations were observed in motions I and III, more substantial changes were noted in motion II (Figure 4.13). In the isolated channel only a few VSD residues were positively correlated with the immobile pore domain, i.e., were also immobile (Figure 4.13A). Upon KCNE1 binding, however, a more substantial part of helix S1 was coupled with the pore domain (Figure 4.13B). Association with KCNE1 also led to variations in the residues' cross-correlations in motion IV, e.g., in G272, V310 and T311, located at the entrance to the selectivity filter (Figure 4.14). These residues manifested negative correlation with the rest of the selectivity filter in the isolated channel (Figure 4.14A), but positive correlation in the presence of KCNE1 (Figure 4.14B).

Experimental data (Performed by the lab of Prof. Attali, Tel-Aviv University)

To probe my structural model, the Attali lab examined the electrophysiological properties of Kv7.1 co-expressed with two KCNE1 mutants, Y46A and L63W, in comparison to the *wt* Kv7.1-KCNE1 channel, as described below. Y46 and L63 are evolutionarily conserved and located at the outer and inner boundaries of the KCNE1 TM segment, respectively (Figure 4.8). L63W activated with slower current kinetics compared to the *wt* complex, as measured by the time of half-maximal activation at +40 mV ($T_{1/2}$ = 1202 ± 95 ms vs. $T_{1/2}$= 952 ± 37 ms, respectively; n = 6-11, $p < 0.05$; Figure 4.15). In addition, L63W exhibited a faster deactivation rate in comparison to the *wt* (τ = 336 ± 23 ms vs. τ = 1642 ± 134 ms, respectively; n = 6-11, p < 0.01) and produced a marked rightward shift in the voltage dependence of channel activation (V_{50} = 22.5 ± 2.3 mV, s

= 7.9 ± 1.6 mV vs. V_{50} = 0.4 ± 1.5 mV, s = 14.3 ± 1.4 mV, respectively; n = 6-11, $p < 0.01$; Figure 4.15). In contrast to the L63W mutant, Y46A displayed faster activation kinetics compared to the *wt* complex, with a significant instantaneous current component ($T_{1/2}$ = 311 ± 32 ms vs. $T_{1/2}$= 952 ± 37 ms, respectively; n = 6-11, p < 0.01; Figure 4.15); its deactivation kinetics, like those of L63W, were faster than those of the *wt* (τ = 363 ± 62 ms vs. τ = 1642 ± 134 ms, respectively; n = 11, $p < 0.01$). Furthermore, Y46A induced a pronounced left shift in the voltage dependence of channel activation relative to the *wt* complex (V_{50} = 0.07 ± 0.9 mV, s = 22.5 ± 1.6 mV vs. V_{50} = 0.4 ± 1.5 mV, s = 14.3 ± 1.4 mV, respectively; n = 6-11, $p < 0.01$) and even exhibited a voltage-independent component by producing current at voltages negative to E_K (Figure 4.15). These results suggest that the KCNE1 mutants, Y46A and L63W, stabilize the open and closed states of the channel, respectively.

4.3 Model-structure of the human nucleotide-gated cone channel: implications for clinical mutations and gating

Evolutionary conservation profile of the cone channel model-structure

I modeled the 3D structure of the cone CNG channel, composed of pairs of CNGA3 and CNGB3 subunits, using two separate templates: the TM region was derived by homology from the TM region of the remotely homologous bacterial channel MlotiK1 in its closed state, whereas the cytosolic domain was derived by homology from the CNBD of mHCN2 in its resting state (Figure 4.16). To evaluate the resultant model, I projected the evolutionary conservation scores of the CNGA3 and CNGB3 subunits onto the full structure of the channel (Figure 4.17). The evolutionary conservation profile has been demonstrated to be a valuable tool for assessing model-structures (19). In the typical evolutionary conservation profile, the protein core is evolutionarily conserved, whereas residues that face the surroundings, either lipids or water, are

variable (19). The model-structure was compatible with this anticipation. For comparison, the evolutionary conservation profiles of the template proteins were projected onto their structures and also showed the expected conservation patterns (Figures 1.4B and 4.18). It should be noted that the conservation scores of the queries and the templates were calculated using distinct sets of homologs, contributing to the robustness of the observed conservation profiles.

Comparison with the available experimental data

Much of the available data related to the CNG channels was collected from experiments on bovine CNG channels. Here I compare the applicable data from these experiments to assess the model-structure of the human cone channel.

The structure of the central pore of the bovine CNGA1 channel has been assessed through cysteine-accessibility analysis, using cysteine mutations and cysteine-specific modifications (130,131). The available data on the accessibility of CNGA1 residues to the central pore were compatible with the model-structure (Figure 4.19A). Additionally, two CNGA1 residues, corresponding to L361 and F385 in CNGA3 and to R403 and F427 in CNGB3, have been shown to interact in the same CNGA1 subunit (132). In the model-structure the α-carbons of CNGA3 L361 and F385 (or CNGB3 R403 and F427) from the same subunit were 11 Å apart; the α-carbons of CNGA3 L361 and F385 (or CNGB3 R403 and F427) from the neighboring subunits were 9 Å apart (Figure 4.19B). The distances between the residues imply that both inter- and intra-subunit interaction between these residues is possible.

The C-linker, connecting the TM domain and the CNBDs, is composed of helices named A'-F' (Figure 4.20A). In the resting state, these helices are arranged in a compact tetrameric

structure, so that the first two helices, A' and B', interact with helices C' and D' from the neighboring subunit (Figure 4.20A). This structural motif has been called "elbow on a shoulder", where helices A' and B' are the "elbow", resting on a "shoulder" comprising helices C' and D' from the neighboring subunit (46). The interaction between the "elbow" and the "shoulder", in addition to interactions between other structural motifs of the C-linker and the CNBDs, have been recognized as functionally important (53,66). Specifically, in the bovine CNGA1 a triad of charged residues in the "elbow on a shoulder" structural motif was shown to stabilize the closed state of the channel (53,66). In CNGA3, residues R436, E467 and D507 correspond to the triad; in CNGB3 the triad corresponds to R478, A509 and D549. At the interface of two CNGA3 subunits, the α-carbons of residues R436, E467 and D507 are 11 Å apart from each other (Figure 4.20B). Evidently, R436 could form a salt bridge with E467 or D507 and stabilize either inter-subunit or intra-subunit interaction. Similarly, at the interface of the CNGA3 and CNGB3 subunits, CNGB3 R478 could form a salt bridge with CNGA3 E467 or D549 (Figure 4.20C).

Disease-causing mutations

I investigated known disease-causing mutations of CNGA3 and CNGB3 (Tables 1.1 and 1.2). As anticipated, almost all known mutations, i.e., all 10 mutations in CNGB3, and 37 of 45 mutations in CNGA3, were found to occur in evolutionarily conserved residues (Tables 1.1 and 1.2). Eight known disease-causing mutations in CNGA3 occur in variable residues, located in loop regions (Table 1.1). Only one of the latter mutations, namely E228K, has been investigated experimentally; it has been found to affect channel trafficking (69). This indicates that although E228K is not evolutionarily conserved, i.e., not important structurally, it plays a role in other aspects of channel function.

I mapped the known disease-causing mutations in the CNGA3 and CNGB3 subunits onto the model-structure (Figure 4.21). Predictably, the pore and the ligand-binding regions, as functionally important domains of the channels, featured several positions with known mutations. In addition, I observed that several mutations occur in positions promoting inter- and intra-subunit interactions in the C-linker (see an example below). Interestingly, in CNGA3 subunits, but not in CNGB3 subunits, the VSD and the interface of the C-linker with the S4-S5 linker contained several positions with disease-causing mutations. I speculate that the regions abundant with positions involved in disease are of special functional and/or structural importance.

The model-structure of the human cone channel can facilitate studies of disease-causing mutations and can be used to derive molecular interpretations of such mutations. Below I present three examples of achromatopsia-causing mutations.

CNGA3 R427C/CNGB3 Y469D. The disease-causing mutation R427C in CNGA3 is of special interest, because a mutation in the corresponding position in CNGB3 subunit, i.e., Y469, is also disease-causing (133,134). CNGA3 R427 is located in the A'-helix in the C-linker. Examination of the adjacent amino acids in the model-structure revealed that R427 can interact with E453, located in the C'-helix of the adjacent CNGA3 subunit (Figure 4.22A). R427 can also interact with CNGB3 D488, located in the loop connecting helices B' and C' of the C-linker of the adjacent CNGB3 subunit, and with E495, located in helix C' of the adjacent CNGB3 subunit (Figure 4.22D). I suggest that interaction between these charged residues stabilizes inter-subunit interfaces. More specifically, I suggest that the resultant hydrogen bonds stabilize the inter-subunit interactions, as in the above-mentioned triad (Figure 4.20, B and C) (53,66). Mutation of the positively charged R427 to Cys would abolish the electrostatic attraction to the negatively charged residues (CNGA3 E453 or CNGB3 D488 and E495; Figure 4.22, A and D). This might

disrupt the compact tetrameric architecture of the C-linker and CNBDs. In the mutation Y469D in CNGB3 (corresponding to CNGA3 R427), the negatively charged D469 might repel D488 and E495 of the adjacent CNGB3 subunit (Figure 4.22B), as well as E453 of the adjacent CNGA3 subunit (Figure 4.22C). In this case, the compact tetrameric architecture of the C-linker and CNBDs would be disrupted due to the electrostatic repulsion between the negatively charged residues.

CNGA3 L186F. CNGA3 L186 is located in the TM helix S1 of the VSD, at the helix's interface with the S5 helix and the p-loop (Figure 4.22E). Clearly, substitution of L186 with a bulky phenylalanine might disrupt the interface between the VSD and the pore domain. Moreover, in voltage-gated channels this interface has been shown to be functionally important (135). Although CNG channels are not voltage-dependent, and the role of the VSD in these channels is not clear, it is possible that the interface between S1 and the pore is still essential. Regardless of the functional role of the interface in CNG channels, its structure can be significantly disrupted by the L186F mutation.

CNGB3 S435F. CNGB3 S435 faces the central pore (Figure 4.22F), and its substitution with any large residue, e.g., F, may destroy the helix bundle, or simply block the pore. In fact, CNGB3 homologs each feature a small amino acid, either S, A or G, at the position corresponding to S435. This further supports the interpretation of the mechanism of the mutation.

Equilibrium dynamics of the CNGA3 channel in the holo-state

I used coarse-grained elastic network models to investigate global motions of the CNG channels. I chose this methodology because it is not sensitive to the atomic details of the (imprecise) model-structure and is capable of exploring large-scale motions, related to channel gating and inactivation (106,129). For simplicity and to facilitate more convenient representation of the data, I focused on a symmetric tetrameric channel composed of four identical CNGA3 subunits, with the CNBDs in the holo-state. GNM was used to identify the dynamic domains and their cooperative motions. The six slowest GNM modes of motion emerged considerably above the other modes in the eigenvalue spectrum (Figure 3.5). These modes, therefore, represented the most important contributions to the overall motion of the channel, and I investigated them. I analyzed the shapes of the residues' mean-square displacement plots in the six slowest GNM modes. GNM modes 2 and 3, as well as GNM modes 5 and 6, shared the same eigenvalues (Figure 3.5) and were degenerate. The average shape of the residues' fluctuations in modes 2 and 3 was very similar to mode 4, indicating that GNM modes 2–4 correspond to the same motion (Figure 4.23). Thus, GNM modes 1–6 represented three types of motion. Next, I carried out ANM analysis, which provided information on the directions of the motions in 3D-space. I sought to associate the fluctuations (and correlations between fluctuations) detected by the GNM to their directions, obtained from the ANM analysis. To this end, I compared the distributions of residue fluctuations in each ANM mode to the residue fluctuations in the GNM modes (Figure 4.24). I further validated the modes' associations by mapping the GNM-derived cross-correlations between residues on the conformations obtained via ANM (Figure 4.25).

In motion I, described by GNM mode 1 and ANM mode 3, the channel was divided into two dynamic domains, the TM domain and the cytosolic domain (Figure 4.25A). The two domains rotated around the membrane normal in opposite directions (Figure 4.25B). In motion II, described by GNM modes 2,3 and 4 and ANM mode 4, the VSDs were swinging, while the pore

domain, as well as the C-linkers and the CNBDs, appeared to be almost stationary (Figures 4.24B and 4.25D). A positive correlation was detected between the VSD, the C-linker and the CNBD of the same chain (Figure 4.25C). In motion III, described by GNM modes 5 and 6 and ANM mode 12, the pairs of diagonal CNBDs were alternately moving towards, and away from, each other (Figure 4.25F). A positive correlation was detected between the VSD and the CNBD with the C-linker of the adjacent chain (Figure 4.25E).

Interestingly, investigation of the 15 slowest GNM modes revealed that they can be categorized into modes in which only the TM domain is fluctuating (as in motion II) or modes in which only the cytosolic domain fluctuates (as in motion III) (data not shown). Thus, each domain fluctuates as an individual module. However, the observed cooperativity between domains suggests that they affect each other (Figure 4.25, C and E). This observation corroborates the modular gating model of the CNG channels, which postulates that the CNG channel domains can undergo conformational changes individually, but that the state of each module affects the states of other modules (66).

Equilibrium dynamics of the CNGA3 channel without VSDs

CNG channels are not regulated by the membrane potential, but VSDs are present in the CNG structure. The role of the VSD is not yet clear (51), although a recent study has shown that the domain is required for proper trafficking of the channel (136). In order to understand the effect of the VSDs on the channel motions, I performed GNM and ANM analysis of the CNGA3 channel in holo-state, removing the VSDs. Three GNM modes of motion emerged as the slowest in the eigenvalue spectrum (Figure 3.5). GNM mode 1 was associated with ANM mode 3 (Figure 4.26, A and B); this motion was very similar to motion I of the intact CNGA3 channel, in direction and

cooperative dynamics (Figures 4.25, A and B, and 4.26, A and B). GNM modes 2 and 3 were degenerate, and I related them to ANM mode 4 (Figure 4.26, C and D). This motion was similar to motion III described above, with the exception of the positive correlation detected in the complete channel between the VSD and the CNBD (with the C-linker) of the same chain (Figures 4.25, E and F, and 4.26, C and D). These findings indicate that the presence of VSDs does not significantly affect the slowest modes of motion of CNG channels, aside from the motions that directly involve the VSDs.

Equilibrium dynamics of the CNGA3 channel in the apo-state

According to the crystal structures of the apo- and holo-states of the mHCN2 CNBD, the CNBD undergoes only minor conformational changes upon ligand binding (Figure 4.18). I aimed to assess whether these conformational changes influence channel motion. To this end, I modeled the CNGA3 channel in the apo-state and performed a separate elastic network analysis. As in the analysis of the holo-state, I observed that the six slowest GNM modes of motion had considerably high eigenvalues, and I focused on them (Figure 3.5). In the apo-state, residue fluctuations in GNM and ANM modes of motion were nearly identical to the fluctuations of the channel in the holo-state (data not shown). There was no change in the cooperative dynamics of the six slowest GNM modes (data not shown). These observations suggest that the slowest modes of motion of CNGA3 are not affected by the minor conformational changes in the CNBDs induced by ligand binding.

5. Discussion

5.1 Targeting the voltage sensor of Kv7.2 channel with a new gating-modifier

The results of this study suggest that the new Kv7.2 channel opener, NH29, acts as a gating modifier. NH29 increases Kv7.2 current amplitude by affecting channel gating, thereby producing a hyperpolarizing shift of the activation curve. In addition, NH29 significantly reduces both activation and deactivation rates.

So far, retigabine is the most extensively characterized Kv7 channel opener. Retigabine docks to a pore hydrophobic pocket, which is formed by the cytoplasmic ends of helices S5 and S6 (125-127) (Figure 4.6A). The presented data clearly indicate that NH29 does not interact with the retigabine site on Kv7.2, as it can potently stimulate the retigabine-insensitive mutant W236L and left-shifts its voltage-dependence of activation.

Among the residues tested in S4, two mutants, L197G, R198A and two epilepsy mutations, R207W and R214W (116), exhibit significantly weaker stimulation by NH29 compared to *wt* Kv7.2. In contrast, mutants L200G in S4, K120A in loop S1-S2, E130Q and Y127A in S2 show significantly higher activation by NH29. The S4 mutants that are much less sensitive to NH29 (e.g., R198A and R207W) are potently activated by M-channel openers acting at the pore region like retigabine and zinc pyrithione, suggesting that these molecules interact with a different target from NH29 on Kv7.2 subunits. Thus, the results suggest an NH29 interaction with the VSD of Kv7.2 subunits. Docking data indicate that NH29 interacts with the external groove formed by the interface of helices S1, S2 and S4 in a pocket formed by the bulky residues K120 in loop S1-S2, Y127 and E130 in helix S2, L200 and R207 in helix S4 (Figure 4.6, A and B). The docking model of NH29 predicts that a nitro group of one aromatic ring is engaged in hydrogen-bonding with the guanidinium of R207 in S4 and with the carboxylate of

E130 in S2 (Figure 4.6C). In addition, the carbonyl oxygen of the NH29 amide function also forms hydrogen-bonds with the hydroxyl of Y127 in S2. In this orientation, the hydroxyl group of NH29 lies close to the aromatic ring of Y127, consistent with the formation of a hydrogen bond with the π-electrons of Y127. Remarkably, in the open state the guanidinium of R207 and the carboxylate of E130 are sufficiently close to form a salt bridge. The docking model suggests that in the presence of NH29 this interaction could be stabilized, which favors the activated VSD conformation (Figure 4.6C). The mutation R207W destabilizes the interaction with NH29, while in E130Q the nitro group of NH29 can still interact via H-bonding with the glutamine side chain and the guanidinium of R207 and even act as a surrogate of E130. In the closed state, the S4 helix rotates and moves downward leading R207 to interact with E140 (10,137). I speculate that NH29 stabilizes the Kv7.2 channel open state by preventing this movement. In the docking open state model, the S4 residue R198 whose mutant A198 displays significant weaker stimulation by NH29, does not face NH29; instead, it is located at 180° opposite to the molecule. I suggest that R198 interacts with NH29 in the closed state, in line with the electrophysiological data.

Despite the overall agreement between the computationally suggested binding mode of NH29 and the mutagenesis data, one should keep in mind the inherent limitations of small molecule docking protocols. Such procedures involve searching for ligand binding site(s) in a query protein and the prediction of the preferred positioning of the ligand in the sites(s), and a scoring function to estimate its binding affinity. In this study, in the absence of a high-resolution structure, a homology model of human Kv7.2 was used, increasing the uncertainty of the procedure. Although the protein backbone is expected to be of relatively high accuracy, the side chains' orientation is based on rotamer libraries and, therefore, presumably imprecise. The LigandFit method that I used (75), akin to most docking protocols, treats proteins as rigid bodies to make the search process computationally feasible, thus, side chains movements were not

included. Moreover, any other possible protein rearrangements taking place upon ligand binding were left out as well. To evaluate ligand positions obtained with a search algorithm, scoring functions were exploited. Scoring functions use approximations and simplifications to moderate their complexity with a consequent cost in terms of accuracy. The results of three different scoring functions were combined in order to reduce the risk. Clearly, further mutagenesis data will be necessary to increase the structural constrains and refine the docking model.

Additional residues in the Kv7.2 VSD are likely involved in NH29 interaction and need to be further identified. The results with the chimera Kv7.1-Kv7.2 S3b-S5 indicate that swapping helices S3 and S4 is not enough to recover the opener effect of NH29. In line with the docking data, the whole VSD (S1-S4) is apparently necessary to retrieve the opener action of NH29. Unfortunately, the lack of functionality of fully swapped VSD chimeras Kv7.2-Kv7.1 S1-S4 and Kv7.1-Kv7.2 S1-S4 prevented a confirmation of the necessity of the whole VSD for supporting NH29 opener action. This lack of functionality of fully swapped VSD chimeras was already emphasized by Alabi et al. (27). Nevertheless, it is interesting to notice that the chimera Kv7.1-Kv7.2 S3b-S5 double mutation converts the opener effect of NH29 into a strong inhibition, supporting the view that this region is important for NH29 interaction. This notion is reminiscent to the finding that a point mutation (S512Y), in the loop S1-S2 converts the VSD targeted TRPV1 antagonist iodoresiniferatoxin into an intrinsic agonist (138). The presented data are in line with a recent study suggesting that the Kv7.2/3 channel opener ICA-27243 may interact with the VSD (139).

Specific residues, found to be critical for the opener action, are also key positions in structural interactions between helices S2 and S4. In Kv7.2, charged residues E130 in S2 and R207 in S4 are homologous to E283 and R371, respectively, in *Shaker* channel, where they were

shown to interact electrostatically (140). E283 and R371 interact in the activated conformation of the VSD (140). The presented data suggest that NH29 resides in the S2-S4 interface and contacts both R207 and E130 in the channel open state. Interestingly, combining charge reversal mutations in *Shaker* channel, a previous study (140) showed that the double mutant, E283R+R371E, left-shifts the channel conductance-voltage relation and slows down the kinetics of activation and deactivation. These features are very similar to those exerted by NH29 on *wt* Kv7.2. I suggest that NH29 stabilizes the interaction between E130 and R207, thereby increasing the relative stability of the activated state as well as the heights of energetic barriers for transitions into and out of the open state.

The mechanism of NH29 activation of the Kv7.2 VSD may be similar to that of gating modifier toxins. The VSD of voltage-gated Na^+ channels is the target of polypeptide toxins from scorpions and sea anemones. These toxins bind to the S3–S4 loop at the outer end of S4 segments of Na^+ channels and impede their movements during gating (34). Hence, α-scorpion and sea-anemone toxins specifically block inactivation by holding the S4 of domain IV in its inward position, while β-scorpion toxins enhance activation of Na^+ channels by holding the S4 of domain II in its outward position (34). Similarly, hanatoxins from tarantula venom bind to the S3–S4 loop of Kv2.1 K^+ channels and inhibit their activity by right-shifting the voltage dependence of activation (33). Interestingly, the vanillotoxin VaTx1 from tarantula venom, not only inhibits Kv2.1 in a similar manner to hanatoxin but also activates TRPV1 channels (32,33). Along this line, the preliminary data from the Attali lab intriguingly showed that in addition to activating Kv7.2 K^+ channels, NH29 is also a potent blocker of TRPV1 channels with an IC_{50} of 4.2 μM. NH29 changes the rather linear TRPV1 current-voltage relation obtained with capsaicin, to an outwardly rectifying shape. A voltage-sensor trapping mechanism was suggested to be the

molecular basis of action of polypeptide toxins that alter the voltage dependence of channel gating (34). Such mechanism may also operate for NH29.

In conclusion, the modular nature of the VSD and its rather unexploited targeting by drugs makes this strategic domain an important pharmacological target. The presented data provide a framework for designing non-toxin gating-modifiers of voltage-gated cation channels to treat hyperexcitability disorders.

5.2 Model-structure, mutations and dynamics of the Kv7.1-KCNE1 complex

Limitations of the calculations

I presented a 3D model-structure of the Kv7.1 channel in complex with its regulatory unit KCNE1, and correlated it with empirical data. Despite the overall agreement between the model and experimental data (Figure 4.9), one should keep in mind some inherent limitations of the approach. As high-resolution structures were not available, I used a homology model of human Kv7.1 (42) and an *ab-initio* model of KCNE1. An NMR structure of KCNE1 is available (41), but it was determined in micelles and might differ from the structure in a bilayer (79). Specifically, the helix corresponding to the TM segment displayed a curvature consistent with the micelle radius, and its precise structure within the context of the Kv7.1-KCNE1 complex is still under debate (41,80). The backbone model of Kv7.1 is expected to be close to the native structure; indeed, it fits the expected evolutionary conservation pattern (Figure 5.1). In contrast, the KCNE1 model might deviate from the real structure, e.g. in the curvature of the TM segment.

In both elastic network models utilized here, the protein structure is simplified into α-carbons connected by hookean springs of identical force constant (107-110). Thus, the models do not depend on the identity of the amino acids and the specificity of their interactions. Moreover,

the models do not depend on the atomic details of the structure and can tolerate small variations in topology (106,129). This is particularly important in the current study as I utilized model-structures of both Kv7.1 and KCNE1. Indeed, the magnitude and direction of the Kv7.1 fluctuations presented here were very similar to those observed in previous studies of potassium channels, in which high-resolution structures, still represented using α-carbons only, were used (103-105). In particular, my current results regarding Kv7.1 were very similar to those of the earlier analysis of the Kv1.2 channel (103), but here I separated modes 4-8 into three motion types, rather than investigating them collectively. The two channels share the same fold; in fact, the Kv7.1 model-structure was inferred from the Kv1.2 crystal structure by homology (42). Because the two channels share the same architecture, they also manifest very similar amino-acid contact maps, and subsequently most of their hinges are observed in similar structural locations (Table 4.1). Ligand-gated ion channels also share a similar TM domain, and are expected to manifest many of the motions of Kv1.2 and the other voltage-gated channels. However, they also feature the distinctive ligand binding domain (1), which should add unique motions.

By definition, elastic network models are not capable of reflecting major conformational changes. Offering possible directions of protein motions, ANM provides only hints as to conformations located close to the initial structure in conformational space. Still, several studies have demonstrated that the slowest (softest) modes describe relevant features of large-scale functional conformational changes, suggesting paths from the global energy minimum and depicting collective changes in the conformation (129). A protein's intrinsic modes of motion are determined by its architecture, making it possible to predict conformational changes from the structure (106). Elastic network models are capable of capturing these intrinsic conformational changes, including changes that are dependent on external stimuli such as voltage. In what

follows I propose potential functional roles for the channel motions described above and for the effects of KCNE1 on these motions.

The lower mobility of the VSDs in motion II upon channel association with KCNE1 and slow deactivation

Motion II mainly describes the fluctuations of the VSDs (Figure 4.13). The movement of the VSDs is further transmitted to the S4-S5 linkers (Figure 4.11B), suggesting that it could be related to channel closure and deactivation. To examine this possibility (and in the absence of a structure of a voltage-gated potassium channel), I compared the model-structure of the open state of Kv7.1 that was used here to the crystal structure of the bacterial potassium channel MlotiK1 in its closed state (51). The two channels share a similar fold, although the latter does not display voltage-dependent activity (141). Interestingly, the fluctuations of the VSDs in motion II resemble the transition of Kv7.1 into the conformation captured for the closed state of the MlotiK1 channel (Figure 5.2, A and B). This supports the association of motion II with deactivation.

Upon channel association with KCNE1 the magnitude of the VSD fluctuations decreases (Figure 4.11B). Additionally, in the complex, a more substantial part of the S1 segment is coupled with the immobile pore domain (Figure 4.13B) as compared to the isolated channel (Figure 4.13A). Both observations indicate lower mobility of the VSDs upon KCNE1 association, consistent with the fact that deactivation of the complex is slower than that of the isolated channel (35,142).

Molecular interpretations of the Y46A and L63W mutants

Overall, the model-structure of the complex manifests the anticipated correlation between the buried vs. exposed nature of the amino acids and their evolutionary conservation. Namely, KCNE1 residues that are buried at the interface with Kv7.1 are conserved, whereas residues that are exposed to the lipid are variable (Figure 4.8B). However, the C-terminal extension of the TM helix shows a patch of evolutionarily conserved and exposed residues in close proximity to each other, including L63 and R67 (Figure 4.8B). Patches of conserved and exposed residues are often important for interaction (143), and I suggest that this patch could fulfill a role in the closed state of the channel. In particular, I suggest that upon deactivation, the VSD moves towards KCNE1 (Figure 5.2, A and C), so that the S1 segment interacts with the conserved patch. All KCNE1 homologs, aside from one, feature Leu or Val in position 63 (Figure 5.3), and the mutation to Trp might promote aromatic-stacking interaction with F123 and/or F127 of S1 of the channel (Figure 5.2C). The interaction between these aromatic residues may stabilize the closed state of the channel (144). This could explain the observed slow activation and fast deactivation of the channel when co-expressed with the KCNE1 L63W mutant (Figure 4.15) as a shift of the channel population towards the closed state. For comparison, in the model-structure by Kang et al. (41) L63 is located in a rather tight interface with Kv7.1 S1 (Figure 1.5), and its mutation to Trp would oppose the movement of S1 (Figure 5.2) and destabilize the closed state, which should produce the opposite effect, in conflict with the experimental data (Figure 4.15).

The Y46A mutant showed different behavior; electrophysiological studies showed that activation and deactivation in Kv7.1 co-expressed with this KCNE1 mutant were faster than those of the *wt* complex, comparable with those of the isolated Kv7.1 channel (Figure 4.15C). All KCNE1 homologs feature Tyr or Phe in position 46 (Figure 5.3). Y46 is tightly packed against the bulky W323 and V324 of the channel (Figure 5.2C), and replacing it with a small Ala residue

would loosen the tight Kv7.1-KCNE1 interface, reducing the regulatory effect of KCNE1. This could explain why the electrophysiological recording of the Y46A mutant resembled that of the isolated channel in activation, deactivation and even inactivation (Figure 4.15C). It is noteworthy that Y46, W323 and V324 are all within a cluster of residues that form a hinge in motion II (Figure 5.3; Table 4.1), and could be involved in the regulation associated with this motion. In this respect, the observed similarities between the electrophysiological recordings of the Y46A mutant and those of the *wt* isolated channel (Figure 4.15C) could be related to deficiencies in motion II. For comparison, in the previous model-structure of the complex Y46 faces the lipid (41), making it difficult to explain the effect of the mutation (Figure 1.5).

Immobilization of the pore region in motion III and voltage-dependent inactivation

In motion III pairs of juxtaposed VSDs lean alternately towards the pore (Figure 4.12). The resulting distortion in the selectivity filter resembles fluctuations previously associated with inactivation of the prokaryotic channel KcsA (145-148). It has previously been demonstrated that KcsA and Kv7.1 share the same inactivation mechanism (149), and I therefore suggest that motion III is related to Kv7.1 inactivation. Kv7.1 displays two types of inactivation: one is fast and voltage-independent, and the other is slow and voltage-dependent (150). In motion III each VSD is divided into two dynamic domains: the first includes the paddle motif, namely the C-terminus of the S3 and S4 segment, S1, and the N-terminus of S2; the second domain includes the C-terminus of S2, the S2-S3 linker, and the N-terminus of S3 (Figure 4.12B). The paddle motif is thought to drive conformational changes in response to membrane-voltage variations (10). In motion III it is decoupled from the rest of the VSD, and I suggest that this motion is associated with voltage-dependent inactivation.

Upon association with KCNE1 the fluctuations of the external vestibule and P-loop of Kv7.1 are significantly lower as compared to those of the isolated channel, especially according to the ANM calculations (Figure 4.11C). Given that fluctuations of the external vestibule and selectivity filter are essential for inactivation, a decrease in the fluctuations in these regions could indicate dampening, or even elimination, of inactivation. Indeed, one of the known effects of KCNE1 on Kv7.1 is abolishment of voltage-dependent inactivation (150-154).

D317 and E295 may play a role in voltage-dependent channel-inactivation

Previous studies have highlighted the importance of the interaction between residues E71 and D80 for inactivation of the KcsA channel (Figure 5.4, A and B) (145-148). Those studies demonstrated that electrostatic repulsion between the two residues hindered the approach of the external vestibule towards the funnel and the conformational changes in the selectivity filter region; neutralization of either of these residues enhanced inactivation (145,146). ANM analysis of KcsA yields results compatible with these observations (104,105), as in one of the two most contributing motions the external vestibules of juxtaposed chains move towards each other, so that E71 is pulled towards D80 (104,105). For illustration and comparison I repeated the ANM studies of KcsA using the HingeProt server (110) (Figure 5.4, A and B).

Kv7.1 has a negatively charged residue in position D317, which is equivalent to D80 in KcsA, but a hydrophobic residue in position V308, which is equivalent to E71. Assuming that the inactivation mechanism in Kv7.1 is similar to that in KcsA (149), I searched for an additional negatively charged residue in the external vestibule of Kv7.1. E295 emerged as a candidate, since it is located in the vicinity of D317; the distance between the α-carbons of D317 and E295 is about 10Å, similar to the distance between the α-carbons of E71 and D80 in KcsA (146). Of the other negatively charged residues in the region, namely E284, D286, E290 and D301 (Figure

5.4C), the first three are too distant from D317 to contribute significantly to the repulsion, while D301 is conserved in all Kv7 family members (including Kv7.2), regardless of their inactivation properties. In motion III, E295 approaches D317 when the VSD and external vestibule lean towards the pore funnel (Figure 5.4, C and D). Mutation of E295 or D317 to Ala amplifies voltage-dependent inactivation of Kv7.1 (113). Moreover, I examined the sequences of the other Kv7 family members undergoing slow inactivation and observed that Kv7.4 and Kv7.5 each have a negatively charged residue at the position corresponding to E295 (D266 and E294, respectively). The Kv7.2 channel, in contrast, does not undergo inactivation upon depolarization, and features H260 in the equivalent position. Thus, I suggest that the electrostatic repulsion between E295 and D317 hinders voltage-dependent inactivation of Kv7.1, similarly to the repulsion between E71 and D80 in KcsA.

Changes in the cross-correlations in motion IV and enhanced conductivity

The rotation displayed in motion IV has been investigated experimentally and computationally (103-105,155,156), and associated with gating. Roughly speaking, the motion divides the channel into two dynamic domains that rotate in opposite directions around hinges in the membrane mid-plane (Figure 4.14, A and B). In the presence of KCNE1, residues G272, V310 and T311 shift from one dynamic domain to another, i.e., change the sense of their cooperative motion, so that all residues in the pore region (and the channel's dynamic domain located in the intracellular membrane leaflet) move together (Figure 4.14C). With these residues, the pore region rotates as a whole rather than in part, which is expected to increase conductance. This could explain the increased K^+ ion current through the channel upon KCNE1 association (35), indicating that the three residues mentioned above should be considered as a regulatory switch for enhanced conductivity.

Further support for this notion emerges from the fact that mutation of V310 to Ile in Kv7.1 results in substantially lower currents (157,158). V310 and T311 (corresponding to KcsA A73 and T74) are located at the entrance to the selectivity filter and interact with F272 and F273 in S5 and F340 in S6 (corresponding to KcsA V39, L40 and F103; Figure 4.14, B and C; Figure 5.5). These five residues are involved in channel inactivation, deactivation and selectivity (148,153,157-161); disease-causing mutations in four of them are well known (42). Indeed, it has recently been suggested that in potassium channels selectivity and inactivation are linked, with F340 in Kv7.1 (or the corresponding position in other channels) and residues interacting with it serving as the link (149).

In conclusion, I presented here elastic network analysis of the equilibrium dynamics of the model-structure of the Kv7.1-KCNE1 complex. The model-structure is compatible with the typical evolutionary conservation pattern and with available disulfide mapping studies. Furthermore, it suggests molecular interpretations for electrophysiological phenomena that was observed by the Attali lab, Tel-Aviv University, in the channel co-expressed with two KCNE1 mutants. Elastic network analysis of the model-structure revealed interesting details with regard to channel deactivation, inactivation and gating, suggesting important roles for D317 and E295 in channel inactivation and for G272, V310 and T311 in conductivity. Moreover, it enabled me to formulate a mechanistic perspective of how KCNE1 binding affects channel dynamics. Slow deactivation was attributed to the low mobility of the voltage sensor domains upon KCNE1 binding; abolishment of voltage-dependent inactivation resulted from the decreased fluctuations in the external vestibule; amalgamation of the fluctuations in the pore region was associated with the enhanced conductivity of the channel.

5.3 Model-structure of the human nucleotide-gated cone channel: implications for clinical mutations and gating

Comparison with KirBac channels indicates that motion I is related to gating

Motion I is a rotational, iris-like motion (Figure 4.21A), similar to a motion previously described for potassium channels and associated with gating (104,105,162). Here I compare this motion with gating in KirBac channels, prokaryotic homologs of mammalian inwardly rectifying potassium channels. KirBac channels share architecture of the pore domain with other members of the voltage-gated-like ion channel superfamily, and they lack VSDs. Similarly to CNG channels, KirBac channels feature a cytoplasmic domain interacting with regulatory molecules, such as G-proteins, ATP and PIP_2 (163). Recent crystal structures of the KirBac3.1 channel in its open and closed states have provided interesting insight into the gating mechanism of the channel (Figure 5.6A) (164,165). Comparison of the crystal structures of KirBac3.1 has revealed that upon activation the TM and cytoplasmic domains rotate in opposite directions around the membrane normal (164). For comparison, I performed elastic network analysis of the KirBac3.1 channel in its closed state. The slowest GNM mode was associated with the slowest ANM mode, which displayed the same rotational motion of the TM and cytoplasmic domains as described by the structural studies (164). The conformational changes that would result from this type of motion resemble the conformational changes observed in the crystal structures, i.e., the shift between the open and closed states (Figure 5.6, A and B). This finding reconfirms the power of elastic network models to capture large conformational changes associated with function. Because motion I of the CNGA3 channel (Figure 5.6C) is analogous to this rotational motion of KirBac1.3 (Figure 5.6B), I propose that it is related to channel gating.

The idea of a rotational motion related to the gating of CNG channels is not new (166,167). Flynn and colleagues used existing experimental evidence to validate involvement of a clockwise rotation of the C-linkers in channel gating (reviewed in (167)). The authors also stated that a gating model including a rotational motion requires definition of a 'pivot point', such that the residues above the pivot point rotate counterclockwise, and the residues below the pivot point rotate clockwise. They proposed that in CNG channels the pivot point is located at the top of the S6 helices. The elastic network analysis shows that the clockwise rotation of the cytosolic domain is indeed coupled to counterclockwise rotation of the TM domain (Figure 4.25A), an observation compatible with their proposition and with the gating mechanism of the KirBac channels (164). However, the pivot point is located at the C-termini, rather than at the top, of the S6 helices (Figure 4.25A).

Although CNG and KirBac channels display similar rotational motion upon gating, there is a principal difference between the two channels. The KirBac channel contains two gates: one in the center of the S6 helix (near the p-loop) and one at the C-termini of the S6 helices (Figure 5.6A) (164). In contrast, in the CNG channels only a single gate was found in the pore region (59,167). I propose that in the absence of the second gate in the CNG channels, the VSDs provide an additional means of gating regulation. This conclusion derives from a close investigation of the rotational motion of the full-length CNGA3 channel (Figure 5.6C) and that of the CNGA3 channel lacking the VSDs (Figure 5.6D). In the absence of the VSDs (Figure 5.6D), the fluctuations of the N-termini of the S6 helices are greater in magnitude than they are in the full-length channel (Figure 5.6C). Thus, in the presence of the VSDs the pore region is rigid, so that the fluctuations in the gate region are limited. In the absence of the VSDs (also in KirBac channels, which lack the VSDs), the pore region is more flexible. Therefore, more strict regulation of gating is required. This could explain why KirBac channels, which lack VSDs, have

an extra gate at the C-termini of the S6 helices (164), whereas CNG channels, which contain VSDs, have only one gate.

Limitations of the study

The approach used to predict the structure has certain drawbacks. First, the TM region of the channel was derived from the structure of a distant bacterial homolog, MlotiK1, with very low sequence identity (~10%) between the queries and the template. This may have led to inaccuracies due to errors in the alignment of the query and template sequences, as well as structural changes along the course of evolution. However, the fact that the model-structure fits the expected evolutionary pattern and the available experimental data is encouraging (Figures 4.17, 4.19 and 4.20). Second, the model-structure of the cone channel was derived from two distinct templates. Therefore, the interface connecting these templates in the model, i.e., the S6-C-linker region, might be incorrect. Lastly, the loop regions in any model-structure are presumably imprecise (15). To examine the effect of the loop conformations on the results of the elastic network analysis, I repeated the analysis, omitting the loops. Reassuringly, the results were very similar. This outcome also validates the offered conclusions for other channels of the CNG family, inferred on the basis of the analysis of the CNGA3 channel.

A different approach in homology modeling includes generation of a number of structural models rather than a single model-structure. This approach is often applied in two cases: the first case involves uncertainty in the query-template alignment; the second case involves modeling of regions absent from the template and essential for the scientific question asked. Indeed, query-template alignment is the most critical step in homology modeling (15). When the query-template alignment is uncertain, generating an ensemble of model-structures can cover all possible

alignment variations. The intrinsic traits of membrane proteins decrease the uncertainty in the query-template alignment, often leading to a single optimal solution. These traits include a high abundance of hydrophobic residues in the TM segments, the existence of "aromatic belts", i.e., an abundance of Trp and Tyr residues near the termini of the TM helices, as well as the tendency to bury conserved and polar and charged residues in the protein core, and expose variable and hydrophobic residues to the lipids (15). Given a pairwise alignment between the query and the template, only a single solution is possible for the secondary structure elements; the loops connecting the secondary structure elements are in fact modeled ab-inito, and multiple solutions are possible. If one needs to explore the conformational space of flexible loops to gain biological insights, then an ensemble of conformations is indeed required. This is not the case when exploring global motions of ion channels, for example; indeed, elastic network analysis was unaffected by the presence of loops.

The structure of the cytosolic domain of the cone channel, including the C-linkers and the CNBDs, was derived by homology from the crystal structure of the corresponding domain of an HCN channel (see "Methods and Materials"). However, the resemblance of CNG CNBDs to HCN CNBDs has been questioned previously (168), on the basis of several experiments performed on bovine CNG channels. For instance, the A'-helix from the C-linker have been demonstrated to be close to the β-strands from the CNBD of the same subunit (169,170); clearly, this contradicts the model-structure derived from the crystal structure of mHCN2 CNBD (Figure 4.20A). Conversely, triads of negatively charged residues (Figure 4.20, C and D), present in corresponding positions of the mHCN2 and bovine CNGA1 channels, have been shown to stabilize the closed states of both channels (53,66). Moreover, the model-structure revealed a cluster of disease-causing mutations in positions that, like those triads, potentially promote inter- and intra-subunit interactions of the C-linker (Figure 4.21). These observations indicate that the

cytosolic domains of HCN and CNG channels in closed conformation could share structural similarities. It is also imaginable that more than one closed state exists for both CNG and HCN channels, resolving the contradicting experimental data.

Given the above-mentioned weaknesses of the presented model-structure, the choice to use elastic network models to study the channel dynamics is rational. As mentioned above in section 5.1, in both GNM and ANM, the channel structure is simplified into α-carbons, making the methodology suitable for investigation of model-structures (106,129). Moreover, GNM and ANM are capable of capturing large-scale conformational changes, including changes that are dependent on external stimuli such as voltage or ligand binding (106).

Using the model-structure of the CNG channel I have provided molecular interpretations of three achromatopsia-causing mutations. One might have expected a more extensive investigation that could include, for instance, a quantitative analysis of disease-causing mutations and their conservation scores, or analysis of non-deleterious mutations, etc. However, such investigation requires extensive experimental and/or clinical data that could unanimously determine mutations effect, supporting or disapproving theoretical predictions. The lack in the experimental information precludes profound studies of mutations effects in case of the CNG channel, as well as in case of many other human proteins.

To conclude, I presented a 3D model-structure of the human cone channel, composed of CNGA3 and CNGB3 subunits. The model-structure provides a structural framework for investigation of disease-causing mutations of the cone channel, enabling me to propose molecular interpretations for several such mutations. I performed elastic network analysis of the homomeric CNGA3 channel and obtained a mechanistic view of the gating of CNG channels. I suggest that the slowest mode of motion, describing counter-rotations of the TM and cytosolic domains

around the membrane normal, depicts channel gating. The VSDs appear to play a role in gating, supplementing the sole gate in the pore. Furthermore, the presented results support the modular gating mechanism of CNG channels (57,66). Lastly, the resemblance in fluctuations of the CNGA3 channel in the apo- and holo-states is in line with experimental evidence showing that the CNG channel can open in the absence of a ligand (63,70).

Tables

Table 1.1. Investigation of known disease-causing mutations in CNGA3. ConSurf grades were calculated using the ConSurf server (83), as described in the "Methods and Materials" section. The "Position occupancy in homologous proteins" column describes all possible amino acids featured in the corresponding positions in homologous sequences. Positions with a ConSurf grade of less than five are underlined. The "Experimental verification" column shows studies that identified the mutation and states whether experimental verification of the mutation was performed.

Mutation	ConSurf grade	Location in the model-structure	Position occupancy in homologous proteins	Experimental verification (reference)
Y181C	7	S1	A,W,M,I,G,Y,V	No (134)
N182Y	8	S1	H,Q,T,N,I,V	No (134)
L186F	6	S1	T,C,I,L,V	No (134)
C191Y	6	Loop S1-S2	F,S,A,T,C,G,V	No (134)
E194K	2	Loop S1-S2	F,S,T,N,K,Y,E,V,Q,C,L,A,P,H,D,R	No (134)
R223W	8	S2/Loop S2-S3	F,H,N,I,R	No (133,134,171)
T224R	8	S2/Loop S2-S3	S,M,T,K,I,E,L,V	No (134)
E228K	4	Loop S2-S3	F,S,T,N,K,E,V,H,Q,D,I,R,G,L	No (134); impaired trafficking (69)
F249S	8	S3	S,A,F,W,L	No (133)
D260N	8	S3	S,D,G,Y,L,E	No (134)
Y263D	4	S3	A,F,N,Y,H,Q,M,C,I,L	No (133)
G267D	3	S3-S4 loop	F,S,N,K,P,E,V,H,Q,D,I,G,L	No (134)
R277C/H	8	S4	Q,D,K,R	No (133,134); no channels formed (172)
R283Q	8	S4	A,S,T,P,K,Q,C,R	No (134,173); Impaired trafficking (69)
T291R	5	S4-S5 linker	F,S,W,T,P,K,V,M,R,I,L	No (134,173); Decreased cGMP sensitivity; impaired trafficking (69)
S341P	1	Loop S5-P-loop	F,S,T,N,K,Y,E,V,M,L,A,P,D,I,R,G	No (133,134)
T369S	7	SF	S,A,T,N,K,V,H,Q,M,D,R,L	No (134)
P372S	8	Loop P-loop-S6	S,A,P	No (134)
F380S	8	S6	F,M,I,L,Y	No (134)
S401P	7	S6	A,S,T,N,D,E	No (133)
M406T	7	S6	S,A,E,V,M,R,I,L	No (134)
R410W	7	A'-helix	S,A,T,K,E,H,Q,D,R,G	No (133,134,173)
R427C	7	A'-helix	F,N,K,Y,H,Q,M,R,L	No (133,134)

Mutation	ConSurf grade	Location in the model-structure	Position occupancy in homologous proteins	Experimental verification (reference)
R436W	8	B'-helix	Q,K,R,G,E	No (133,134,171)
R439W	5	B'-helix	S,T,K,E,H,Q,M,D,R,L	impaired trafficking (69)
A469T	7	D'-helix	S,A,T,K,Y,V,C,D,I,G,L	Increased cGMP sensitivity (69)
N471S	6	D'-helix	A,F,S,N,E,Y,H,Q,D	No (134); Increased cGMP sensitivity (172)
D485V	4	F'-helix	S,A,T,N,K,E,H,Q,D,G,L	No (134)
C510S	8	β-roll	F,C,I,L,Y,V	No (134)
G513E	9	β-roll	H,N,G,E	No (134)
G516E	8	β-roll	A,I,G,L,V	No (134)
I522T	9	β-roll	I,V	No (134)
G525D	9	β-roll	G	No (134)
L527M	8	β-roll	F,A,M,I,L,V	No (134)
V529M	9	β-roll	A,I,E,L,V	No (133,134,173)
F547L	9	β-roll	F,I,L,V	No (134,171,173); Increased cGMP sensitivity; misfolding (69)
G548R	9	β-roll	D,G	Expression (69)
G557R	7	β-roll	S,Q,G	No (173); Decreased cGMP sensitivity (69)
R563H	8	β-roll	H,Q,P,K,R,L,V	No (134); Increased cGMP sensitivity (172); ER retention (174)
T565M	8	β-roll	A,S,T,N,V,H,M,C,R,I	No (133,134)
R569H	7	β-roll	H,T,I,R,K,L,V	No (134,171)
Y573C	7	β-roll	F,T,N,Y,V,H,C,D	No (134)
E590K	5	β-roll	S,F,N,Y,E,V,H,Q,M,D,I,R,L	No (133);Increased cGMP sensitivity; impaired trafficking (69)
E593K	3	C-helix	A,T,N,E,V,H,Q,M,D,I,R,L	No (134)

Table 1.2. Investigation of disease-causing mutations in CNGB3. ConSurf grades were calculated using the ConSurf server (83), as described in the "Methods and Materials" section. The "Position occupancy in homologous proteins" column describes all possible amino acids featured in the corresponding positions in homologous sequences. None of the mutations has been verified experimentally.

Mutation	ConSurf grade	Location in the model-structure	Position occupancy in homologous proteins	Reference
P309L	9	S3	P	(175)
R403Q	7	P-loop	F,A,S,T,K,V,D,C,I,R,L	(133,175)
S435F	9	S6	S,A,G,V	(176)
M466T	8	Helix A'	S,A,V,M,C,I,G,L	(133)
Y469D	7	Helix A'	F,A,N,K,Y,H,Q,M,C,R,L	(133)
D494N	7	Loop B'-C'	F,Q,T,N,D,R,K,G,E	(133)
D513Y	5	Helix D'	F,S,T,N,K,Y,E,H,Q,C,D,L	(133)
F525N	8	Helix F'	F,L,V	(171)
G558C	7	cGMP binding region	A,T,I,P,G,L,V	(133)
L595F	7	cGMP binding region	F,A,S,W,N,Y,V,C,I,L	(133)

Table 3.1. The Cβ-Cβ distances between KCNE1-KCNQ1 residue pairs in the final model of the complex (presented in Å). In the case of G40 the distances were measured from the Cα. These pairs were verified against data from disulfide mapping studies, and the residues in each pair are separated by a distance of less than 15Å in the final model. The last column details the location of the interacting pairs, either in a loop, a TM segment (TM) or at the end of a TM segment (TM end).

Pair	The final model	Location
G40/T144	12.7	Loop/TM end
G40/I145	9	Loop/TM end
G40/Q147	13	Loop/Loop
K41/T144	13.9	TM end/TM end
K41/I145	9.3	TM end/TM end
K41/Q147	14.6	TM end/loop
L42/V324	7	TM end/TM end
E43/W323	5.7	TM end/TM end
A44/V141	6.2	TM/TM

Table 3.2. The Cβ-Cβ distances between KCNE1-KCNQ1 residue pairs in the final model of the complex (presented in Å). In the case of G40 the distances were measured from the Cα. These pairs were verified as not interacting by the disulfide mapping studies, and in most cases the residues in each pair are separated by a distance of more than 15Å in the final model. Still, some pairs are separated by a distances of less than 15 Å; an inspection of the model-structure of the complex revealed that only three pairs, namely L45/L142, D39/I145, A44/I145 (italicized), can be in physical contact to create an disulfide bond.

R36/S140	23.2	D39/L142	13	L45/I145	13.5
S37/S140	23.3	G40/L142	10.5	Y46/I145	15
S38/S140	20.4	K41/L142	9.4	V47/I145	13.1
D39/S140	17.6	L42/L142	12.3	R36/Q147	18.6
G40/S140	14.6	E43/L142	11.1	S37/Q147	20.5
K41/S140	13.9	*L45/L142*	10.1	S38/Q147	18.1
L42/S140	16.1	Y46/L142	12.3	D39/Q147	14.9
E43/S140	14.2	V47/L142	10	A44/Q147	15.9
A44/S140	10.8	R36/T144	20.1	L45/Q147	19.4
L45/S140	12.8	S37/T144	21	Y46/Q147	20.8
Y46/S140	14.1	S38/T144	18.2	V47/Q147	19
V47/S140	10.8	D39/T144	15.2	R36/Y148	21.3
R36/V141	19.5	L42/T144	16	S37/Y148	23.1
S37/V141	19.5	E43/T144	14	S38/Y148	20.5
S38/V141	16.7	A44/T144	11.3	D39/Y148	17.1
D39/V141	14.2	L45/T144	14.5	G40/Y148	16.6
G40/V141	10.9	Y46/T144	15.7	K41/Y148	17.5
K41/V141	10.5	V47/T144	13	L42/Y148	21.2
L42/V141	12.7	R36/I145	17.1	E43/Y148	20.4
E43/V141	10.5	S37/I145	18.1	A44/Y148	18.5
L45/V141	9.9	S38/I145	15.2	L45/Y148	21.7
Y46/V141	10.9	*D39/I145*	11.9	Y46/Y148	23.6
R36/L142	19.4	L42/I145	13.8	V47/Y148	21.9
S37/L142	19.3	E43/I145	12.3		
S38/L142	16.1	*A44/I145*	*10*		

Table 4.1. Matching GNM modes of the Kv7.1 channel with the corresponding modes of Kv1.2 (103) that share similar hinges. The first column shows hinges in Kv7.1, and the second column shows hinges in the Kv1.2 channel (103). The third column shows the Kv7.1 positions corresponding to the Kv1.2 hinges of the second column; if the hinges are the same in Kv7.1 and Kv1.2, the same position appears in columns 1 and 3. The last column describes the involvement of each Kv7.1 hinge (first column) in diseases. LQTS1 - long QT syndrome 1; JLNS - Jervell and Lange-Nielsen syndrome; AF - atrial fibrillation.

Kv7.1 GNM1,2+3	Kv1.2 GNM3	Corresponding position in Kv7.1	Disease association
Q147	C181	V141	
A208	V261	I204	R192P is involved in LQTS1(177)
I235	R297	R231	I235N is involved in LQTS1(178,179)
Q260-262	M325-L328	R259-L262	E261D is involved in JLNS(179); E261K(180), L262V(177) are involved in LQTS1
T312-G316	T373-D379	T311-D317	T312I(179), I313M(181), G314S(182)/C(183)/D(179)/A(184), Y315S(180)/C(179), G316R(179) are involved in LQTS1
F340-A346	I402-V410	F340-G348	A341E(185)/V(179), L342F(180,182), P343S(177), A344E/V(179), G345E(179)/R(186) are involved in LQTS1

Kv7.1 GNM4	Kv1.2 GNM4	Corresponding position in Kv7.1	Disease association
L137	V178	I138	L137P is involved in LQTS1
A152-T153	F223	F157	
F232-M238	P265	A208	I235N is involved in LQTS1(180,182)
I282	V301	I235	
Y299	L341-F348	F275-I282	
W323-G325	V390	I328	G325R is involved in LQTS1(181)

Kv7.1 GNM5,6+7	Kv1.2 GNM5	Corresponding position in Kv7.1	Disease association
V129	L182	L142	
F167-G168	T216	-	G168R is involved in LQTS1(179)
I204-V206	I254-T269	P197-V212	I204M(177)/F(179) is involved in LQTS1
R249-V262	L321	V255	L250H(187), L251P(188), V254M(179) E261K(180), L262V(177) are involved in LQTS1; E261D is involved in JLNS(179)
I313-G316	T373-G376	T311-G314	I313M(181), G314S(182)/C(183)/D(179)/A(184), Y315S(180)/C(179), G316R(179) are involved in LQTS1
G345	A403	A341	G345E(179)/R(186) is involved in LQTS1

Table 4.2. Matching the slowest GNM and ANM modes of the Kv7.1 channel alone and in association with KCNE1. Degenerate modes are separated by commas.

Motion type	Kv7.1		Kv7.1 + KCNE1	
	GNM	ANM	GNM	ANM
I	1,2+3	4	1,2+3	1
II	4	1+2,3	4	3,4
III	5,6+7	6,7+8	5,6+8	5
IV	8	5	7	2

Figures

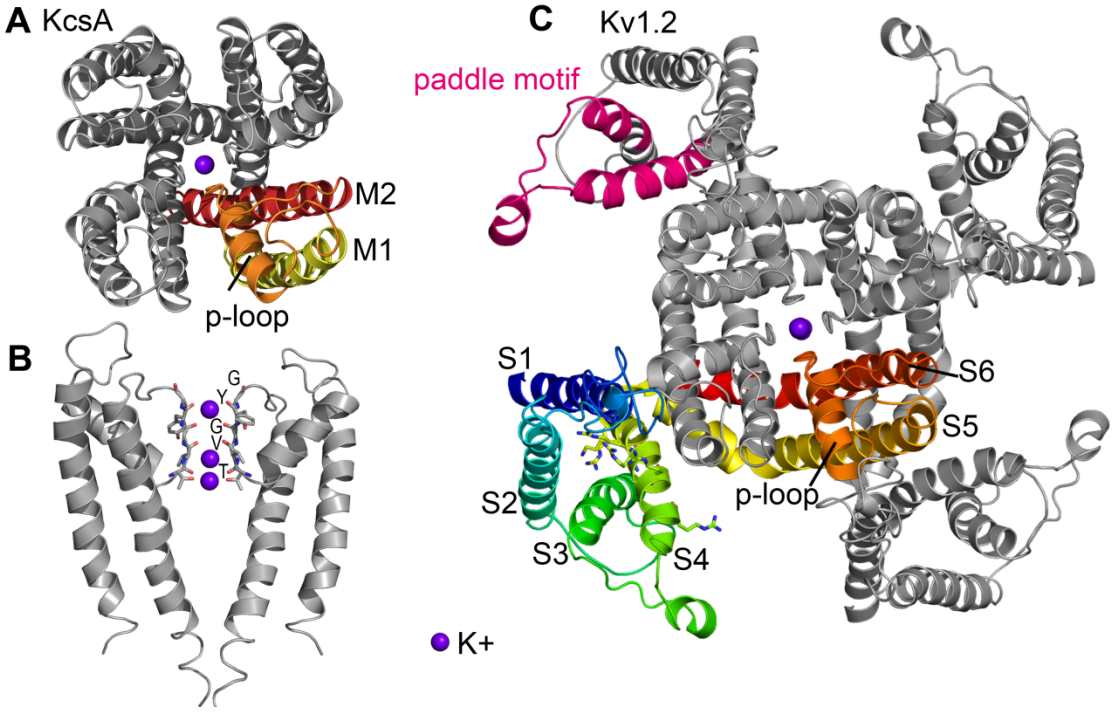

Figure 1.1. Tetrameric potassium channels: (A, B) KcsA (PDB entry 1K4C, (13)) and (C) refined Kv1.2 structure (PDB entry 3LUT, (8)). Potassium ions are shown as purple. (A, B) The prokaryotic channel KcsA represents the simplest VGL channel with only two TM helices, named M1 and M2. (A) An extracellular view of the KcsA tetramer. One of the subunits is presented in rainbow scheme to show the structural elements, and the rest are in grey. (B) Side view of the channel, showing only two juxtaposed subunits. The conserved residues of the selectivity filter, i.e., TVGYG, are shown in sticks representation. (C) An extracellular view of the Kv1.2 tetramer. One of the subunits is presented in rainbow scheme to show the structural elements, and the rest are in grey; on the adjacent subunit the paddle motif, i.e., the C-terminus of S3 helix and the S4 helix, is colored pink. The conserved positively charged residues on S4 are shown in stick representation. Many VGL channel share a similar fold with six TM helices.

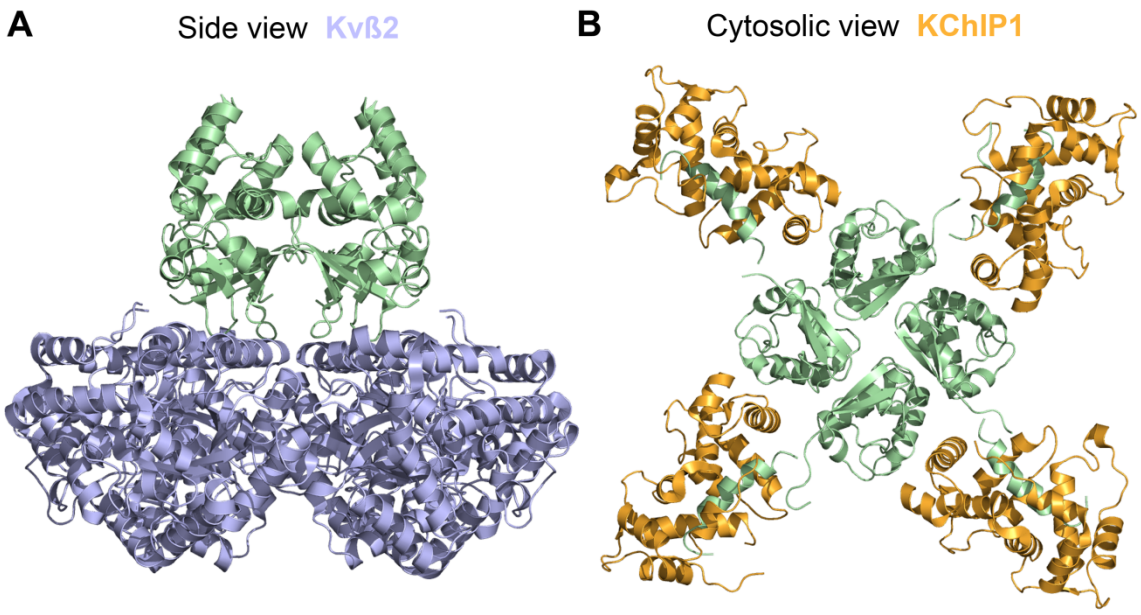

Figure 1.2. Diversity in the auxiliary subunits of the voltage-gated potassium channels. (A) A side view of the crystal structure of the Kvβ2 subunit (blue) interacting with the cytosolic domain (green) of Kv1.2 (PDB entry 2A79, (7)). (B) A cytosolic view of the crystal structure of the KChIP1 subunit (orange) interacting with the cytosolic domain (green) of the Kv4.3 channel (PDB entry 2I2R, (14)). It is evident that KChIP1 subunits interact with the cytosolic domain of the voltage-gated channel as monomers, whereas Kvβ2 subunits interact with the cytosolic domain as a tetramer.

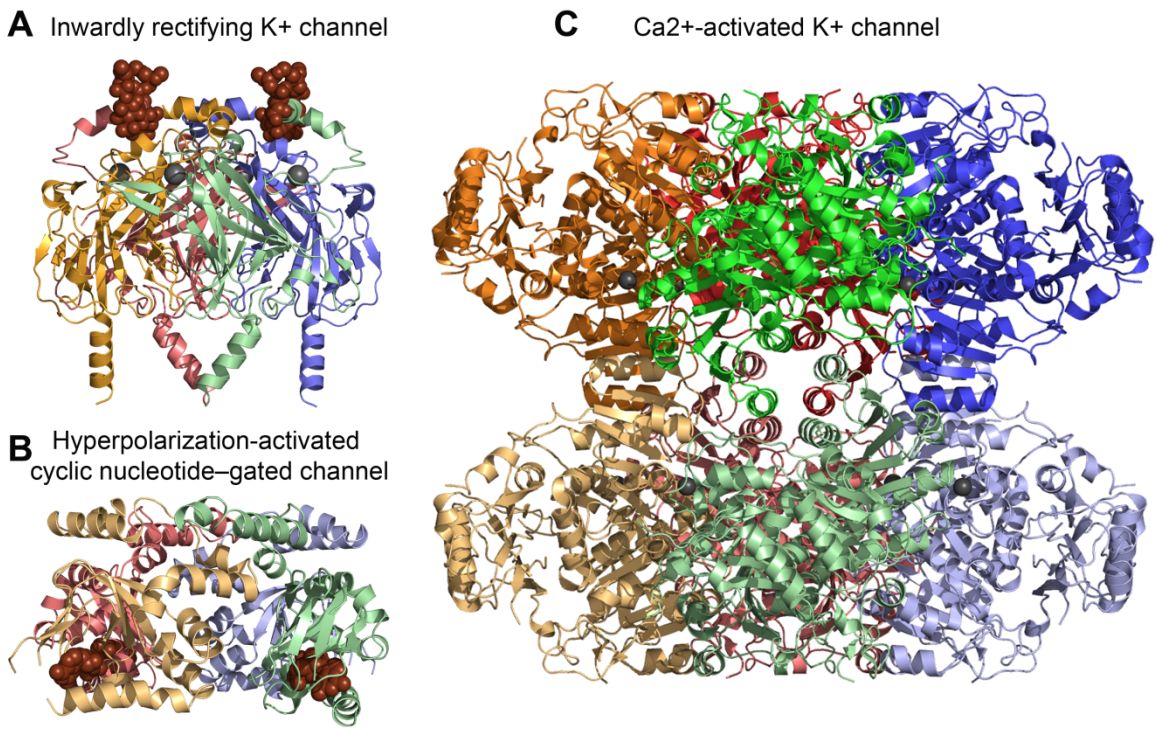

Figure 1.3. Diversity of the cytoplasmic regulatory domains in the VGL superfamily. (A) The cytosolic tetrameric domain of the inwardly rectifying potassium channel Kir3.2 (PDB entry 3SYA, (189)). The domain is presented in side view and colored according to monomers. The channel can be modulated by Na^+ ions and PIP2 molecules, both interacting with the cytosolic domain. Na^+ ions and PIP2 molecules are presented as space-filled atoms colored grey and brown, respectively. (B) The cytosolic tetrameric domain of hyperpolarization-activated cyclic nucleotide–gated channel HCN2 (PDB entry 1Q3E, (46)). The domain is presented in side view and colored according to monomers. The cyclic nucleotide is shown as brown space-filled atoms. (C) The cytosolic octameric domain of the calcium-activated potassium channel BK1 (PDB entry 3U6N, (190)). The domain is presented in side view and each subunit is colored separately. Ca^{2+} ions are shown as grey space-filled atoms. It is evident that the regulatory cytosolic domains differ from each other significantly in their structure, size, number of subunits and the modulatory ligands.

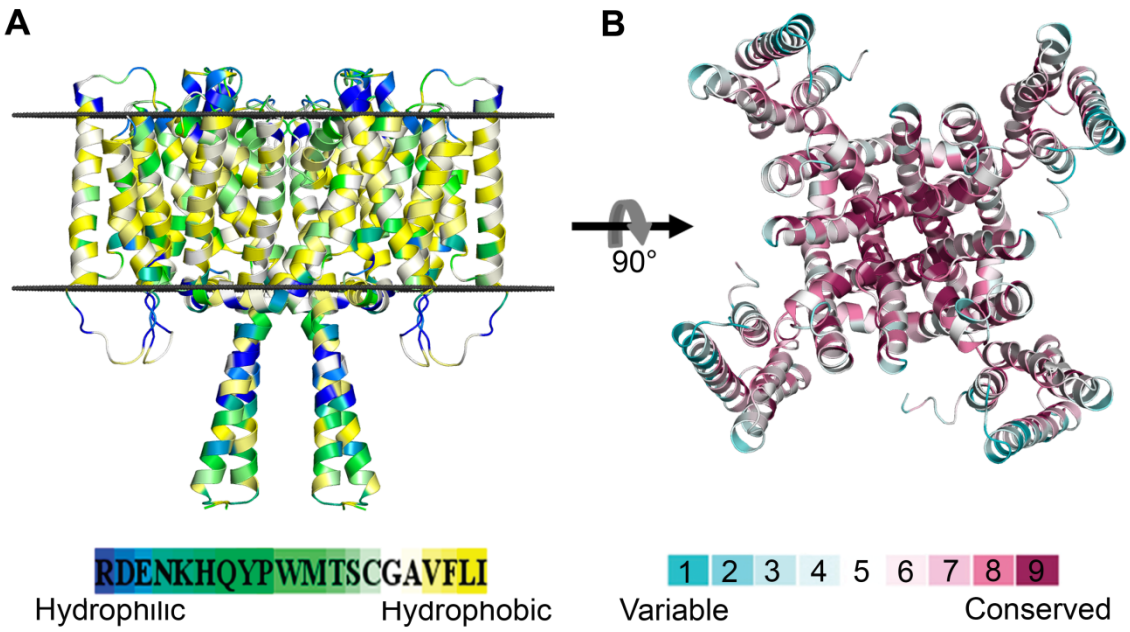

Figure 1.4. The hydrophobicity profile and the evolutionary conservation profile are general characteristics of TM structures. Here both profiles are demonstrated on the bacterial MlotiK1 channel (PDB entry 3BEH, (51)). (A) The channel is colored according to the color-coding bar, with hydrophilic-through-hydrophobic residues corresponding to blue-through-yellow (side view). The approximate boundaries of the hydrocarbon region of the membrane, as predicted by the OPM database (191), are shown in grey. The structure displays a typical hydrophobicity pattern, with hydrophobic residues exposed to the lipid, and charged and polar amino acids buried in the protein core or located in the loop regions. (B) The channel is colored by conservation grades according to the color-coding bar, with variable-through-conserved corresponding to turquoise-through-maroon (extracellular view). The structure displays the typical conservation pattern, where the variable residues are peripheral, and the conserved residues are in the channel core.

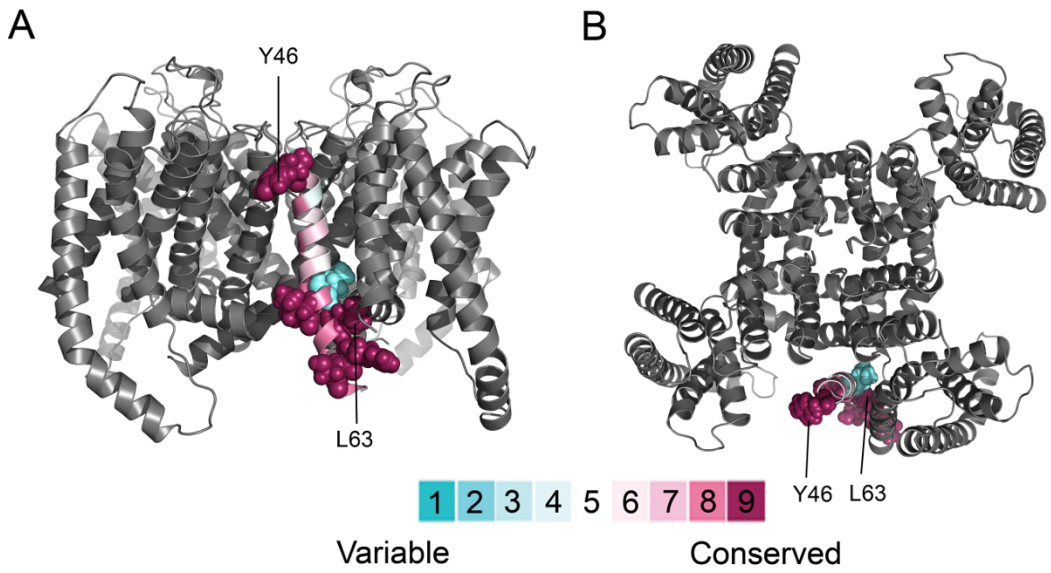

Figure 1.5. Extracellular (A) and side (B) views of the evolutionary conservation profile of KCNE1 in complex with the Kv7.1 channel according to the Kang et al. model (41). The channel tetramer is in grey, and the KCNE1 model is colored by conservation grades according to the color-coding bar, with variable-through-conserved corresponding to turquoise-through-maroon. The most variable residues (score 2 – none of the residues in this region was assigned a score of 1), namely L59, and the most conserved residues (score 9), namely Y46, I61, L63, R67 and S68, are displayed as space-filled atoms. It is evident that variable residues of KCNE1 are located at the interaction interface with the channel, a conformation that is in conflict with the typical conservation pattern. KCNE1 residues Y46 and L63, mutations in which are described here, are labeled.

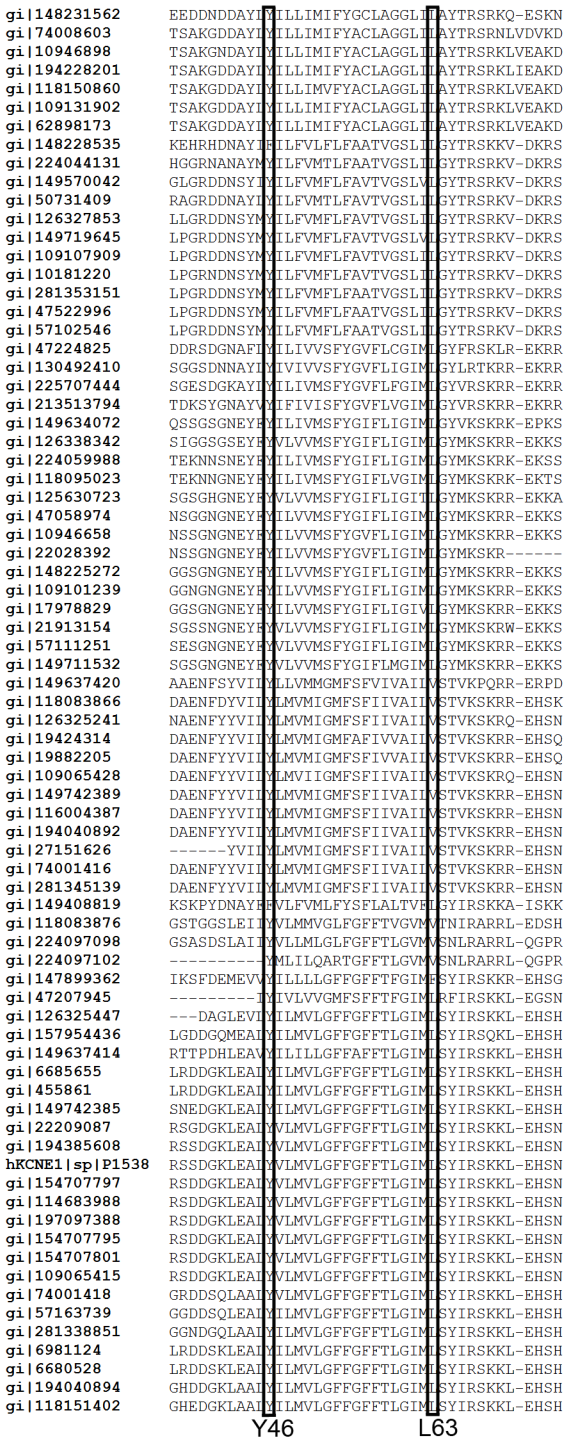

Figure 3.1. The multiple sequence alignment of KCNE1 homologs used to calculate the conservation profile of KCNE1. The homologs were collected from the NR database (84) using PSI-BLAST (85). Redundant sequences (>99% sequence identity) were discarded, and the resultant 76 sequences, all from the KCNE family, were aligned using MUSCLE (86). Only the

modeled segment of KCNE1, i.e., residues 36-75, and the corresponding sequences of the homologous proteins are shown. Positions Y46 and L63, which were mutated, are highlighted.

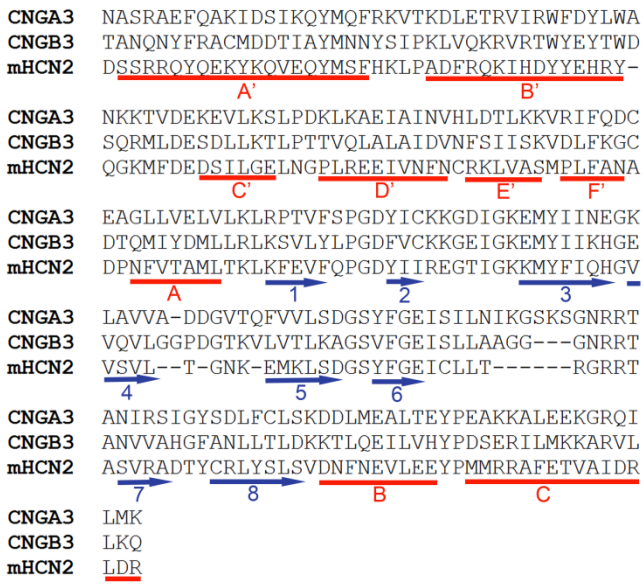

Figure 3.2. Sequence alignment of mouse HCN2, CNGA3 and CNGB3 channels in the CNBD region. The structural elements, α-helices (red lines) and β-sheets (blue arrows), are marked. The α-helices are labeled with capital letters and the β-sheets with regular numbers (59).

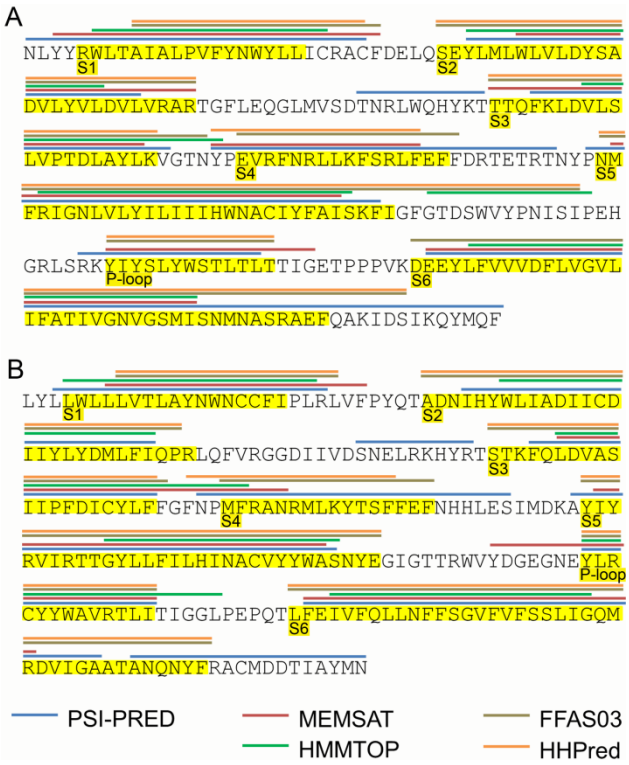

Figure 3.3. Building the model structures of human CNGA3 (A) and CNGB3 (B). The location of the TM helices according to secondary-structure prediction (PsiPred (94)), TM segment identification (MEMSAT (95) and HMMTOP (96)), profile-to-profile alignment (HHpred (98)) and fold recognition (FFAS03 (97)) are marked in different colors according to the legend. The boundaries of the TM helices that were used for the modeling are highlighted in yellow; the TM helices are also marked and highlighted in yellow.

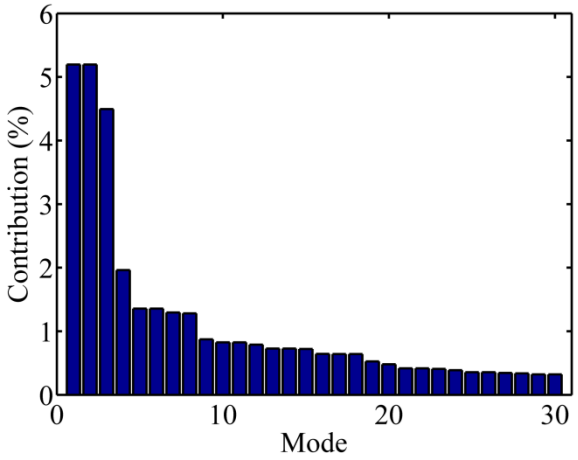

Figure 3.4. The contribution of the 30 slowest GNM modes to the overall motion of the Kv7.1 tetramer. The percentage of contribution was estimated as the weight of the frequency of a specific mode *n*, calculated considering the frequencies of all N modes ($100\lambda_n/\lambda_{N-1}$). Modes 1 and 2 share the same eigenvalue, as do modes 5 and 6. I studied the 8 slowest modes, each of which contributes over 1%.

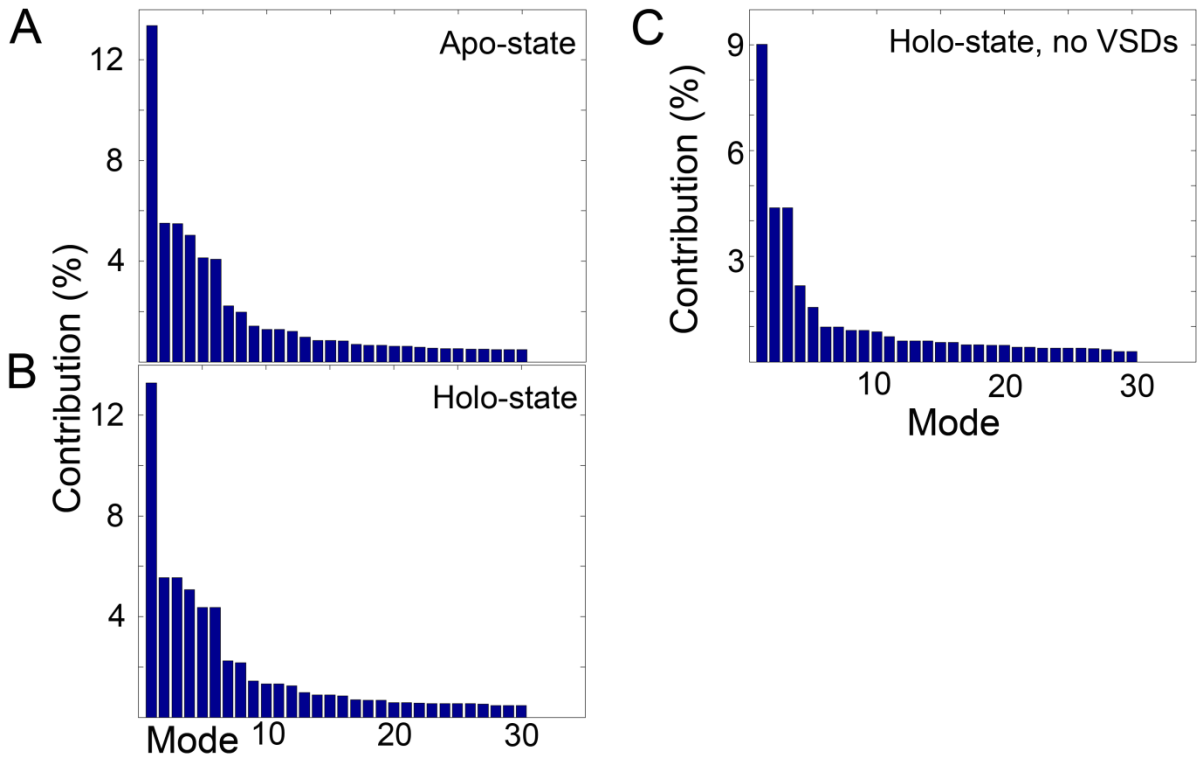

Figure 3.5. The contribution of the 30 slowest GNM modes to the overall motion of the CNGA3 tetramer in apo (A) and holo (B) states, and in holo-state lacking the VSDs (C). The percentage of contribution was estimated as the weight of the frequency of a specific mode *n*, calculated considering the frequencies of all N modes ($100\lambda_n/\lambda_{N-1}$). (A, B) Modes 2 and 3 share the same eigenvalue, as do modes 5 and 6. I studied here the 6 slowest modes, each contributing over 4%. (C) Modes 2 and 3 share the same eigenvalue. I investigated the three slowest modes of the CNGA3 tetramer lacking the VSDs, each contributing over 3%.

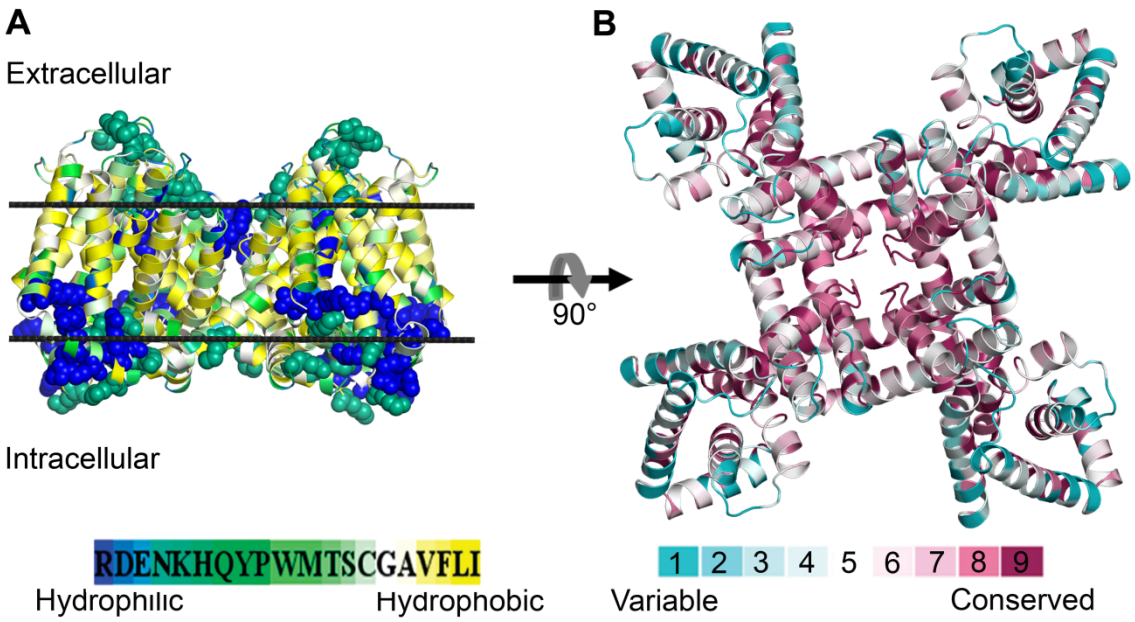

Figure 4.1. (A) The hydrophobicity profile of the model-structure of the TM region of Kv7.2. The channel is colored according to the color-coding bar, with hydrophilic-through-hydrophobic residues corresponding to blue-through-yellow (a side view). The approximate boundaries of the hydrocarbon region of the membrane, as predicted by the OPM database (191), are shown in grey. The structure displays a typical hydrophobicity pattern, with hydrophobic residues exposed to the lipid, and charged and polar amino acids buried in the protein core or located in the loop regions. The positively charged residues, lysine and arginine, in the extracellular and the intracellular sides of the membrane are shown as space-filled atoms. Reassuringly, the abundance of the predicted location of such residues in the cytoplasmic end of the protein is in accordance with the 'positive-inside' rule (115). (B) The Kv7.2 channel is colored by conservation grades according to the color-coding bar, with variable-through-conserved corresponding to turquoise-through-maroon (an extracellular view). The model-structure displays the typical conservation pattern, where the variable residues are peripheral, and the conserved residues are in the channel core.

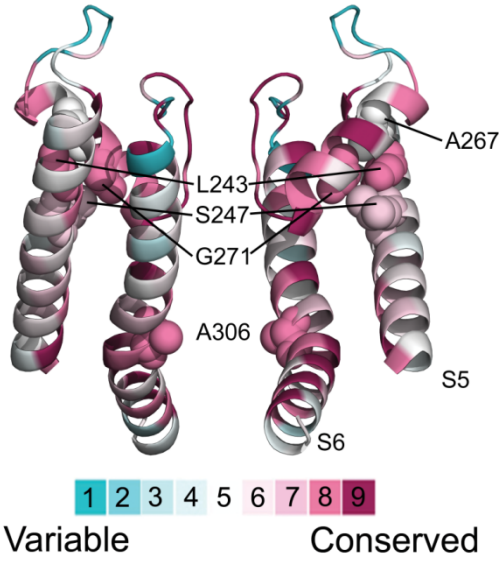

Figure 4.2. The location of disease-causing mutations in the Kv72 TM region. For clarity, only the S5 and S6 helices of two juxtaposed monomers (of the tetrameric channel) are shown in ribbons representation with the cytoplasmic region facing down. The evolutionary conservation is color-coded using the bar. The amino acids, mutations in which are disease-causing, are shown as space-filled atoms. Evidently, L243, S247, A267, G271 are positioned in the tight interface between S5 and the pore helix, while A306 faces the pore.

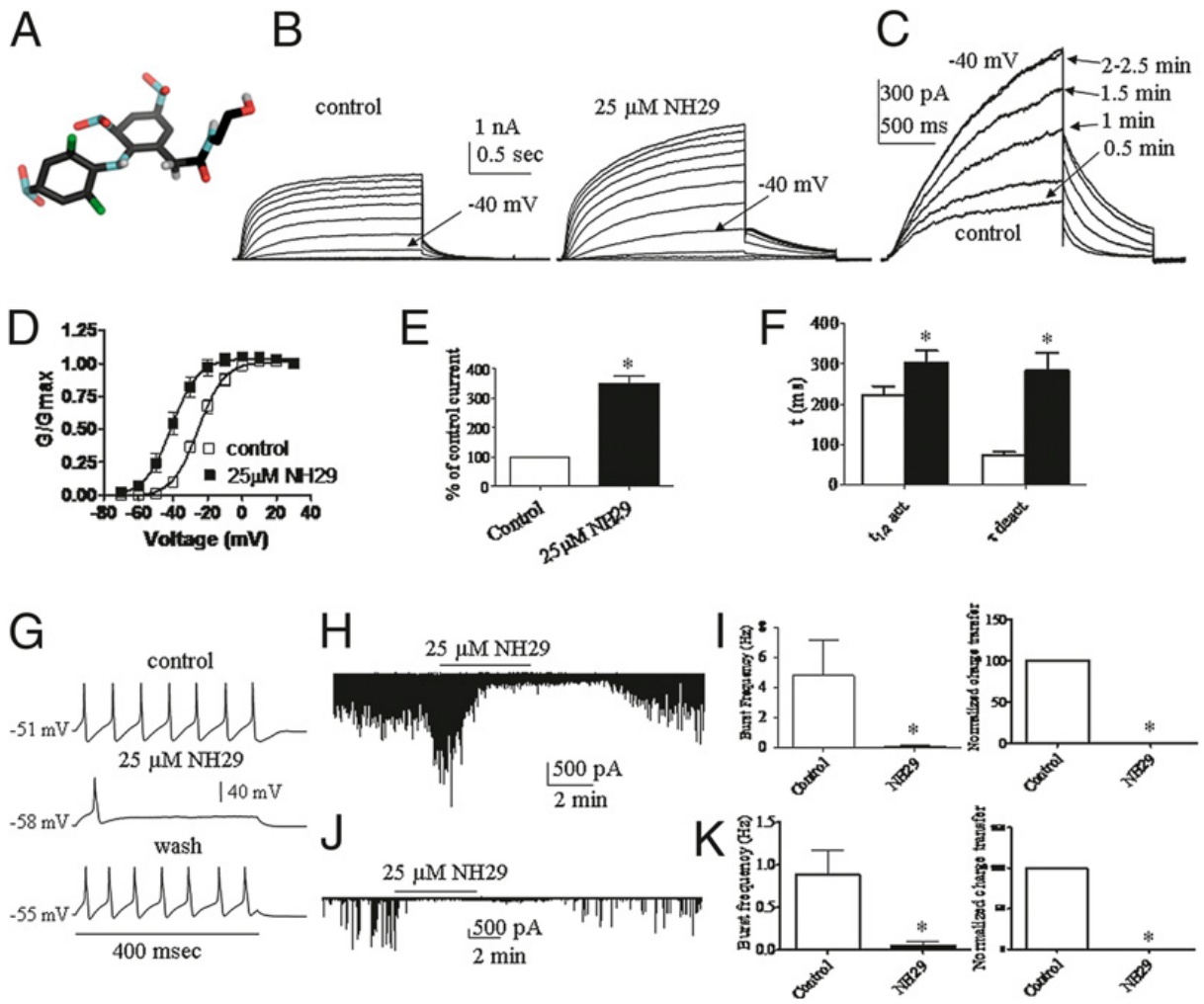

Figure 4.3. NH29 increases Kv7.2 currents and inhibits neuronal spike discharge and neurotransmitter release. (A) Chemical structure of NH29. (B) Representative Kv7.2 whole-cell currents, in transfected Chinese hamster ovary cells, in the absence and presence of 25µM NH29. Cells, held at -90 mV, were stepped from -70 mV to +30 mV in 10 mV increments and repolarized at -60 mV. (C) Representative trace of a cell, stepped at -40 mV every 30 s in the absence (control) and presence of 25µM NH29. (D) The normalized conductance was plotted as a function of the test voltages, for cells in the absence (empty squares) and presence (solid squares) of 25µM NH29 (n = 15, *p < 0.01). (E) Potentiation of *wt* Kv7.2 currents recorded at -40 mV in the presence of NH29 expressed as percentage of control in the absence of opener (n = 15, *p < 0.01). (F) Kinetics of Kv7.2 were measured in the absence (empty bars) and presence of 25 µM

NH29 (solid bars) ($n = 15$, $^*p < 0.01$). Activation kinetics was evaluated at -40 mV by $t_{1/2}$, the time at which half of the current amplitude developed. Deactivation kinetics was measured at -60 mV and fitted by one exponential function. (G) Representative rat dorsal root ganglion spiking discharge, evoked by a squared depolarizing current pulse (100 pA for 400 msec) before (control), during exposure to 25 μM NH29 and after washout (wash). Representative traces of spontaneous EPSCs (H) and IPSCs (J) recorded before, during exposure to 25 μM NH29 and after washout. Effects of NH29 on burst frequency and charge transfer of spontaneous EPSCs (I) and IPSCs (K) ($n = 4$; $^*p < 0.05$). The experiments were performed by the lab of Prof. Attali.

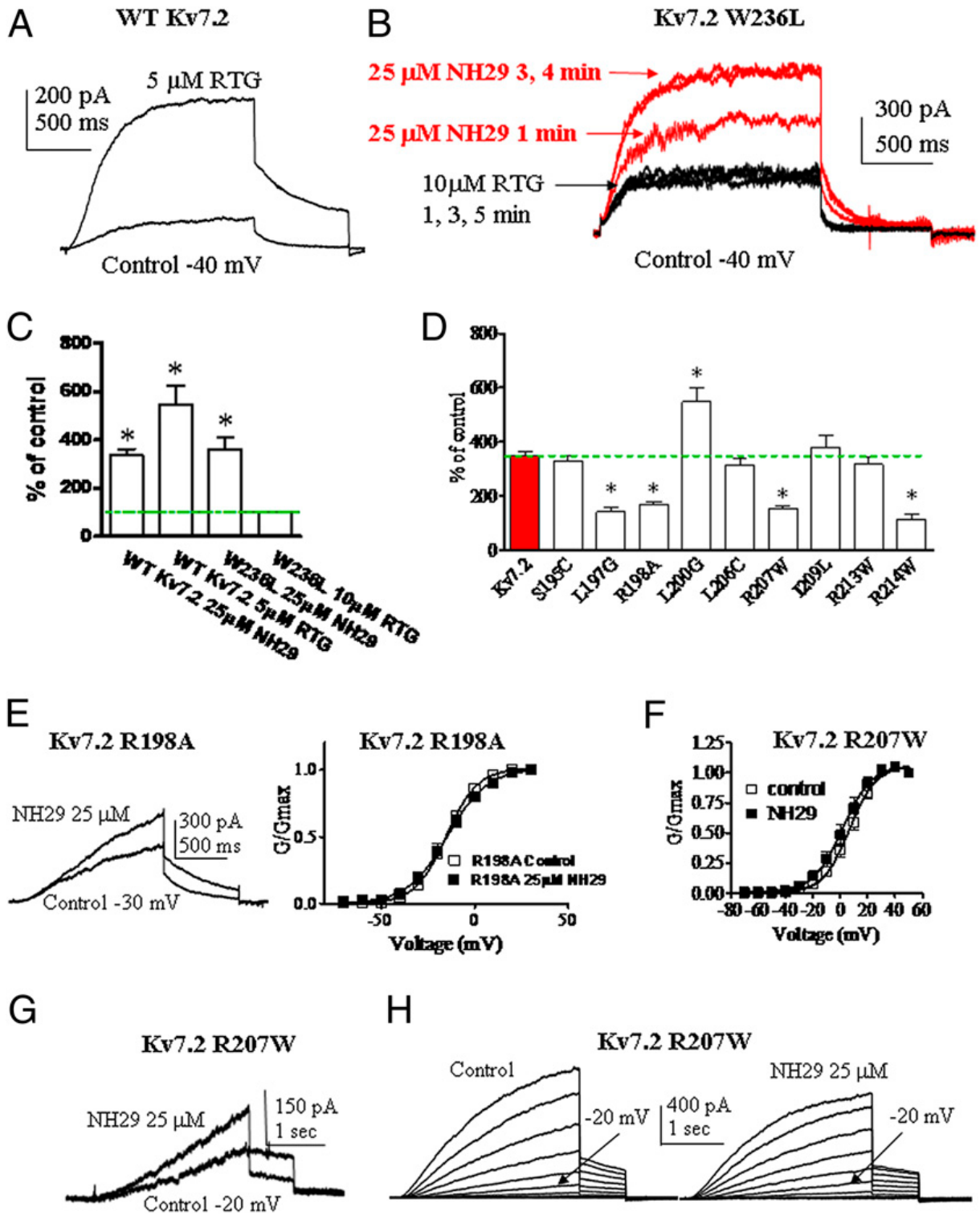

Figure 4.4. Sensitivity of pore and S4 residues to NH29 modulation. (A) Representative trace of a cell expressing *wt* Kv7.2, stepped at -40 mV in the absence (control) and presence of 5µM retigabine. (B) Representative trace of a cell expressing mutant Kv7.2 W236L, stepped at -40 mV

in the absence (control) and presence of 10 μM retigabine and subsequently exposed to 25 μM NH29. (C) Potentiation of *wt* Kv7.2 and mutant W236L currents recorded at -40 mV in the presence of NH29 or retigabine expressed as percentage of control (n = 5-8, *p < 0.01). (D) Potentiation of the current produced by 25 μM NH29 on *wt* Kv7.2 (red bar) and the different S4 mutants, expressed as % of control determined in the absence of the opener (n = 6-15, *p < 0.01). (E) Representative trace of a cell expressing mutant Kv7.2 R198A, stepped at -20 mV in the absence (control) and presence of 25 μM NH29 (left) and normalized conductance (right) in the absence (empty squares) and presence (solid squares) of 25μM NH29 (n = 8). (F) Normalized conductance of mutant Kv7.2 R207W in the absence (empty squares) and presence (solid squares) of 25μM NH29 (n = 8). (G) Representative trace of a cell expressing mutant Kv7.2 R207W, stepped at -20 mV in the absence (control) and presence of 25 μM NH29. (H) Representative Kv7.2 R207W currents recorded as in Figure 4.3B, in the absence and presence of 25μM NH29. The experiments were performed by the lab of Prof. Attali

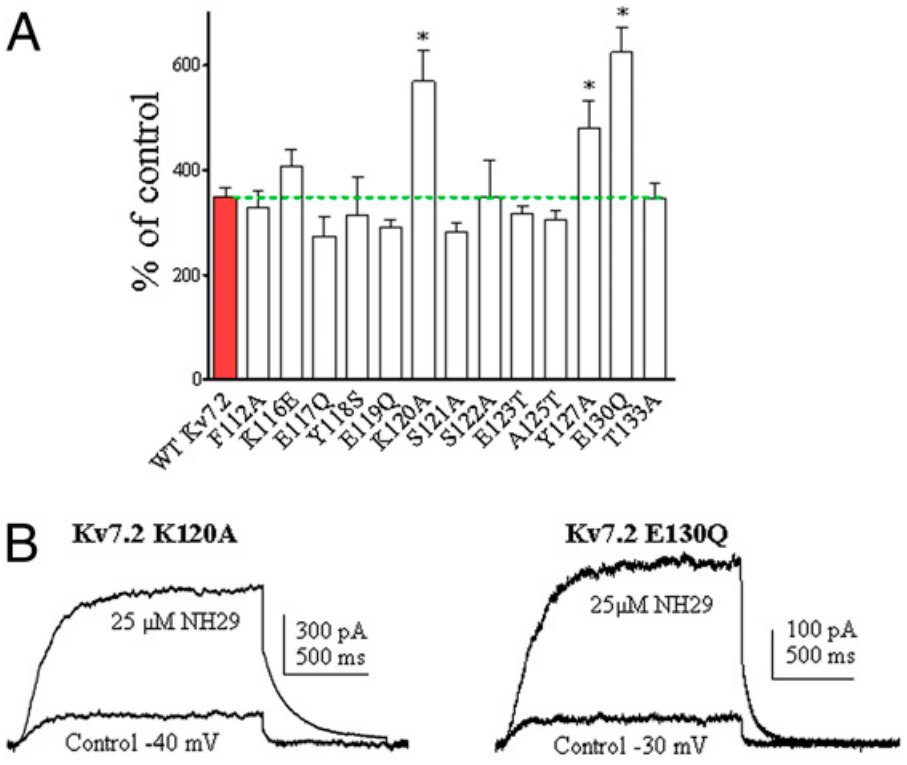

Figure 4.5. Sensitivity of S2 and S1-S2 linker residues to NH29 modulation. (A) Potentiation of the currents produced by 25 µM NH29 on *wt* Kv7.2 (red bar) and the different S1-S2 linker and S2 mutants, expressed as % of control determined in the absence of the opener (n = 4-15, *p < 0.01). (B) Representative trace of cells expressing mutant Kv7.2 K120A (left) or mutant Kv7.2 E130Q (right) in the absence (control) and presence of 25 µM NH29. The experiments were performed by the lab of Prof. Attali

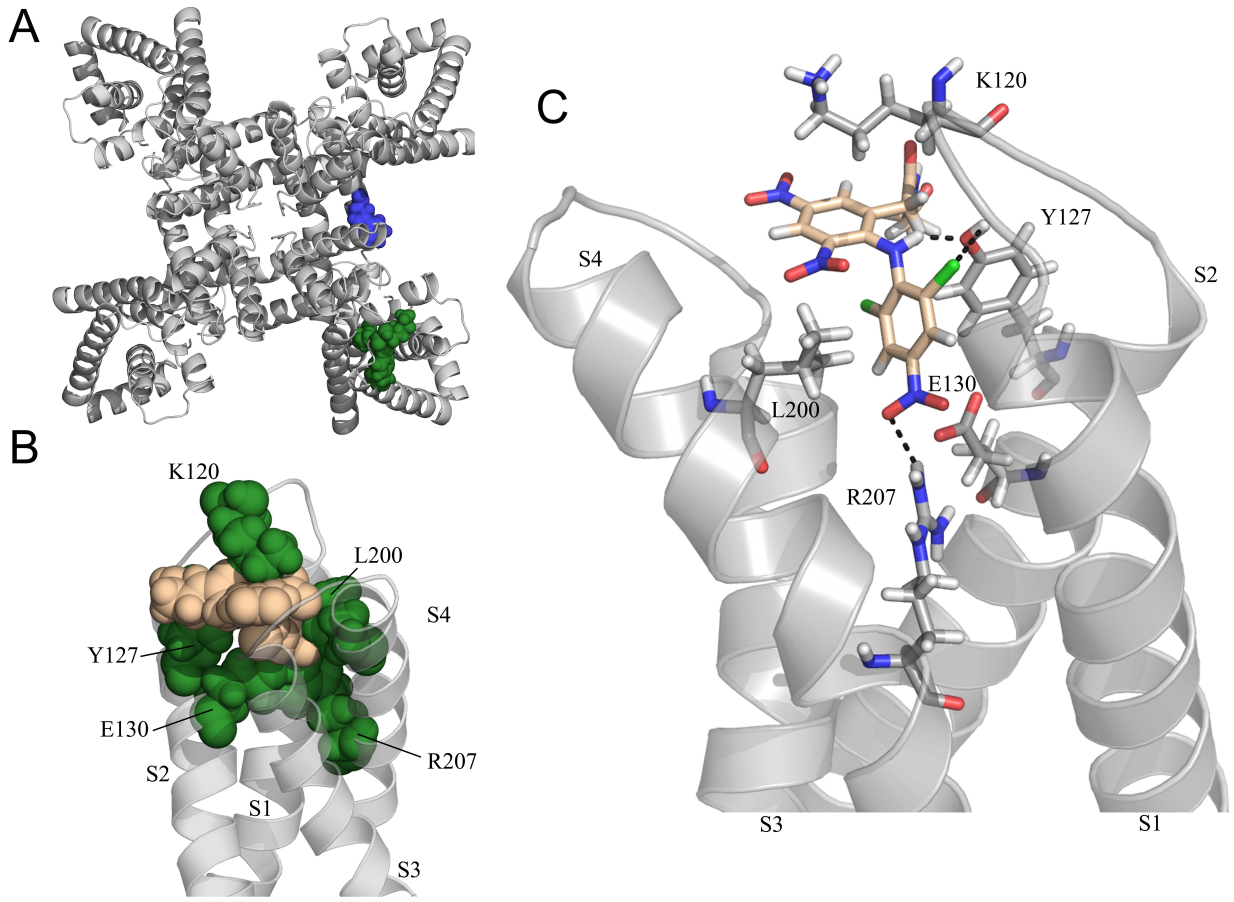

Figure 4.6. Docking of NH29 onto the model-structure of Kv7.2 in an open state. (A) Top view of the model-structure showing on one subunit the S5 residue W236 (blue) involved in retigabine interaction and on another subunit the VSD residues (green) (K120, Y127A, E130, L200 and R207) forming the binding pocket of NH29. (B) Front view of one VSD showing the bulky residues (green filled spheres) sandwiching one NH29 molecule (salmon filled spheres). (C) Side view of VSD residues (sticks) engaged in hydrogen bonding with one NH29 molecule (stick).

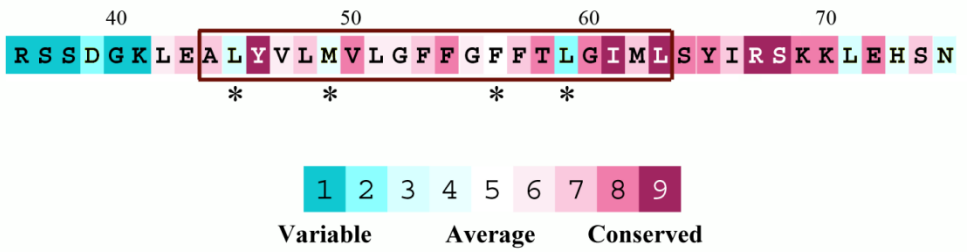

Figure 4.7. Mapping of the ConSurf conservation grades of Figures 4.8 and 1.5 on the KCNE1 sequence. Conservation is shown using the color-coding bar, i.e. the highly variable and highly conserved residues are shown in turquoise and maroon, respectively. The brown rectangle represents the location of the TM helical segment in the model-structure. The residues marked by asterisks are more variable than the rest. All these residues face the lipids in my model-structure of the Kv7.1-KCNE1 complex, but three of them, namely L45, F56 and L59, are in direct contact with Kv7.1 in the Kang et al. model (41).

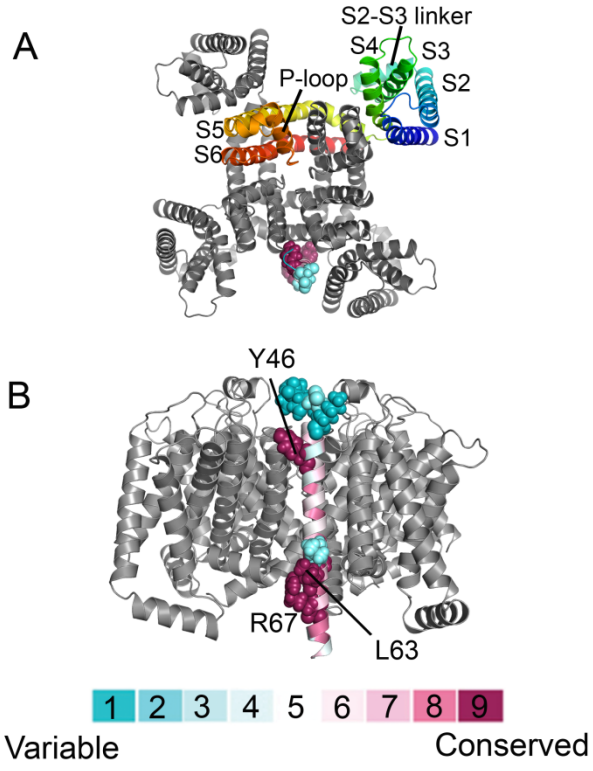

Figure 4.8. The evolutionary conservation of KCNE1 within the complex with Kv7.1. In the proposed model, the evolutionarily-conserved face of KCNE1 is in contact with the channel, and the variable face points to the lipid bilayer, as it should. The channel tetramer is in grey, and the KCNE1 model is colored by conservation grades according to the color-coding bar, with variable-through-conserved corresponding to turquoise-through-maroon. The most variable residues (scores 1 and 2), namely R36, S37, S38, D39, G40, K41 and L59, and the most conserved residues (score 9), namely Y46, I61, L63, R67 and S68, are displayed as space-filled atoms. (A) Extracellular view. One of the subunits of the homotetrameric channel is presented in rainbow scheme to show the structural elements, and the rest of the subunits are in grey. (B) Side view. KCNE1 residues Y46, L63 and R67 are marked.

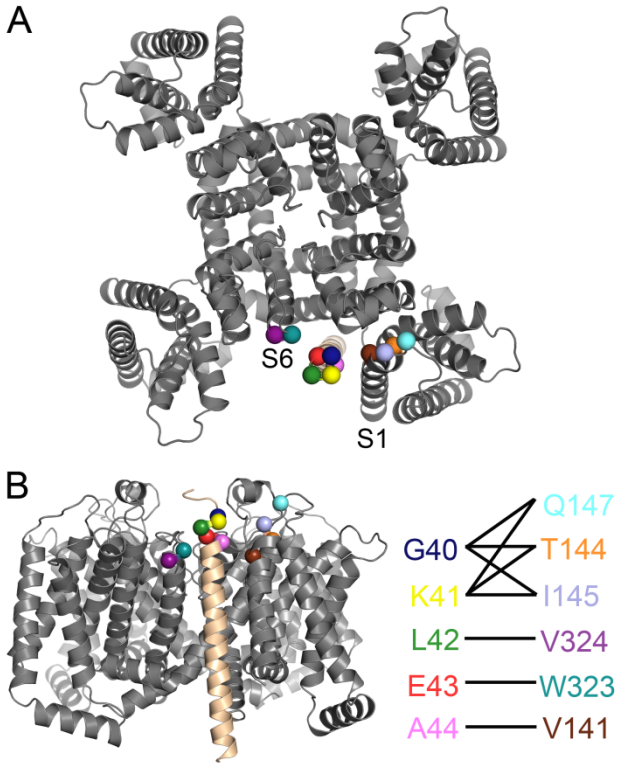

Figure 4.9. The model-structure of the Kv7.1-KCNE1 complex correlates well with disulfide-link experiments. Extracellular (A) and side (B) views of the model using ribbon representation. KCNE1 appears in light orange and the channel tetramer in grey. The α-carbons of residues that formed disulfide bonds upon Cys mutation of G40, K41, L42, E43 and A44 in KCNE1 and of V141, T144, I145, Q147, W323 and V324 in the channel are shown as space-filled atoms and colored according to the scheme. The distances between the residue pairs shown here are listed in Table 3.1. The pairs reported to form S-S bonds when mutated to Cys are connected by solid black lines (89-91). In (A) residues 36–39 of KCNE1 are omitted for clarity.

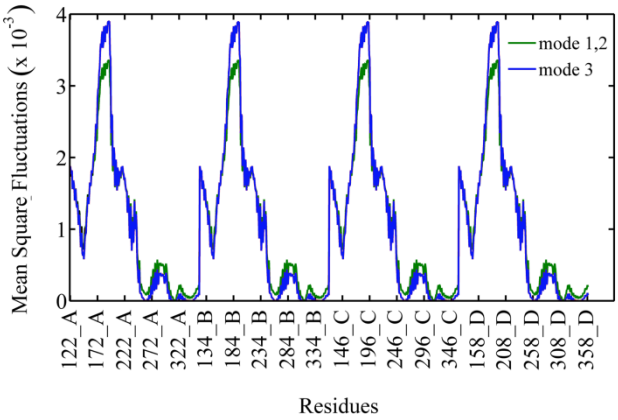

Figure 4.10. Mean-square fluctuations of the Kv7.1 tetramer in the three slowest GNM modes. The shape of the third mode (blue) fits the profile of the average of modes 1 and 2 (green).

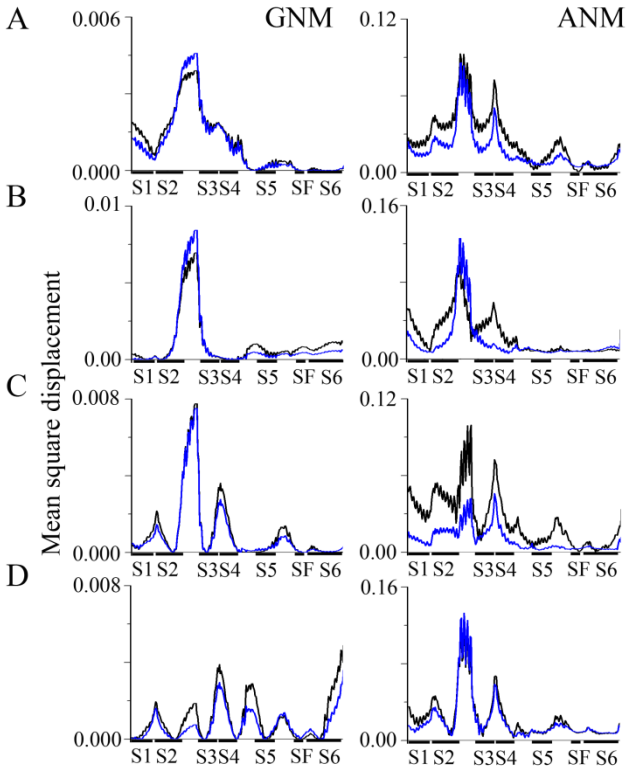

Figure 4.11. Mean-square displacement of the Kv7.1 channel alone (black curves) and in complex with four KCNE1 subunits (blue curves) according to the GNM and ANM modes. The modes of motion are grouped as described in Table 4.2: (A) Motion I; (B) Motion II; (C) Motion III; (D) Motion IV. The locations of the TM helices and the selectivity filter (SF) are marked on the x-axis. The fluctuations of one chain of the homotetrameric channel are presented, since the fluctuations of all four Kv7.1 chains are identical. The overall shape of the fluctuations is mostly preserved upon KCNE1 binding in both elastic models.

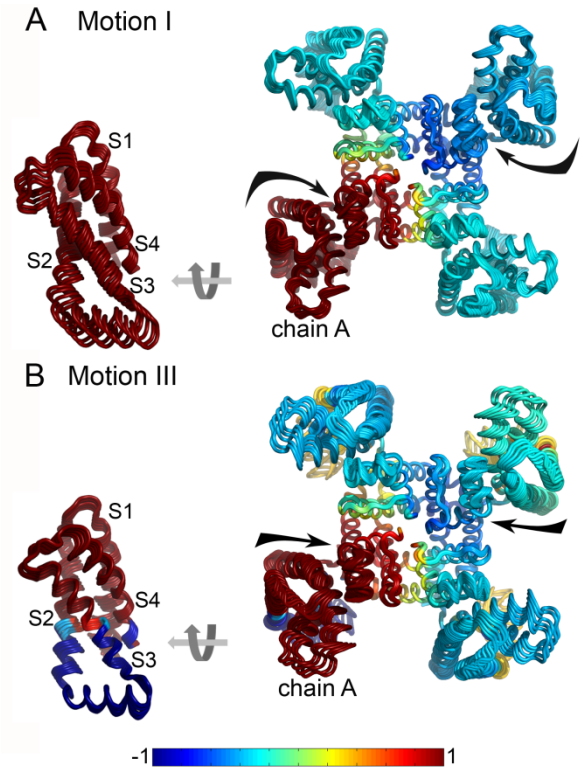

Figure 4.12. Mapping the cooperative dynamics of the Kv7.1 channel on the conformations predicted by ANM. The channel is shown in cartoon representation and colored according to the correlation of the chain A paddle with the other residues in the corresponding GNM mode (Table 4.2): (A) Motion I – conformations of ANM mode 4, colored according to the corresponding GNM modes 1-3. (B) Motion III – conformations of ANM mode 8, colored according to the corresponding GNM modes 5-7. The magnitude of positive and negative correlations between the fluctuations of the residues is color-coded according to the blue-to-red scale at the bottom of the picture. Positive correlation indicates motion of two residues in the same direction, while negative correlation specifies motion in opposite directions. The direction of motion, detected by the ANM analysis, is marked with black arrows. For clarity, the VSDs of chain A are shown in side view as well. It is apparent that in motion I each VSD domain moves, in essence, as one unit. In motion III, the S1, the N-terminus of S2, and the paddle motif (C-terminus of S3 and S4

segments) are negatively correlated with the C-terminus of S2, the S2-S3 linker and the N-terminus of S3.

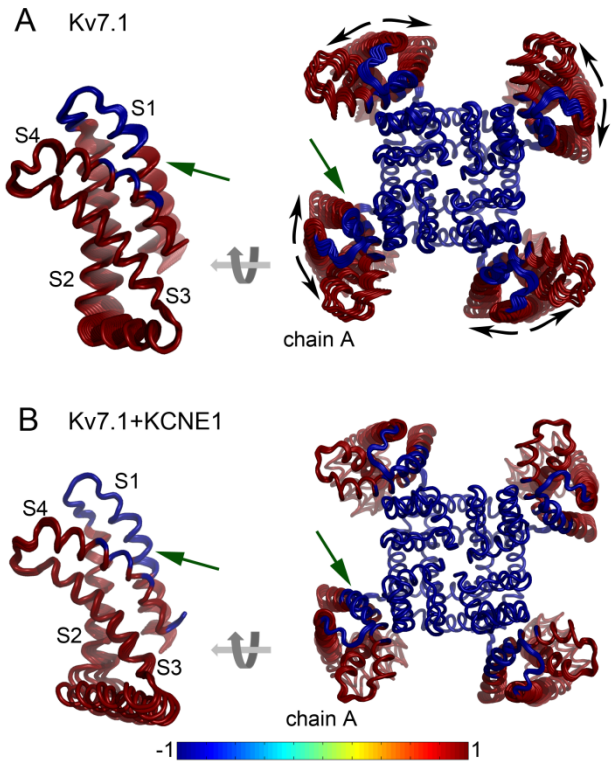

Figure 4.13. KCNE1 association affects the cooperative dynamics of motion II of the isolated Kv7.1 channel. The conformations are colored according to the correlation of the chain A paddle with the other residues in the corresponding GNM mode (Table 4.2), using the blue-to-red scale at the bottom. (A) Channel conformations from ANM mode 1, colored according to the corresponding GNM mode 4. The direction of motion, detected by the ANM analysis, is marked with black arrows. (B) Averaged conformations of the channel in complex with KCNE1 from ANM modes 3 and 4, colored according to the corresponding GNM mode 4. KCNE1 association affects the cross-correlations of the S1 C-terminus (green arrows).

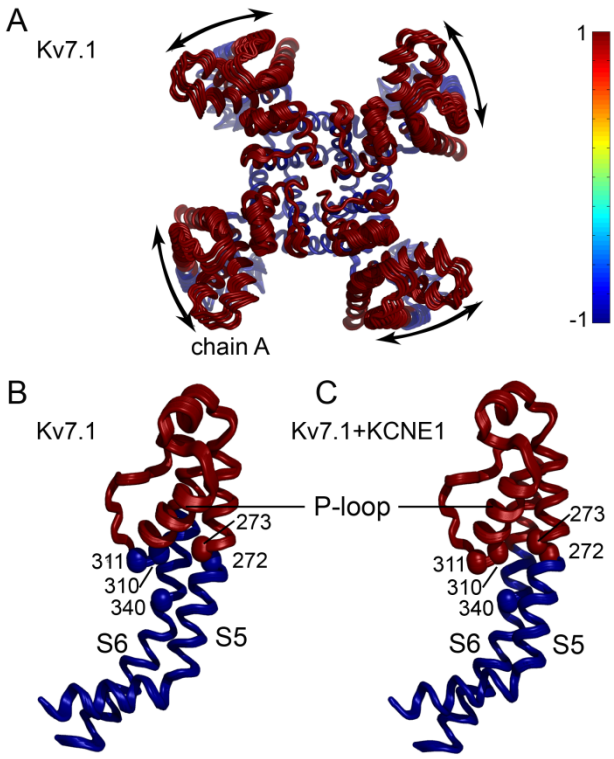

Figure 4.14. Changes in the cooperativity dynamics of motion IV of the isolated Kv7.1 channel upon association with KCNE1. The conformations predicted by ANM are colored according to the correlation of the chain A paddle with the other residues in the corresponding GNM mode (Table 4.2): (A, B) Channel conformations from ANM mode 5, colored according to the corresponding GNM mode 8. (C) Conformations of the channel in complex with KCNE1 from ANM mode 2, colored according to the corresponding GNM mode 7. The magnitude of positive and negative correlations between the fluctuations of the residues is color-coded according to the blue-to-red scale at the bottom. (A) Extracellular view of the channel tetramer. The direction of motion, detected by the ANM analysis, is marked with black arrows. (B, C) Side view of Kv7.1 segments S5 and S6 from a single chain in the absence (B) and presence (C) of KCNE1; the cross-correlations were identical for all four chains. The α-carbons of G272, L273, V310, T311 and F340 are shown as space-filled atoms. Notably, the correlation of residues G272, V310 and T311 with the other residues is reversed upon complex formation.

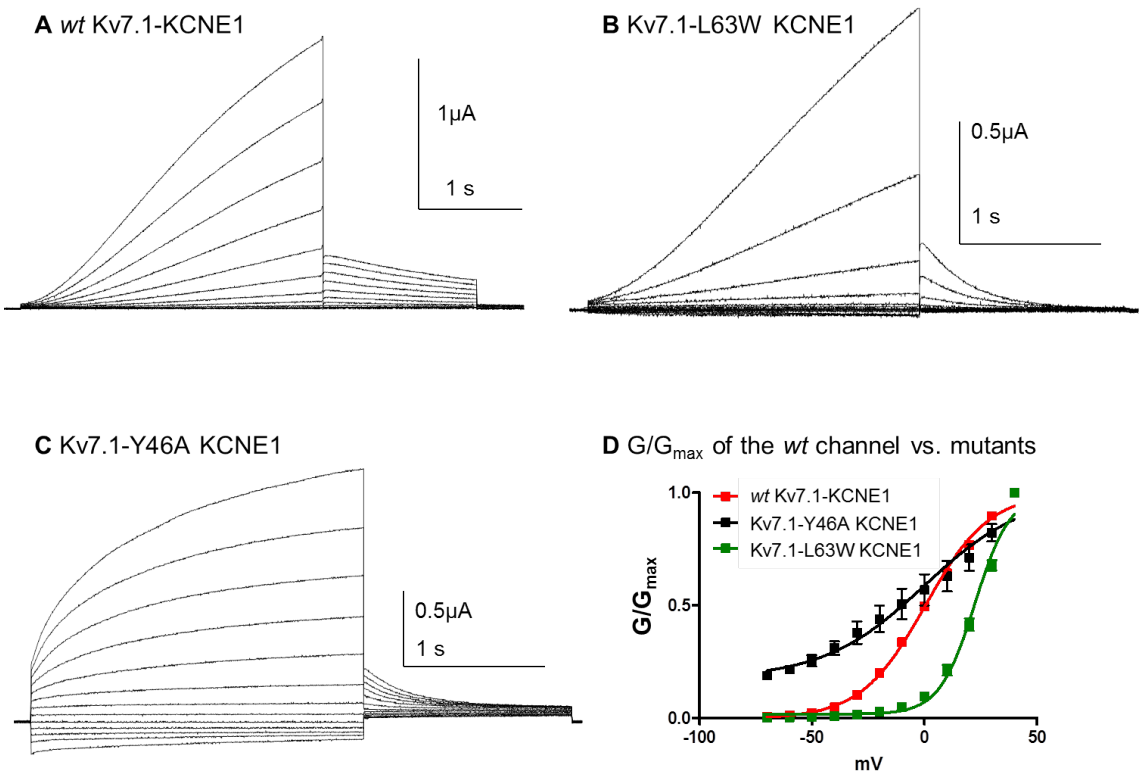

Figure 4.15. Electrophysiological properties of the *wt* Kv7.1-KCNE1 channel and two KCNE1 mutants, L63W and Y46A. (A-C), representative traces of the *wt* Kv7.1-KCNE1 (I_{KS}), Kv7.1-L63W KCNE1 and Kv7.1-Y46A KCNE1, respectively, expressed in *Xenopus* oocytes. The currents were recorded from 2.4 s depolarizing pulses of -140 mV to +40 mV, in 15 mV increments, from a holding potential of –80 mV. The tail currents were recorded at –60 mV. (D) normalized conductance-voltage relation of the *wt* Kv7.1-KCNE1, Kv7.1-L63W KCNE1 and Kv7.1-Y46A KCNE1. Voltage-dependent activation curves were fitted by a single Boltzmann function (Eq. 6). The experiments were performed by the lab of Prof. Attali

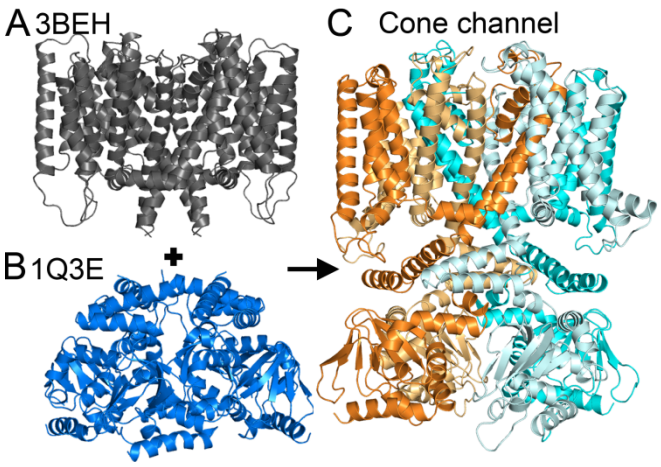

Figure 4.16. Modeling of the full-length cone channel in its resting state, based on two separate templates. (A) Side view of the TM region of the bacterial channel MlotiK1 in a closed state, PDB entry 3BEH (51). This structure was the template for modeling the TM region of the cone channel. (B) Side view of the mouse HCN2 CNBDs in a resting state, pdb entry 1Q3E (46). This structure served as a template for the cytosolic domain of the cone channel. (C) Side view of the resultant model-structure of the human cone channel, shown in cartoon representation. CNGA3 subunits are colored cyan (light and dark); CNGB3 subunits are colored orange (light and dark).

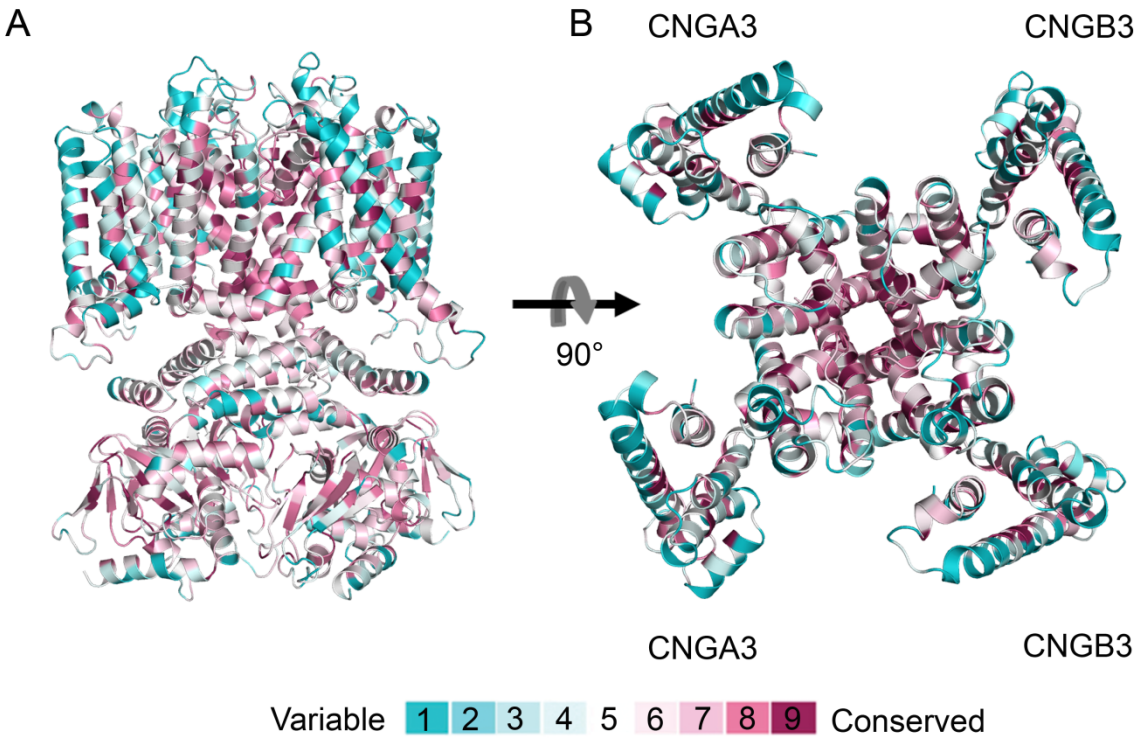

Figure 4.17. The evolutionary conservation profile of the cone channel model-structure is compatible with the typical conservation pattern. The channel is colored by conservation grades according to the color-coding bar, with variable-through-conserved corresponding to turquoise-through-maroon. Overall, the variable residues are peripheral, whereas the conserved residues are in the structural core and channel pore. (A) Side view of the model-structure in cartoon representation; the CNBDs are in their holo-state. (B) Extracellular view of the TM domain of the model-structure. The proposed locations of the CNGA3 and CNGB3 subunits are marked (68).

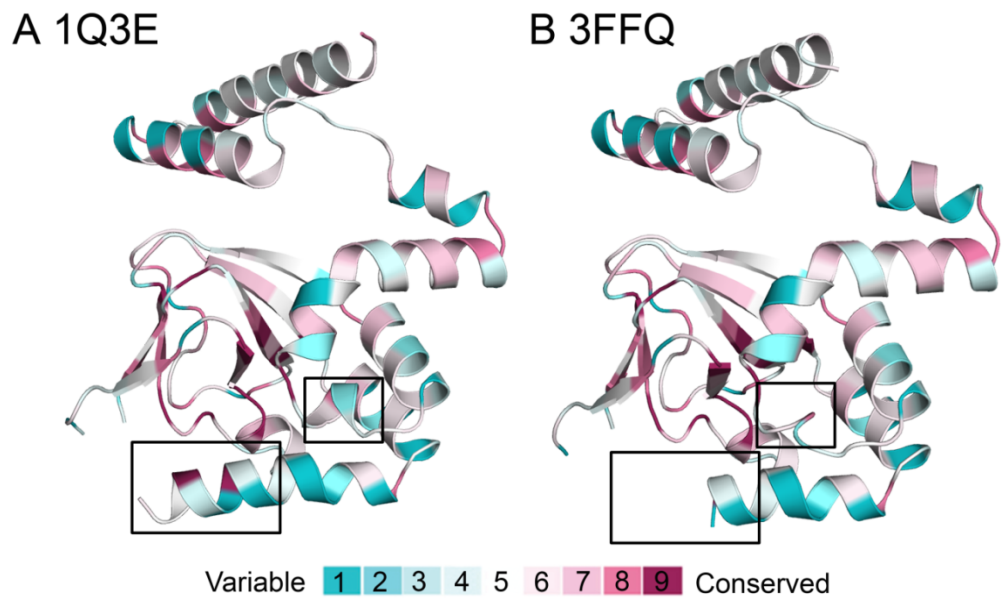

Figure 4.18. The evolutionary conservation of the high-resolution structures used as the templates for comparative modeling of the cytosolic domain of the cone channel. The proteins are colored by conservation grades according to the color-coding bar, with variable-through-conserved corresponding to turquoise-through-maroon. All structures display the typical conservation pattern, where the variable residues are peripheral, and the conserved residues are in the core of the channel. (A) Ligand-free CNBD from the mHCN2 channel, PDB entry 3FFQ (54). (B) cGMP-bound CNBD from the mHCN2 channel, PDB entry 1Q3E (46). The main differences between the ligand-free and cGMP-bound structures of the CNBDs are marked by black rectangles.

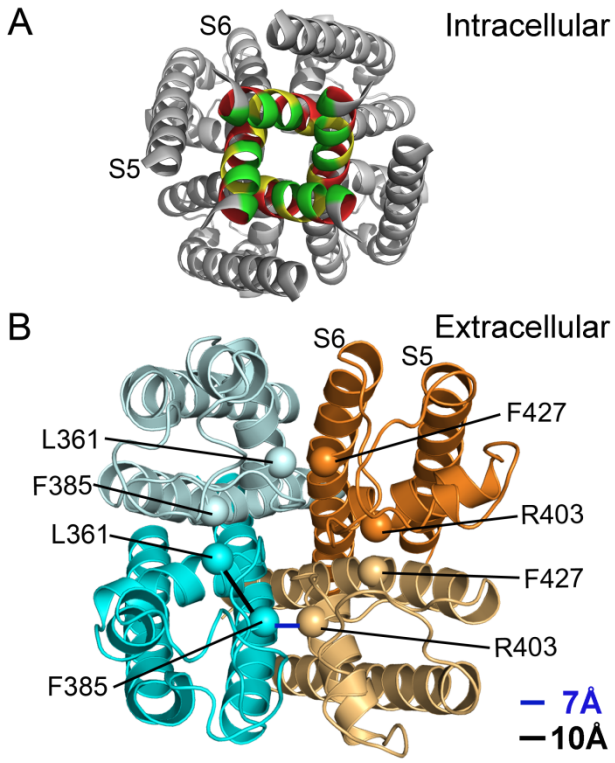

Figure 4.19. The model-structure of the human cone channel is in agreement with the available experimental data. (A) Intracellular view of the channel in cartoon representation. For clarity, the VSDs and CNBDs are omitted. The channel is colored grey. S6 residues accessible to the central pore are colored green; S6 residues with intermediate accessibility are colored yellow; S6 residues not accessible to the central pore are colored red (130,131). (B) Extracellular view of the cone channel in cartoon representation. For clarity, the VSDs and CNBDs are omitted. The CNGA3 subunits are colored cyan (light and dark), and the CNGB3 subunits are colored orange (light and dark); the α-carbons of CNGA3 L361 and F385 and the corresponding CNGB3 R403 and F427 are shown as space-filled atoms. The distance between the α-carbons of residues in the same subunit, e.g., the distance between the α-carbons of L361 and F385 in the CNGA3 subunit, was 10 Å (marked by a black line in one of the subunits); the distance between the α-carbons of the residues in neighboring subunits, e.g., the distance between the α-carbons of CNGA3 F385

and CNGB3 R403, was 7 Å (marked by a blue line in one of the subunits). It is apparent that the residues can interact with each other (132).

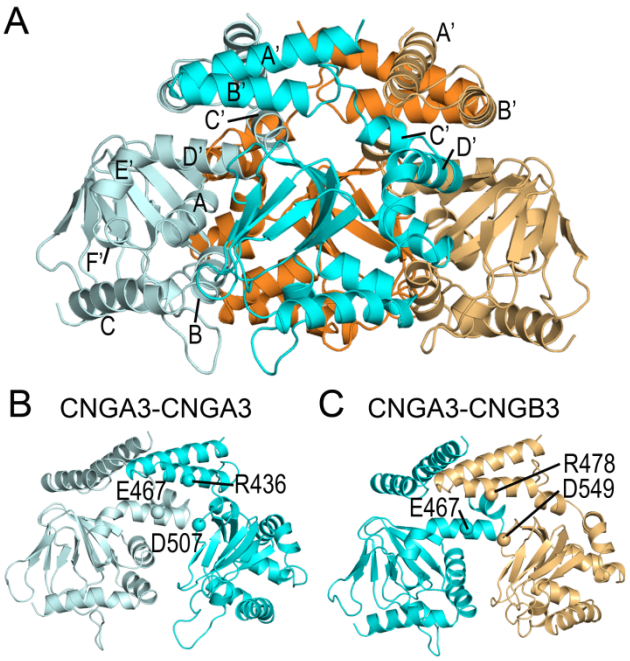

Figure 4.20. The model-structure of the human cone channel is in agreement with the available experimental data. (A) Side view of the CNBD tetramer in cartoon representation. For clarity, the TM domain is omitted. The CNGA3 subunits are colored cyan (light and dark) and the CNGB3 subunits are colored orange (light and dark). The helices composing the C-linker, A'-F', are marked; the helices of the CNBD, namely helices A-C, are marked in one of the subunits. The inter-subunit interaction called "elbow on a shoulder" is evident: the "elbow" comprises the A' and B' helices, which rest on the "shoulder," the C' and D' helices of the neighboring subunit. (B) Side view of two CNGA3 CNBDs from the cone channel in cartoon representation, colored cyan (light and dark). The α-carbons of R436, E467 and D507 are shown as space-filled atoms; the distance between the R436 Cα and the Cαs of both E467 and D507 is 11 Å. Hence, R436 can

form a salt bridge with E467 or D507, stabilizing the intra- and inter-subunit interface. (C) Side view of two CNBDs from the cone channel, CNGA3 and CNGB3, in cartoon representation, colored cyan and orange, respectively. The α-carbons of CNGA3 E467 and CNGB3 R478 and D549 are shown as space-filled atoms; the distance between the Cα of R436 and the α-carbons of the negatively charged residues is 11 Å. Therefore, R478 can form a salt bridge with E467 or D549, stabilizing either the intra- or inter-subunit interface.

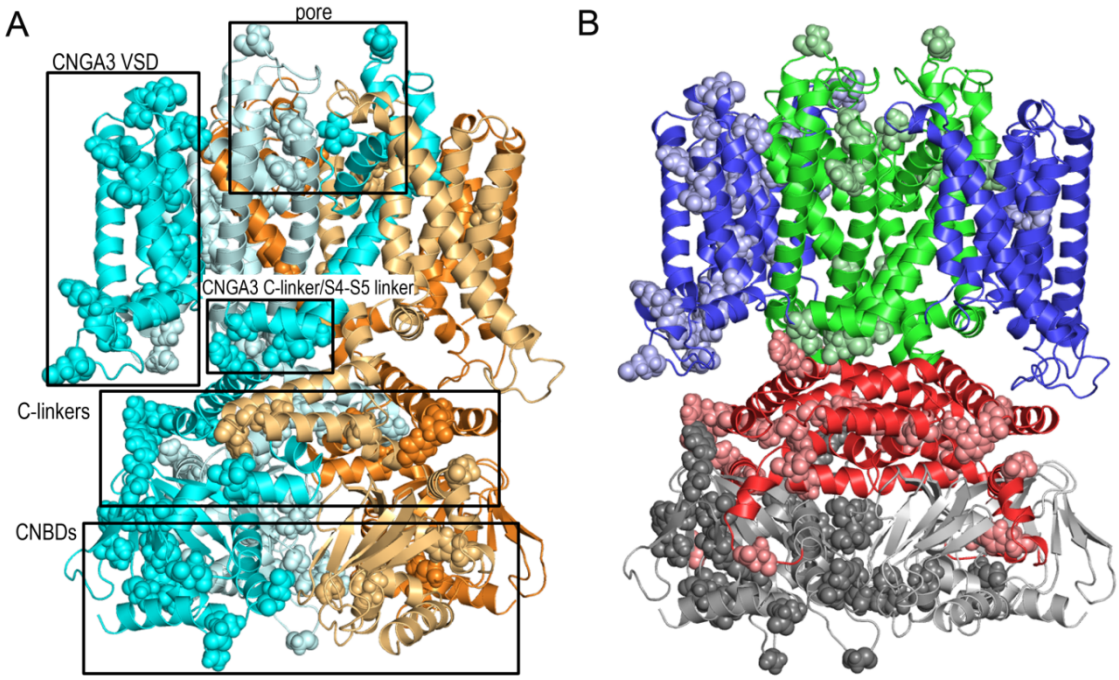

Figure 4.21. Mapping disease-causing mutations on the model-structure of the cone channel. CNGA3 subunits are colored cyan (light and dark); CNGB3 subunits are colored orange (light and dark). (A) Side view of the cone channel in cartoon representation. Residues with known disease-causing mutations are shown as space-filled atoms. Evidently, disease-causing mutations of the cone channel are clustered in several regions of the model-structure: the pore region, the C-linker, and the ligand-binding region. In addition, in CNGA3 subunits (cyan) the VSD and the

interface between the C-linker and the S4-S5 linker contain several positions with disease-causing mutations. (B) For clarity, the cone channel is presented from the same view, but colored according to the functional domains: the VSDs are blue, the pore domain is green, the C-linkers are red and the CNBDs are grey. Residues with known disease-causing mutations are shown as space-filled atoms and colored according to the functional domains to which they belong: light blue, light green, light red and dark grey for disease-causing mutations in the VSDs, the pore domain, the C-linkers and the CNBDs, respectively.

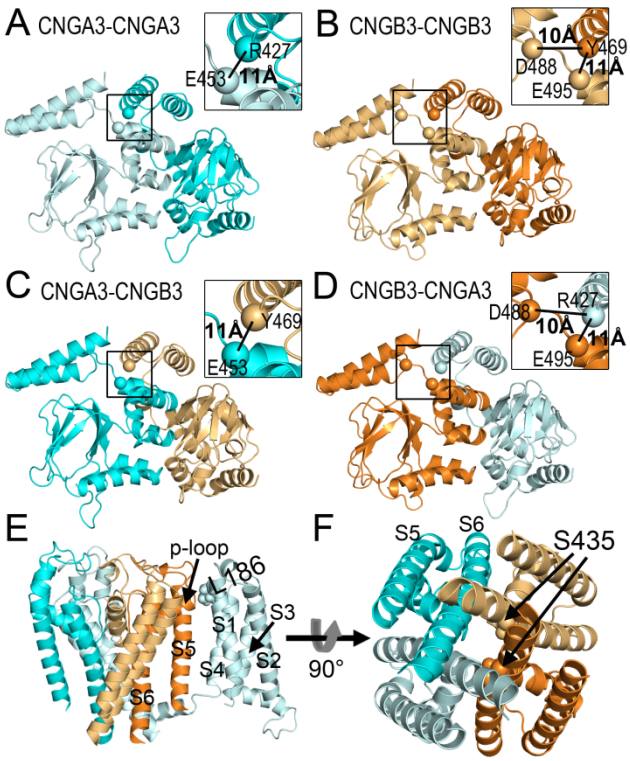

Figure 4.22. Molecular interpretations for disease-causing mutations mapped on the model-structure of the cone channel. (A-D) The effect of the CNGA3 R427C mutation and the corresponding CNGB3 Y469D mutation. In each panel CNBDs from two neighboring subunits are shown in side view. The α-carbons of CNGA3 R427 and E453, as well as of CNGB3 Y469,

D488, and E495, are presented as space-filled atoms. The insets show a closer view of the residues' interactions, marked by black rectangles on the main panels. It is clear that CNGA3 R427 could interact with CNGA3 E453 (A) or CNGB3 D488 and E495 (D). Abolishment of the positive charge at the position R427C may disrupt the inter-subunit electrostatic interactions. Similarly, the negative charge resulting from mutation of CNGB3 Y469 to D could result in repulsion of the mutated residue by the negatively charged CNGA3 E453 (C) or by CNGB3 D488 and E495 (B). The distances of the interacting residues are marked. (E) The effect of the CNGA3 L186F mutation. A side view of the TM region of the cone channel is presented; for clarity only one VSD is shown. CNGA3 L186, shown as space-filled atoms, is located at the interface of the VSD with the p-loop. Substitution of L186 with a bulky F can interrupt the tight interface. (F) The effect of the CNGB3 S435F mutation. An intracellular view of the pore region of the cone channel is presented. S435 faces the central pore, and its substitution with a bulky F can disrupt the helix bundle and/or block the pore.

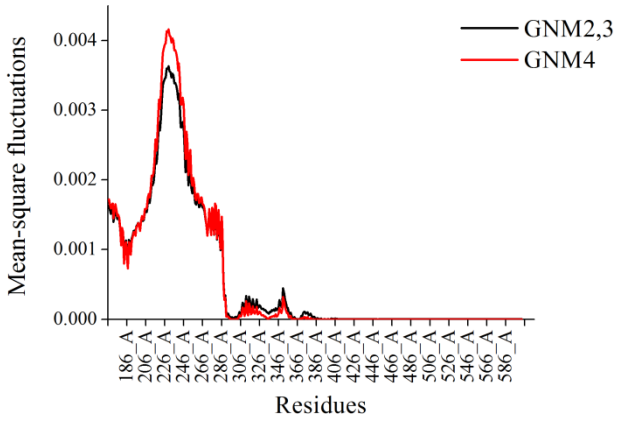

Figure 4.23. Mean-square fluctuations of the CNGA3 tetramer in holo-state in GNM modes 2-4. The shape of mode 4 (red) fits the profile of the average of modes 2 and 3 (black). The

fluctuations of one chain of the homotetrameric channel are presented, since the fluctuations of the four chains are identical.

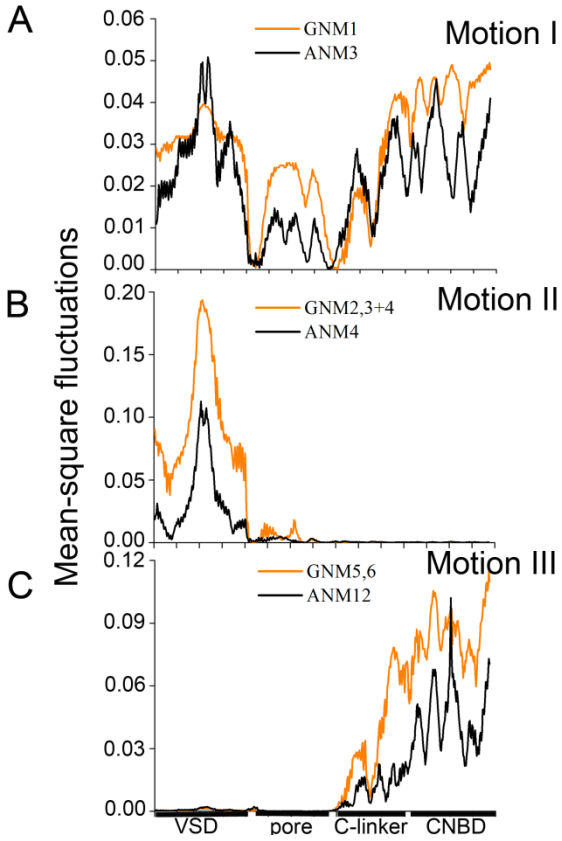

Figure 4.24. Mean-square displacement of the CNGA3 channel in the holo-state according to the GNM and ANM modes. (A) Motion I: the shape of GNM mode 1 fits the profile of ANM mode 3. (B) Motion II: the average shape of GNM modes 2-4 fits the profile of ANM mode 4. (C) Motion III: the average shape of GNM modes 5 and 6 fits the profile of ANM mode 12. The fluctuations of one chain are demonstrated, since the fluctuations of all four chains are identical. The locations of the VSD, the pore, the C-linker and the CNBD are marked on the x-axis. The fluctuations of the channel in the apo-state according to GNM and ANM are almost identical (not shown).

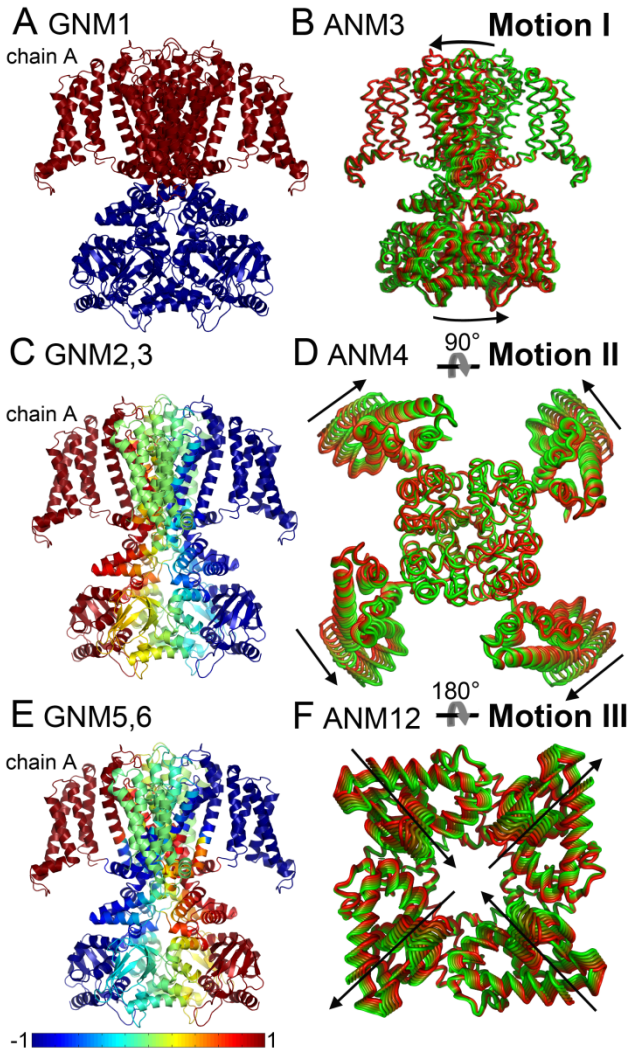

Figure 4.25. Association of GNM and ANM modes of motion of the homotetrameric CNGA3 channel. In each panel, chain A represents an arbitrary CNGA3 chain (the channel comprises four identical chains). (A, B) Motion I: GNM mode 1 is associated with ANM mode 3. (A) Side view of the channel in cartoon representation, colored according to the correlation of the VSD of chain A with the other residues in GNM mode 1. (B) Conformations of ANM mode 3, colored according to the direction of motion, ranging from green to red (extracellular view). (C, D) Motion II: GNM modes 2 and 3 are associated with ANM mode 4. (C) Side view of the channel in cartoon representation, colored according to the correlation of the chain A VSD with the other residues in GNM modes 2 and 3. (D) Conformations of ANM mode 4, colored according to the

direction of motion, ranging from green to red (extracellular view, CNBDs are omitted for clarity). (E, F) Motion III: GNM modes 5 and 6 are associated with ANM mode 12. (E) Side view of the channel in cartoon representation, colored according to the correlation of the chain A VSD with the other residues in GNM modes 5 and 6. (F) Conformations of ANM mode 12, colored according to the direction of motion, ranging from green to red (intracellular view, the TM domain is omitted for clarity). (A, C, E) The magnitude of positive and negative correlations between the fluctuations of the residues is color-coded according to the blue-to-red scale at the bottom of the picture. Positive correlation indicates motion of two residues in the same direction, while negative correlation indicates motion in opposite directions.

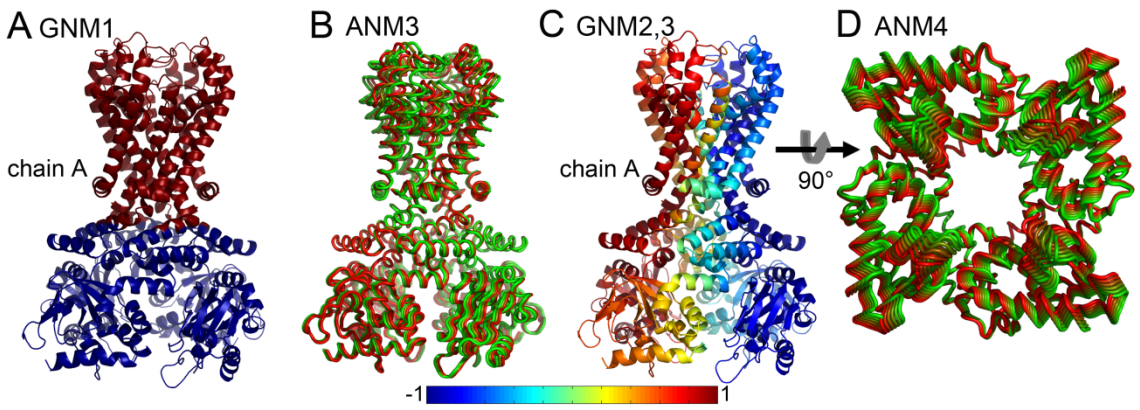

Figure 4.26. Association of GNM and ANM modes of motion of the homotetrameric CNGA3 channel lacking the VSDs. In each panel, chain A represents an arbitrary CNGA3 chain (the channel comprises four identical chains). (A, B) GNM mode 1 is associated with ANM mode 3. (A) Side view of the channel in cartoon representation colored according to the correlation of the S5 helix in chain A with the other residues in GNM mode 1. (B) Conformations of ANM mode 3, colored according to the direction of motion, ranging from green to red (side view). (C, D) GNM modes 2 and 3 are associated with ANM mode 4. (C) Side view of the channel in cartoon

representation, colored according to the correlation of the chain A S5 with the other residues in GNM modes 2 and 3. (D) Conformations of ANM mode 4, colored according to the direction of motion, ranging from green to red (intracellular view). (A, C) The magnitude of positive and negative correlations between the fluctuations of the residues is color-coded according to the blue-to-red scale at the bottom of the picture. Positive correlation indicates motion of two residues in the same direction, while negative correlation indicates motion in opposite directions.

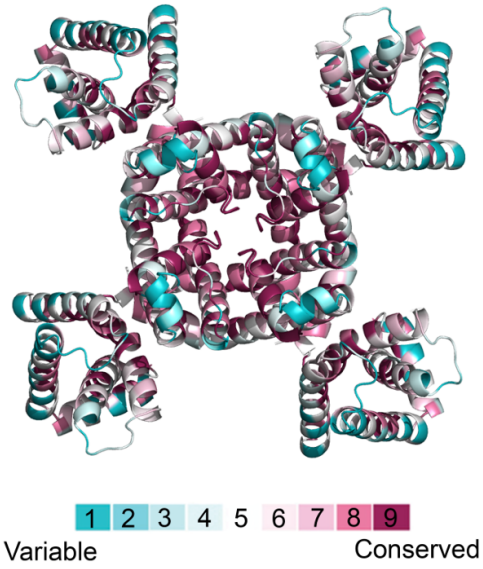

Figure 5.1. ConSurf (83) analysis of the Kv7.1 homology model by Smith and colleagues (42) supports the accuracy of the model. An extracellular view of the channel is colored by conservation grades according to the color-coding bar, with variable-through-conserved corresponding to turquoise-through-maroon. Variable residues face the lipid or are located in the loops, whereas conserved residues are located in the channel core, as expected.

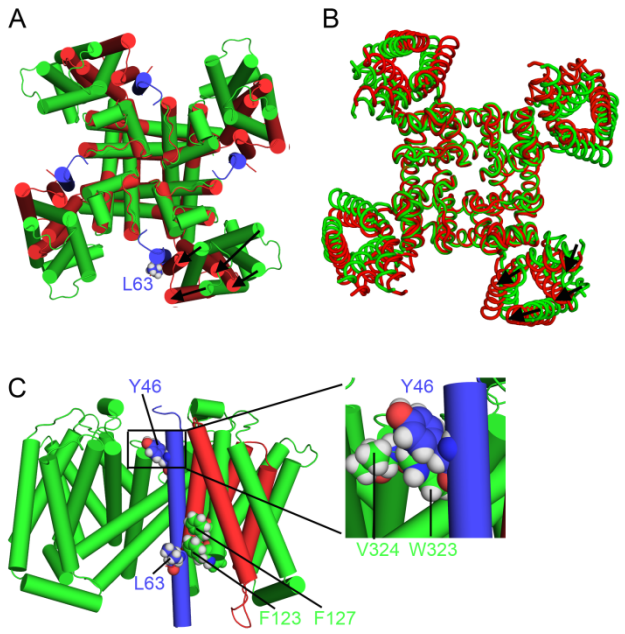

Figure 5.2. Association of Kv7.1 motion II with channel deactivation. (A) Extracellular view of the Kv7.1 model-structure in an open state (colored green) and the closed structure of bacterial potassium channel MlotK1 (colored red) aligned according to the pore domain. Both proteins are shown in cylinder representation. The arrows indicate possible direction of transition between the open and closed states. The KCNE1 subunits are in blue, and L63 is shown as space-filled atoms. (B) Kv7.1 conformations as predicted by ANM mode 1 (motion II); only two edge conformations are presented (in red and green). The arrows denote the direction of the motion. The loops connecting S1 and S2, as well as S3 and S4, are omitted for clarity. (C) The Kv7.1 model-structure in the open state (green) and the closed structure of the bacterial potassium channel MlotK1 (red) aligned according to the pore domain (side view). For clarity, only one VSD of MlotK1 and one KCNE1 subunit are shown. Both proteins are shown in cylinder representation. The KCNE1 subunit is in blue, and Y46 and L63 are shown as space-filled atoms. Kv7.1 F123 and F127 are shown as space-filled atoms. The inset shows the tight interface between Kv7.1 S6 and KCNE1; Kv7.1 W323 and V324 are also shown as space-filled atoms.

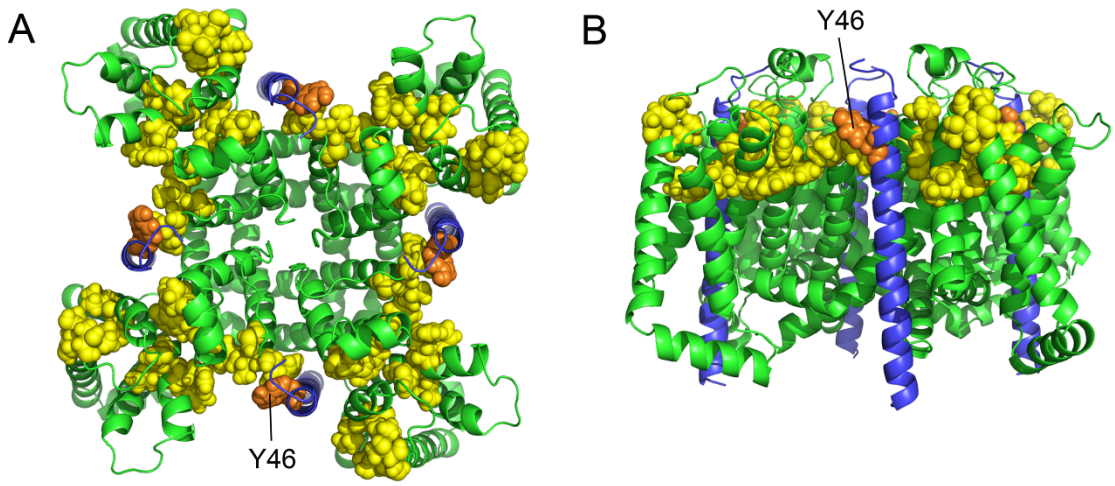

Figure 5.3. Hinges controlling motion II mapped on the model-structure of the Kv7.1-KCNE1 complex: (A) extracellular view, (B) side view. The Kv7.1 channel is green and KCNE1 is blue. The hinge residues of motion II are shown as yellow space-filled atoms. KCNE1 Y46 is shown as orange space-filled atoms. Clearly, the hinge residues are in close proximity to each other, creating a cluster, and KCNE1 Y46 is a part of this cluster.

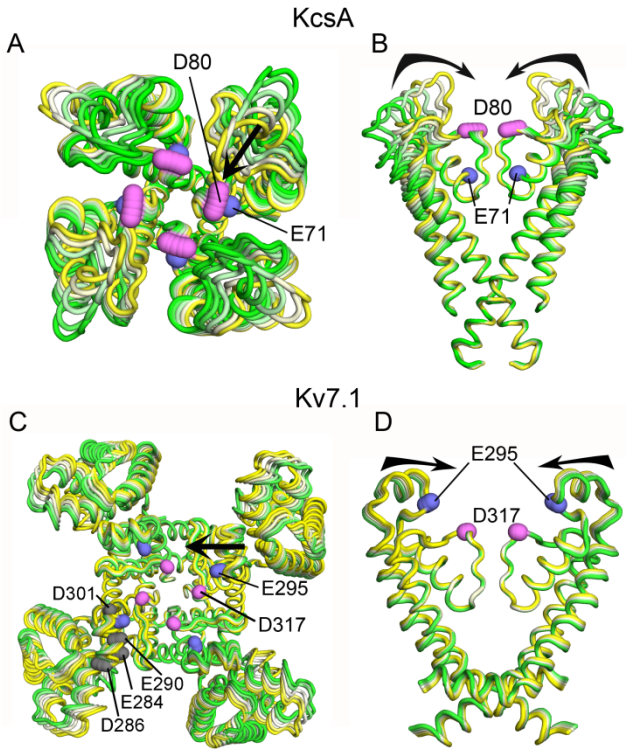

Figure 5.4. Two negatively charged residues may affect slow voltage-dependent inactivation of Kv7.1. (A, B) KcsA conformations predicted by the ANM mode related to channel inactivation are shown. The conformations were reproduced using HingeProt (110) and colored according to the direction of motion, ranging from yellow to white and green. The α-carbons of E71 and D80 are shown as blue and pink space-filled atoms, respectively. (C, D) The conformations predicted by ANM mode 8, related to slow voltage-dependent inactivation in Kv7.1, are colored according to the direction of motion, ranging from yellow to white and green. The α-carbons of E295 and D317 are shown as blue and pink space-filled atoms, respectively. In (C) the α-carbons of E284, D286, E290 and D301 of one of the chains are shown as grey space-filled atoms. (A, C) Extracellular view. (B, D) Side view; for clarity the pore domains of only two chains are presented.

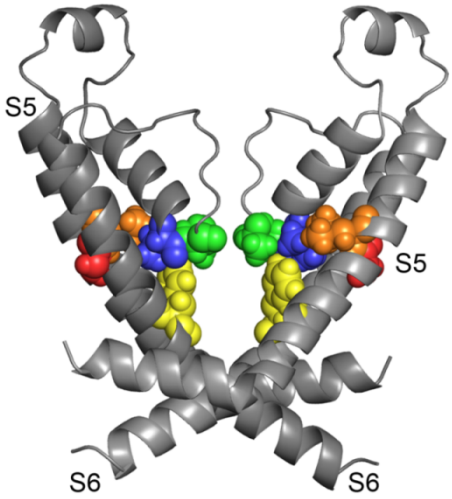

Figure 5.5. The location of residues G272 (red), L273 (orange), V310 (blue), T311 (green) and F340 (yellow) in the Kv7.1 model-structure. Segments S5 and S6 of two diagonally-opposite chains are presented. Residues G272, L273, V310, T311 and F340 are shown as space-filled atoms. These five residues are in close proximity to each other, creating a cluster.

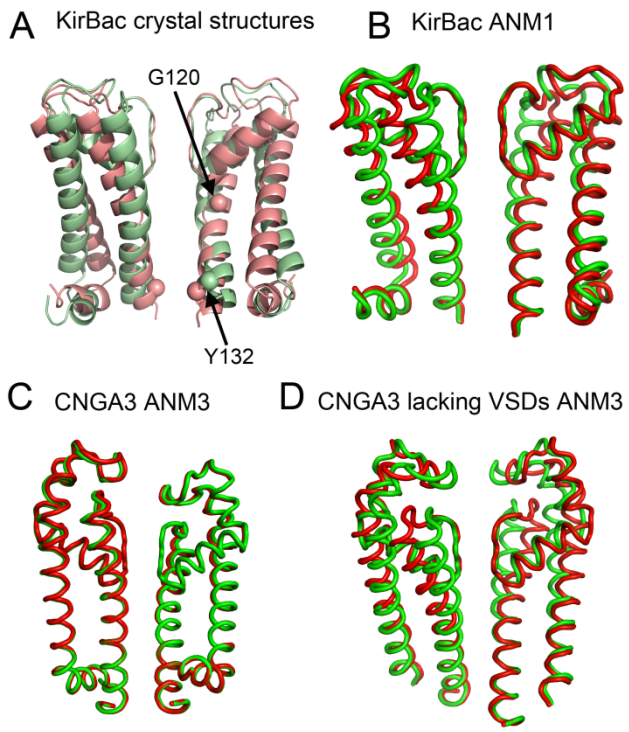

Figure 5.6. Motion I of the tetrameric CNGA3 channel appears to describe its gating. (A) Side view of the KirBac3.1 crystal structures in an open state (pale green, PDB entry 3ZRS (164) and in a closed state (pale red, PDB entry 2WLJ (165)). The α-carbons of the two gate-residues, namely G120 and Y132, are shown as space-filled atoms. (B) The two edge KirBac3.1 conformations, as predicted by the slowest ANM mode, are shown in red and green. The similarity between the ANM conformations and the crystal structures in panel A is apparent, verifying the relationship between these conformations and channel gating. (C) The two edge CNGA3 conformations, as predicted by ANM mode 3, are shown in red and green. The VSDs are omitted for clarity. The conformations resemble the conformations predicted for the KirBac channel (panel B), but the pore region is rigid. (D) The two edge CNGA3 conformations in the absence of VSDs, as predicted by ANM mode 3, are shown in red and green. The conformations are identical to the KirBac conformations (panel B). For clarity, only helices S5 and S6 (or corresponding helices) of two juxtaposed subunits are shown in all panels.

References

1. Yu, F.H. and Catterall, W.A. (2004) The VGL-chanome: a protein superfamily specialized for electrical signaling and ionic homeostasis. *Sci. STKE*, **2004**, re15.
2. Doyle, D.A., Morais Cabral, J., Pfuetzner, R.A., Kuo, A., Gulbis, J.M., Cohen, S.L., Chait, B.T. and MacKinnon, R. (1998) The structure of the potassium channel: molecular basis of K+ conduction and selectivity. *Science*, **280**, 69-77.
3. MacKinnon, R. (2004) Nobel Lecture. Potassium channels and the atomic basis of selective ion conduction. *Biosci Rep*, **24**, 75-100.
4. Jiang, Y., Lee, A., Chen, J., Cadene, M., Chait, B.T. and MacKinnon, R. (2002) Crystal structure and mechanism of a calcium-gated potassium channel. *Nature*, **417**, 515-522.
5. Kuo, A., Gulbis, J.M., Antcliff, J.F., Rahman, T., Lowe, E.D., Zimmer, J., Cuthbertson, J., Ashcroft, F.M., Ezaki, T. and Doyle, D.A. (2003) Crystal structure of the potassium channel KirBac1.1 in the closed state. *Science*, **300**, 1922-1926.
6. Shi, N., Ye, S., Alam, A., Chen, L. and Jiang, Y. (2006) Atomic structure of a Na+- and K+-conducting channel. *Nature*, **440**, 570-574.
7. Long, S.B., Campbell, E.B. and Mackinnon, R. (2005) Crystal structure of a mammalian voltage-dependent Shaker family K+ channel. *Science*, **309**, 897-903.
8. Chen, X., Wang, Q., Ni, F. and Ma, J. (2010) Structure of the full-length Shaker potassium channel Kv1.2 by normal-mode-based X-ray crystallographic refinement. *Proc Natl Acad Sci U S A*, **107**, 11352-11357.
9. Long, S.B., Tao, X., Campbell, E.B. and MacKinnon, R. (2007) Atomic structure of a voltage-dependent K+ channel in a lipid membrane-like environment. *Nature*, **450**, 376-382.
10. Swartz, K.J. (2008) Sensing voltage across lipid membranes. *Nature*, **456**, 891-897.
11. Cerda, O. and Trimmer, J.S. (2010) Analysis and functional implications of phosphorylation of neuronal voltage-gated potassium channels. *Neurosci. Lett.*, **486**, 60-67.
12. Pongs, O. and Schwarz, J.R. (2010) Ancillary subunits associated with voltage-dependent K+ channels. *Physiol Rev*, **90**, 755-796.
13. Zhou, M., Morais-Cabral, J.H., Mann, S. and MacKinnon, R. (2001) Potassium channel receptor site for the inactivation gate and quaternary amine inhibitors. *Nature*, **411**, 657-661.
14. Pioletti, M., Findeisen, F., Hura, G.L. and Minor, D.L., Jr. (2006) Three-dimensional structure of the KChIP1-Kv4.3 T1 complex reveals a cross-shaped octamer. *Nat Struct Mol Biol*, **13**, 987-995.
15. Schushan, M. and Ben-Tal, N. (2010) In Rangwala, H. and Karypis, G. (eds.), *Introduction to Protein Structure Prediction*. John Wiley & Sons, Inc., pp. 369-401.
16. Petrey, D. and Honig, B. (2005) Protein structure prediction: inroads to biology. *Molecular cell*, **20**, 811-819.
17. Levit, A., Barak, D., Behrens, M., Meyerhof, W. and Niv, M.Y. (2012) Homology model-assisted elucidation of binding sites in GPCRs. *Methods Mol Biol*, **914**, 179-205.
18. Ravna, A.W. and Sylte, I. (2012) Homology modeling of transporter proteins (carriers and ion channels). *Methods Mol Biol*, **857**, 281-299.
19. Kalman, M. and Ben-Tal, N. (2010) Quality assessment of protein model-structures using evolutionary conservation. *Bioinformatics*, **26**, 1299-1307.
20. Ashcroft, F.M. (2000) *Ion Channels and Diseases*. Academic Press, Oxford.

21. Camerino, D.C., Tricarico, D. and Desaphy, J.F. (2007) Ion channel pharmacology. *Neurotherapeutics*, **4**, 184-198.
22. Murata, Y., Iwasaki, H., Sasaki, M., Inaba, K. and Okamura, Y. (2005) Phosphoinositide phosphatase activity coupled to an intrinsic voltage sensor. *Nature*, **435**, 1239-1243.
23. Ramsey, I.S., Moran, M.M., Chong, J.A. and Clapham, D.E. (2006) A voltage-gated proton-selective channel lacking the pore domain. *Nature*, **440**, 1213-1216.
24. Sasaki, M., Takagi, M. and Okamura, Y. (2006) A voltage sensor-domain protein is a voltage-gated proton channel. *Science*, **312**, 589-592.
25. Lee, S.Y., Letts, J.A. and MacKinnon, R. (2009) Functional reconstitution of purified human Hv1 H+ channels. *J Mol Biol*, **387**, 1055-1060.
26. Jiang, Y., Lee, A., Chen, J., Ruta, V., Cadene, M., Chait, B.T. and MacKinnon, R. (2003) X-ray structure of a voltage-dependent K+ channel. *Nature*, **423**, 33-41.
27. Alabi, A.A., Bahamonde, M.I., Jung, H.J., Kim, J.I. and Swartz, K.J. (2007) Portability of paddle motif function and pharmacology in voltage sensors. *Nature*, **450**, 370-375.
28. Brown, D.A. and Passmore, G.M. (2009) Neural KCNQ (Kv7) channels. *Br. J. Pharmacol.*, **156**, 1185-1195.
29. Peretz, A., Degani-Katzav, N., Talmon, M., Danieli, E., Gopin, A., Malka, E., Nachman, R., Raz, A., Shabat, D. and Attali, B. (2007) A tale of switched functions: from cyclooxygenase inhibition to M-channel modulation in new diphenylamine derivatives. *PLoS One*, **2**, e1332.
30. Delmas, P. and Brown, D.A. (2005) Pathways modulating neural KCNQ/M (Kv7) potassium channels. *Nat Rev Neurosci*, **6**, 850-862.
31. Jentsch, T.J. (2000) Neuronal KCNQ potassium channels: physiology and role in disease. *Nat. Rev. Neurosci.*, **1**, 21-30.
32. Siemens, J., Zhou, S., Piskorowski, R., Nikai, T., Lumpkin, E.A., Basbaum, A.I., King, D. and Julius, D. (2006) Spider toxins activate the capsaicin receptor to produce inflammatory pain. *Nature*, **444**, 208-212.
33. Swartz, K.J. (2007) Tarantula toxins interacting with voltage sensors in potassium channels. *Toxicon*, **49**, 213-230.
34. Catterall, W.A., Cestele, S., Yarov-Yarovoy, V., Yu, F.H., Konoki, K. and Scheuer, T. (2007) Voltage-gated ion channels and gating modifier toxins. *Toxicon*, **49**, 124-141.
35. Jespersen, T., Grunnet, M. and Olesen, S.P. (2005) The KCNQ1 potassium channel: from gene to physiological function. *Physiology*, **20**, 408-416.
36. Van Horn, W.D., Vanoye, C.G. and Sanders, C.R. (2011) Working model for the structural basis for KCNE1 modulation of the KCNQ1 potassium channel. *Curr. Opin. Struct. Biol.*, **21**, 283-291.
37. Chen, H., Kim, L.A., Rajan, S., Xu, S. and Goldstein, S.A. (2003) Charybdotoxin binding in the I(Ks) pore demonstrates two MinK subunits in each channel complex. *Neuron*, **40**, 15-23.
38. Morin, T.J. and Kobertz, W.R. (2008) Counting membrane-embedded KCNE beta-subunits in functioning K+ channel complexes. *Proc. Natl. Acad. Sci. USA*, **105**, 1478-1482.
39. Nakajo, K., Ulbrich, M.H., Kubo, Y. and Isacoff, E.Y. (2010) Stoichiometry of the KCNQ1 - KCNE1 ion channel complex. *Proc. Natl. Acad. Sci. USA*, **107**, 18862-18867.
40. Wang, W., Xia, J. and Kass, R.S. (1998) MinK-KvLQT1 fusion proteins, evidence for multiple stoichiometries of the assembled IsK channel. *J. Biol. Chem.*, **273**, 34069-34074.

41. Kang, C., Tian, C., Sonnichsen, F.D., Smith, J.A., Meiler, J., George, A.L., Jr., Vanoye, C.G., Kim, H.J. and Sanders, C.R. (2008) Structure of KCNE1 and implications for how it modulates the KCNQ1 potassium channel. *Biochemistry*, **47**, 7999-8006.
42. Smith, J.A., Vanoye, C.G., George, A.L., Jr., Meiler, J. and Sanders, C.R. (2007) Structural models for the KCNQ1 voltage-gated potassium channel. *Biochemistry*, **46**, 14141-14152.
43. Biel, M. and Michalakis, S. (2007) Function and dysfunction of CNG channels: insights from channelopathies and mouse models. *Mol Neurobiol*, **35**, 266-277.
44. Matulef, K. and Zagotta, W.N. (2003) Cyclic nucleotide-gated ion channels. *Annu Rev Cell Dev Biol*, **19**, 23-44.
45. Wang, Z., Jiang, Y., Lu, L., Huang, R., Hou, Q. and Shi, F. (2007) Molecular mechanisms of cyclic nucleotide-gated ion channel gating. *J Genet Genomics*, **34**, 477-485.
46. Zagotta, W.N., Olivier, N.B., Black, K.D., Young, E.C., Olson, R. and Gouaux, E. (2003) Structural basis for modulation and agonist specificity of HCN pacemaker channels. *Nature*, **425**, 200-205.
47. Altieri, S.L., Clayton, G.M., Silverman, W.R., Olivares, A.O., De la Cruz, E.M., Thomas, L.R. and Morais-Cabral, J.H. (2008) Structural and energetic analysis of activation by a cyclic nucleotide binding domain. *J Mol Biol*, **381**, 655-669.
48. Clayton, G.M., Silverman, W.R., Heginbotham, L. and Morais-Cabral, J.H. (2004) Structural basis of ligand activation in a cyclic nucleotide regulated potassium channel. *Cell*, **119**, 615-627.
49. Schunke, S., Stoldt, M., Lecher, J., Kaupp, U.B. and Willbold, D. (2011) Structural insights into conformational changes of a cyclic nucleotide-binding domain in solution from Mesorhizobium loti K1 channel. *Proc Natl Acad Sci U S A*, **108**, 6121-6126.
50. Schunke, S., Stoldt, M., Novak, K., Kaupp, U.B. and Willbold, D. (2009) Solution structure of the Mesorhizobium loti K1 channel cyclic nucleotide-binding domain in complex with cAMP. *EMBO Rep*, **10**, 729-735.
51. Clayton, G.M., Altieri, S., Heginbotham, L., Unger, V.M. and Morais-Cabral, J.H. (2008) Structure of the transmembrane regions of a bacterial cyclic nucleotide-regulated channel. *Proc. Natl. Acad. Sci. USA*, **105**, 1511-1515.
52. Flynn, G.E., Black, K.D., Islas, L.D., Sankaran, B. and Zagotta, W.N. (2007) Structure and rearrangements in the carboxy-terminal region of SpIH channels. *Structure*, **15**, 671-682.
53. Craven, K.B., Olivier, N.B. and Zagotta, W.N. (2008) C-terminal movement during gating in cyclic nucleotide-modulated channels. *J Biol Chem*, **283**, 14728-14738.
54. Taraska, J.W., Puljung, M.C., Olivier, N.B., Flynn, G.E. and Zagotta, W.N. (2009) Mapping the structure and conformational movements of proteins with transition metal ion FRET. *Nat Methods*, **6**, 532-537.
55. Xu, X., Vysotskaya, Z.V., Liu, Q. and Zhou, L. (2010) Structural basis for the cAMP-dependent gating in the human HCN4 channel. *J Biol Chem*, **285**, 37082-37091.
56. Lolicato, M., Nardini, M., Gazzarrini, S., Moller, S., Bertinetti, D., Herberg, F.W., Bolognesi, M., Martin, H., Fasolini, M., Bertrand, J.A. *et al.* (2011) Tetramerization dynamics of C-terminal domain underlies isoform-specific cAMP gating in hyperpolarization-activated cyclic nucleotide-gated channels. *J Biol Chem*, **286**, 44811-44820.
57. Craven, K.B. and Zagotta, W.N. (2006) CNG and HCN channels: two peas, one pod. *Annu Rev Physiol*, **68**, 375-401.

58. Karpen, J.W. and Ruiz, M. (2002) Ion channels: does each subunit do something on its own? *Trends Biochem Sci*, **27**, 402-409.
59. Cukkemane, A., Seifert, R. and Kaupp, U.B. (2011) Cooperative and uncooperative cyclic-nucleotide-gated ion channels. *Trends Biochem Sci*, **36**, 55-64.
60. Rehmann, H., Wittinghofer, A. and Bos, J.L. (2007) Capturing cyclic nucleotides in action: snapshots from crystallographic studies. *Nat Rev Mol Cell Biol*, **8**, 63-73.
61. Richards, M.J. and Gordon, S.E. (2000) Cooperativity and cooperation in cyclic nucleotide-gated ion channels. *Biochemistry*, **39**, 14003-14011.
62. Karpen, J.W., Zimmerman, A.L., Stryer, L. and Baylor, D.A. (1988) Gating kinetics of the cyclic-GMP-activated channel of retinal rods: flash photolysis and voltage-jump studies. *Proc Natl Acad Sci U S A*, **85**, 1287-1291.
63. Tibbs, G.R., Goulding, E.H. and Siegelbaum, S.A. (1997) Allosteric activation and tuning of ligand efficacy in cyclic-nucleotide-gated channels. *Nature*, **386**, 612-615.
64. Monod, J., Wyman, J. and Changeux, J.P. (1965) On the Nature of Allosteric Transitions: A Plausible Model. *J Mol Biol*, **12**, 88-118.
65. Liu, D.T., Tibbs, G.R., Paoletti, P. and Siegelbaum, S.A. (1998) Constraining ligand-binding site stoichiometry suggests that a cyclic nucleotide-gated channel is composed of two functional dimers. *Neuron*, **21**, 235-248.
66. Craven, K.B. and Zagotta, W.N. (2004) Salt bridges and gating in the COOH-terminal region of HCN2 and CNGA1 channels. *J Gen Physiol*, **124**, 663-677.
67. Kaupp, U.B. and Seifert, R. (2002) Cyclic nucleotide-gated ion channels. *Physiol Rev*, **82**, 769-824.
68. Peng, C., Rich, E.D. and Varnum, M.D. (2004) Subunit configuration of heteromeric cone cyclic nucleotide-gated channels. *Neuron*, **42**, 401-410.
69. Reuter, P., Koeppen, K., Ladewig, T., Kohl, S., Baumann, B. and Wissinger, B. (2008) Mutations in CNGA3 impair trafficking or function of cone cyclic nucleotide-gated channels, resulting in achromatopsia. *Hum Mutat*, **29**, 1228-1236.
70. Biskup, C., Kusch, J., Schulz, E., Nache, V., Schwede, F., Lehmann, F., Hagen, V. and Benndorf, K. (2007) Relating ligand binding to activation gating in CNGA2 channels. *Nature*, **446**, 440-443.
71. Goldenberg, O., Erez, E., Nimrod, G. and Ben-Tal, N. (2009) The ConSurf-DB: pre-calculated evolutionary conservation profiles of protein structures. *Nucleic Acids Res*, **37**, D323-327.
72. Katoh, K., Kuma, K., Toh, H. and Miyata, T. (2005) MAFFT version 5: improvement in accuracy of multiple sequence alignment. *Nucleic Acids Res*, **33**, 511-518.
73. Petrey, D., Xiang, Z., Tang, C.L., Xie, L., Gimpelev, M., Mitros, T., Soto, C.S., Goldsmith-Fischman, S., Kernytsky, A., Schlessinger, A. *et al.* (2003) Using multiple structure alignments, fast model building, and energetic analysis in fold recognition and homology modeling. *Proteins*, **53 Suppl 6**, 430-435.
74. Jacobson, M.P., Friesner, R.A., Xiang, Z. and Honig, B. (2002) On the role of the crystal environment in determining protein side-chain conformations. *J Mol Biol*, **320**, 597-608.
75. Venkatachalam, C.M., Jiang, X., Oldfield, T. and Waldman, M. (2003) LigandFit: a novel method for the shape-directed rapid docking of ligands to protein active sites. *J Mol Graph Model*, **21**, 289-307.
76. Mayo, S.L., Olafson, BD, Goddard, WA. (1990) Dreiding - a generic force-field for molecular simulations. *J Phys Chem*, **94**, 8897–8909.

77. Krammer, A., Kirchhoff, P.D., Jiang, X., Venkatachalam, C.M. and Waldman, M. (2005) LigScore: a novel scoring function for predicting binding affinities. *J Mol Graph Model*, **23**, 395-407.
78. Muegge, I. (2006) PMF scoring revisited. *J Med Chem*, **49**, 5895-5902.
79. Warschawski, D.E., Arnold, A.A., Beaugrand, M., Gravel, A., Chartrand, E. and Marcotte, I. (2011) Choosing membrane mimetics for NMR structural studies of transmembrane proteins. *Biochim. Biophys. Acta*, **1808**, 1957-1974.
80. Coey, A.T., Sahu, I.D., Gunasekera, T.S., Troxel, K.R., Hawn, J.M., Swartz, M.S., Wickenheiser, M.R., Reid, R.J., Welch, R.C., Vanoye, C.G. *et al.* (2011) Reconstitution of KCNE1 into lipid bilayers: comparing the structural, dynamic, and activity differences in micelle and vesicle environments. *Biochemistry*, **50**, 10851-10859.
81. Barth, P., Wallner, B. and Baker, D. (2009) Prediction of membrane protein structures with complex topologies using limited constraints. *Proc. Natl. Acad. Sci. USA*, **106**, 1409-1414.
82. Schneidman-Duhovny, D., Inbar, Y., Nussinov, R. and Wolfson, H.J. (2005) PatchDock and SymmDock: servers for rigid and symmetric docking. *Nucleic Acids Res.*, **33**, W363-367.
83. Ashkenazy, H., Erez, E., Martz, E., Pupko, T. and Ben-Tal, N. (2010) ConSurf 2010: calculating evolutionary conservation in sequence and structure of proteins and nucleic acids. *Nucleic Acids Res*, **38 Suppl**, W529-533.
84. Sayers, E.W., Barrett, T., Benson, D.A., Bolton, E., Bryant, S.H., Canese, K., Chetvernin, V., Church, D.M., DiCuccio, M., Federhen, S. *et al.* (2011) Database resources of the National Center for Biotechnology Information. *Nucleic Acids Res*, **39**, D38-51.
85. Altschul, S.F., Madden, T.L., Schaffer, A.A., Zhang, J., Zhang, Z., Miller, W. and Lipman, D.J. (1997) Gapped BLAST and PSI-BLAST: a new generation of protein database search programs. *Nucleic Acids Res*, **25**, 3389-3402.
86. Edgar, R.C. (2004) MUSCLE: multiple sequence alignment with high accuracy and high throughput. *Nucleic Acids Res*, **32**, 1792-1797.
87. Wang, C., Bradley, P. and Baker, D. (2007) Protein-protein docking with backbone flexibility. *J. Mol. Biol.*, **373**, 503-519.
88. Tovchigrechko, A. and Vakser, I.A. (2006) GRAMM-X public web server for protein-protein docking. *Nucleic Acids Res.*, **34**, W310-314.
89. Xu, X., Jiang, M., Hsu, K.L., Zhang, M. and Tseng, G.N. (2008) KCNQ1 and KCNE1 in the IKs channel complex make state-dependent contacts in their extracellular domains. *J. Gen. Physiol.*, **131**, 589-603.
90. Chung, D.Y., Chan, P.J., Bankston, J.R., Yang, L., Liu, G., Marx, S.O., Karlin, A. and Kass, R.S. (2009) Location of KCNE1 relative to KCNQ1 in the I(KS) potassium channel by disulfide cross-linking of substituted cysteines. *Proc. Natl. Acad. Sci. USA*, **106**, 743-748.
91. Wang, Y.H., Jiang, M., Xu, X.L., Hsu, K.L., Zhang, M. and Tseng, G.N. (2010) Gating-related molecular motions in the extracellular domain of the I(Ks) channel: implications for I (Ks) channelopathy. *J. Membr. Biol.*, **239**, 137-156.
92. Careaga, C.L. and Falke, J.J. (1992) Thermal motions of surface alpha-helices in the D-galactose chemosensory receptor. Detection by disulfide trapping. *J. Mol. Biol.*, **226**, 1219-1235.
93. Glaser, F., Steinberg, D.M., Vakser, I.A. and Ben-Tal, N. (2001) Residue frequencies and pairing preferences at protein-protein interfaces. *Proteins*, **43**, 89-102.

94. Jones, D.T. (1999) Protein secondary structure prediction based on position-specific scoring matrices. *J Mol Biol*, **292**, 195-202.
95. Nugent, T. and Jones, D.T. (2009) Transmembrane protein topology prediction using support vector machines. *BMC Bioinformatics*, **10**, 159.
96. Tusnady, G.E. and Simon, I. (1998) Principles governing amino acid composition of integral membrane proteins: application to topology prediction. *J Mol Biol*, **283**, 489-506.
97. Jaroszewski, L., Rychlewski, L., Li, Z., Li, W. and Godzik, A. (2005) FFAS03: a server for profile--profile sequence alignments. *Nucleic Acids Res*, **33**, W284-288.
98. Hildebrand, A., Remmert, M., Biegert, A. and Soding, J. (2009) Fast and accurate automatic structure prediction with HHpred. *Proteins*, **77 Suppl 9**, 128-132.
99. Boeckmann, B., Bairoch, A., Apweiler, R., Blatter, M.C., Estreicher, A., Gasteiger, E., Martin, M.J., Michoud, K., O'Donovan, C., Phan, I. *et al.* (2003) The SWISS-PROT protein knowledgebase and its supplement TrEMBL in 2003. *Nucleic Acids Res*, **31**, 365-370.
100. Biegert, A. and Soding, J. (2009) Sequence context-specific profiles for homology searching. *Proc Natl Acad Sci U S A*, **106**, 3770-3775.
101. Eswar, N., Webb, B., Marti-Renom, M.A., Madhusudhan, M.S., Eramian, D., Shen, M.Y., Pieper, U. and Sali, A. (2006) Comparative protein structure modeling using Modeller. *Curr Protoc Bioinformatics*, **Chapter 5**, Unit 5 6.
102. Canutescu, A.A. and Dunbrack, R.L., Jr. (2003) Cyclic coordinate descent: A robotics algorithm for protein loop closure. *Protein Sci*, **12**, 963-972.
103. Yeheskel, A., Haliloglu, T. and Ben-Tal, N. (2010) Independent and cooperative motions of the Kv1.2 channel: voltage sensing and gating. *Biophys. J.*, **98**, 2179-2188.
104. Haliloglu, T. and Ben-Tal, N. (2008) Cooperative transition between open and closed conformations in potassium channels. *PLoS Comput. Biol.*, **4**, e1000164.
105. Shrivastava, I.H. and Bahar, I. (2006) Common mechanism of pore opening shared by five different potassium channels. *Biophys. J.*, **90**, 3929-3940.
106. Bahar, I., Lezon, T.R., Bakan, A. and Shrivastava, I.H. (2010) Normal mode analysis of biomolecular structures: functional mechanisms of membrane proteins. *Chem. Rev.*, **110**, 1463-1497.
107. Bahar, I., Atilgan, A.R. and Erman, B. (1997) Direct evaluation of thermal fluctuations in proteins using a single-parameter harmonic potential. *Fold. Des.*, **2**, 173-181.
108. Haliloglu, T., Bahar, I. and Erman, B. (1997) Gaussian dynamics of folded proteins. *Phys. Rev. Lett.*, **79**, 3090.
109. Atilgan, A.R., Durell, S.R., Jernigan, R.L., Demirel, M.C., Keskin, O. and Bahar, I. (2001) Anisotropy of fluctuation dynamics of proteins with an elastic network model. *Biophys. J.*, **80**, 505-515.
110. Emekli, U., Schneidman-Duhovny, D., Wolfson, H.J., Nussinov, R. and Haliloglu, T. (2008) HingeProt: automated prediction of hinges in protein structures. *Proteins*, **70**, 1219-1227.
111. Bahar, I. and Rader, A.J. (2005) Coarse-grained normal mode analysis in structural biology. *Curr. Opin. Struct. Biol.*, **15**, 586-592.
112. Peretz, A., Sheinin, A., Yue, C., Degani-Katzav, N., Gibor, G., Nachman, R., Gopin, A., Tam, E., Shabat, D., Yaari, Y. *et al.* (2007) Pre- and postsynaptic activation of M-channels by a novel opener dampens neuronal firing and transmitter release. *J Neurophysiol*, **97**, 283-295.

113. Gibor, G., Yakubovich, D., Rosenhouse-Dantsker, A., Peretz, A., Schottelndreier, H., Seebohm, G., Dascal, N., Logothetis, D.E., Paas, Y. and Attali, B. (2007) An inactivation gate in the selectivity filter of KCNQ1 potassium channels. *Biophys. J.*, **93**, 4159-4172.
114. Rees, D.C., DeAntonio, L. and Eisenberg, D. (1989) Hydrophobic organization of membrane proteins. *Science*, **245**, 510-513.
115. von Heijne, G. (2006) Membrane-protein topology. *Nat Rev Mol Cell Biol*, **7**, 909-918.
116. Dedek, K., Kunath, B., Kananura, C., Reuner, U., Jentsch, T.J. and Steinlein, O.K. (2001) Myokymia and neonatal epilepsy caused by a mutation in the voltage sensor of the KCNQ2 K+ channel. *Proc Natl Acad Sci U S A*, **98**, 12272-12277.
117. Wuttke, T.V., Jurkat-Rott, K., Paulus, W., Garncarek, M., Lehmann-Horn, F. and Lerche, H. (2007) Peripheral nerve hyperexcitability due to dominant-negative KCNQ2 mutations. *Neurology*, **69**, 2045-2053.
118. Miraglia del Giudice, E., Coppola, G., Scuccimarra, G., Cirillo, G., Bellini, G. and Pascotto, A. (2000) Benign familial neonatal convulsions (BFNC) resulting from mutation of the KCNQ2 voltage sensor. *Eur J Hum Genet*, **8**, 994-997.
119. Schroeder, B.C., Kubisch, C., Stein, V. and Jentsch, T.J. (1998) Moderate loss of function of cyclic-AMP-modulated KCNQ2/KCNQ3 K+ channels causes epilepsy. *Nature*, **396**, 687-690.
120. Singh, N.A., Westenskow, P., Charlier, C., Pappas, C., Leslie, J., Dillon, J., Anderson, V.E., Sanguinetti, M.C. and Leppert, M.F. (2003) KCNQ2 and KCNQ3 potassium channel genes in benign familial neonatal convulsions: expansion of the functional and mutation spectrum. *Brain*, **126**, 2726-2737.
121. Dedek, K., Fusco, L., Teloy, N. and Steinlein, O.K. (2003) Neonatal convulsions and epileptic encephalopathy in an Italian family with a missense mutation in the fifth transmembrane region of KCNQ2. *Epilepsy Res*, **54**, 21-27.
122. Curran, A.R. and Engelman, D.M. (2003) Sequence motifs, polar interactions and conformational changes in helical membrane proteins. *Curr Opin Struct Biol*, **13**, 412-417.
123. Senes, A., Gerstein, M. and Engelman, D.M. (2000) Statistical analysis of amino acid patterns in transmembrane helices: the GxxxG motif occurs frequently and in association with beta-branched residues at neighboring positions. *J Mol Biol*, **296**, 921-936.
124. Peretz, A., Degani, N., Nachman, R., Uziyel, Y., Gibor, G., Shabat, D. and Attali, B. (2005) Meclofenamic acid and diclofenac, novel templates of KCNQ2/Q3 potassium channel openers, depress cortical neuron activity and exhibit anticonvulsant properties. *Mol Pharmacol*, **67**, 1053-1066.
125. Lange, W., Geissendorfer, J., Schenzer, A., Grotzinger, J., Seebohm, G., Friedrich, T. and Schwake, M. (2009) Refinement of the binding site and mode of action of the anticonvulsant Retigabine on KCNQ K+ channels. *Mol Pharmacol*, **75**, 272-280.
126. Schenzer, A., Friedrich, T., Pusch, M., Saftig, P., Jentsch, T.J., Grotzinger, J. and Schwake, M. (2005) Molecular determinants of KCNQ (Kv7) K+ channel sensitivity to the anticonvulsant retigabine. *J Neurosci*, **25**, 5051-5060.
127. Wuttke, T.V., Seebohm, G., Bail, S., Maljevic, S. and Lerche, H. (2005) The new anticonvulsant retigabine favors voltage-dependent opening of the Kv7.2 (KCNQ2) channel by binding to its activation gate. *Mol Pharmacol*, **67**, 1009-1017.
128. Xiong, Q., Sun, H. and Li, M. (2007) Zinc pyrithione-mediated activation of voltage-gated KCNQ potassium channels rescues epileptogenic mutants. *Nat Chem Biol*, **3**, 287-296.

129. Bahar, I. (2010) On the functional significance of soft modes predicted by coarse-grained models for membrane proteins. *J. Gen. Physiol.*, **135**, 563-573.
130. Flynn, G.E. and Zagotta, W.N. (2001) Conformational changes in S6 coupled to the opening of cyclic nucleotide-gated channels. *Neuron*, **30**, 689-698.
131. Flynn, G.E. and Zagotta, W.N. (2003) A cysteine scan of the inner vestibule of cyclic nucleotide-gated channels reveals architecture and rearrangement of the pore. *J Gen Physiol*, **121**, 563-582.
132. Mazzolini, M., Anselmi, C. and Torre, V. (2009) The analysis of desensitizing CNGA1 channels reveals molecular interactions essential for normal gating. *J Gen Physiol*, **133**, 375-386.
133. Nishiguchi, K.M., Sandberg, M.A., Gorji, N., Berson, E.L. and Dryja, T.P. (2005) Cone cGMP-gated channel mutations and clinical findings in patients with achromatopsia, macular degeneration, and other hereditary cone diseases. *Hum Mutat*, **25**, 248-258.
134. Wissinger, B., Gamer, D., Jagle, H., Giorda, R., Marx, T., Mayer, S., Tippmann, S., Broghammer, M., Jurklies, B., Rosenberg, T. *et al.* (2001) CNGA3 mutations in hereditary cone photoreceptor disorders. *Am J Hum Genet*, **69**, 722-737.
135. Lee, S.Y., Banerjee, A. and MacKinnon, R. (2009) Two separate interfaces between the voltage sensor and pore are required for the function of voltage-dependent K(+) channels. *PLoS Biol*, **7**, e47.
136. Faillace, M.P., Bernabeu, R.O. and Korenbrot, J.I. (2004) Cellular processing of cone photoreceptor cyclic GMP-gated ion channels: a role for the S4 structural motif. *J Biol Chem*, **279**, 22643-22653.
137. Miceli, F., Soldovieri, M.V., Hernandez, C.C., Shapiro, M.S., Annunziato, L. and Taglialatela, M. (2008) Gating consequences of charge neutralization of arginine residues in the S4 segment of K(v)7.2, an epilepsy-linked K+ channel subunit. *Biophys J*, **95**, 2254-2264.
138. Johnson, D.M., Garrett, E.M., Rutter, R., Bonnert, T.P., Gao, Y.D., Middleton, R.E. and Sutton, K.G. (2006) Functional mapping of the transient receptor potential vanilloid 1 intracellular binding site. *Mol Pharmacol*, **70**, 1005-1012.
139. Padilla, K., Wickenden, A.D., Gerlach, A.C. and McCormack, K. (2009) The KCNQ2/3 selective channel opener ICA-27243 binds to a novel voltage-sensor domain site. *Neurosci Lett*, **465**, 138-142.
140. Tiwari-Woodruff, S.K., Lin, M.A., Schulteis, C.T. and Papazian, D.M. (2000) Voltage-dependent structural interactions in the Shaker K(+) channel. *J Gen Physiol*, **115**, 123-138.
141. Nimigean, C.M., Shane, T. and Miller, C. (2004) A cyclic nucleotide modulated prokaryotic K+ channel. *J. Gen. Physiol.*, **124**, 203-210.
142. Nakajo, K. and Kubo, Y. (2011) Nano-environmental changes by KCNE proteins modify KCNQ channel function. *Channels (Austin)*, **5**, 397-401.
143. Kessel, A. and Ben-Tal, N. (2010) *Introduction to Proteins: Structure, Function and Motion.* CRC Press, Boca Raton.
144. Burley, S.K. and Petsko, G.A. (1985) Aromatic-aromatic interaction: a mechanism of protein structure stabilization. *Science*, **229**, 23-28.
145. Cordero-Morales, J.F., Cuello, L.G., Zhao, Y., Jogini, V., Cortes, D.M., Roux, B. and Perozo, E. (2006) Molecular determinants of gating at the potassium-channel selectivity filter. *Nat. Struct. Mol. Biol.*, **13**, 311-318.

146. Cordero-Morales, J.F., Jogini, V., Lewis, A., Vasquez, V., Cortes, D.M., Roux, B. and Perozo, E. (2007) Molecular driving forces determining potassium channel slow inactivation. *Nat. Struct. Mol. Biol.*, **14**, 1062-1069.
147. Chakrapani, S., Cordero-Morales, J.F., Jogini, V., Pan, A.C., Cortes, D.M., Roux, B. and Perozo, E. (2011) On the structural basis of modal gating behavior in K(+) channels. *Nat. Struct. Mol. Biol.*, **18**, 67-74.
148. Cuello, L.G., Jogini, V., Cortes, D.M., Pan, A.C., Gagnon, D.G., Dalmas, O., Cordero-Morales, J.F., Chakrapani, S., Roux, B. and Perozo, E. (2010) Structural basis for the coupling between activation and inactivation gates in K(+) channels. *Nature*, **466**, 272-275.
149. McCoy, J.G. and Nimigean, C.M. (2012) Structural correlates of selectivity and inactivation in potassium channels. *Biochim. Biophys. Acta*, **1818**, 272-285.
150. Pusch, M., Magrassi, R., Wollnik, B. and Conti, F. (1998) Activation and inactivation of homomeric KvLQT1 potassium channels. *Biophys. J.*, **75**, 785-792.
151. Tristani-Firouzi, M. and Sanguinetti, M.C. (1998) Voltage-dependent inactivation of the human K+ channel KvLQT1 is eliminated by association with minimal K+ channel (minK) subunits. *J. Physiol.*, **510**, 37-45.
152. Abitbol, I., Peretz, A., Lerche, C., Busch, A.E. and Attali, B. (1999) Stilbenes and fenamates rescue the loss of I(KS) channel function induced by an LQT5 mutation and other IsK mutants. *EMBO J.*, **18**, 4137-4148.
153. Melman, Y.F., Um, S.Y., Krumerman, A., Kagan, A. and McDonald, T.V. (2004) KCNE1 binds to the KCNQ1 pore to regulate potassium channel activity. *Neuron*, **42**, 927-937.
154. Seebohm, G., Sanguinetti, M.C. and Pusch, M. (2003) Tight coupling of rubidium conductance and inactivation in human KCNQ1 potassium channels. *J. Physiol.*, **552**, 369-378.
155. Shimizu, H., Iwamoto, M., Konno, T., Nihei, A., Sasaki, Y.C. and Oiki, S. (2008) Global twisting motion of single molecular KcsA potassium channel upon gating. *Cell*, **132**, 67-78.
156. Valadie, H., Lacapcre, J.J., Sanejouand, Y.H. and Etchebest, C. (2003) Dynamical properties of the MscL of Escherichia coli: a normal mode analysis. *J. Mol. Biol.*, **332**, 657-674.
157. Seebohm, G., Westenskow, P., Lang, F. and Sanguinetti, M.C. (2005) Mutation of colocalized residues of the pore helix and transmembrane segments S5 and S6 disrupt deactivation and modify inactivation of KCNQ1 K+ channels. *J. Physiol.*, **563**, 359-368.
158. Westenskow, P., Splawski, I., Timothy, K.W., Keating, M.T. and Sanguinetti, M.C. (2004) Compound mutations: a common cause of severe long-QT syndrome. *Circulation*, **109**, 1834-1841.
159. Bhate, M.P., Wylie, B.J., Tian, L. and McDermott, A.E. (2010) Conformational dynamics in the selectivity filter of KcsA in response to potassium ion concentration. *J Mol Biol*, **401**, 155-166.
160. Panaghie, G., Purtell, K., Tai, K.K. and Abbott, G.W. (2008) Voltage-dependent C-type inactivation in a constitutively open K+ channel. *Biophys. J.*, **95**, 2759-2778.
161. Panaghie, G., Tai, K.K. and Abbott, G.W. (2006) Interaction of KCNE subunits with the KCNQ1 K+ channel pore. *J. Physiol.*, **570**, 455-467.
162. Swartz, K.J. (2004) Towards a structural view of gating in potassium channels. *Nat Rev Neurosci*, **5**, 905-916.

163. Hibino, H., Inanobe, A., Furutani, K., Murakami, S., Findlay, I. and Kurachi, Y. (2010) Inwardly rectifying potassium channels: their structure, function, and physiological roles. *Physiol Rev*, **90**, 291-366.
164. Bavro, V.N., De Zorzi, R., Schmidt, M.R., Muniz, J.R., Zubcevic, L., Sansom, M.S., Venien-Bryan, C. and Tucker, S.J. (2012) Structure of a KirBac potassium channel with an open bundle crossing indicates a mechanism of channel gating. *Nat Struct Mol Biol*, **19**, 158-163.
165. Clarke, O.B., Caputo, A.T., Hill, A.P., Vandenberg, J.I., Smith, B.J. and Gulbis, J.M. (2010) Domain reorientation and rotation of an intracellular assembly regulate conduction in Kir potassium channels. *Cell*, **141**, 1018-1029.
166. Giorgetti, A., Nair, A.V., Codega, P., Torre, V. and Carloni, P. (2005) Structural basis of gating of CNG channels. *FEBS Lett*, **579**, 1968-1972.
167. Flynn, G.E., Johnson, J.P., Jr. and Zagotta, W.N. (2001) Cyclic nucleotide-gated channels: shedding light on the opening of a channel pore. *Nat Rev Neurosci*, **2**, 643-651.
168. Mazzolini, M., Marchesi, A., Giorgetti, A. and Torre, V. (2010) Gating in CNGA1 channels. *Pflugers Arch*, **459**, 547-555.
169. Nair, A.V., Nguyen, C.H. and Mazzolini, M. (2009) Conformational rearrangements in the S6 domain and C-linker during gating in CNGA1 channels. *Eur Biophys J*, **38**, 993-1002.
170. Nair, A.V., Anselmi, C. and Mazzolini, M. (2009) Movements of native C505 during channel gating in CNGA1 channels. *Eur Biophys J*, **38**, 465-478.
171. Johnson, S., Michaelides, M., Aligianis, I.A., Ainsworth, J.R., Mollon, J.D., Maher, E.R., Moore, A.T. and Hunt, D.M. (2004) Achromatopsia caused by novel mutations in both CNGA3 and CNGB3. *J Med Genet*, **41**, e20.
172. Liu, C. and Varnum, M.D. (2005) Functional consequences of progressive cone dystrophy-associated mutations in the human cone photoreceptor cyclic nucleotide-gated channel CNGA3 subunit. *Am J Physiol Cell Physiol*, **289**, C187-198.
173. Kohl, S., Marx, T., Giddings, I., Jagle, H., Jacobson, S.G., Apfelstedt-Sylla, E., Zrenner, E., Sharpe, L.T. and Wissinger, B. (1998) Total colourblindness is caused by mutations in the gene encoding the alpha-subunit of the cone photoreceptor cGMP-gated cation channel. *Nat Genet*, **19**, 257-259.
174. Duricka, D.L., Brown, R.L. and Varnum, M.D. (2012) Defective trafficking of cone photoreceptor CNG channels induces the unfolded protein response and ER-stress-associated cell death. *Biochem J*, **441**, 685-696.
175. Kohl, S., Varsanyi, B., Antunes, G.A., Baumann, B., Hoyng, C.B., Jagle, H., Rosenberg, T., Kellner, U., Lorenz, B., Salati, R. *et al.* (2005) CNGB3 mutations account for 50% of all cases with autosomal recessive achromatopsia. *Eur J Hum Genet*, **13**, 302-308.
176. Kohl, S., Baumann, B., Broghammer, M., Jagle, H., Sieving, P., Kellner, U., Spegal, R., Anastasi, M., Zrenner, E., Sharpe, L.T. *et al.* (2000) Mutations in the CNGB3 gene encoding the beta-subunit of the cone photoreceptor cGMP-gated channel are responsible for achromatopsia (ACHM3) linked to chromosome 8q21. *Hum Mol Genet*, **9**, 2107-2116.
177. Napolitano, C., Priori, S.G., Schwartz, P.J., Bloise, R., Ronchetti, E., Nastoli, J., Bottelli, G., Cerrone, M. and Leonardi, S. (2005) Genetic testing in the long QT syndrome: development and validation of an efficient approach to genotyping in clinical practice. *JAMA*, **294**, 2975-2980.
178. Choi, G., Kopplin, L.J., Tester, D.J., Will, M.L., Haglund, C.M. and Ackerman, M.J. (2004) Spectrum and frequency of cardiac channel defects in swimming-triggered arrhythmia syndromes. *Circulation*, **110**, 2119-2124.

179. Tester, D.J., Will, M.L., Haglund, C.M. and Ackerman, M.J. (2005) Compendium of cardiac channel mutations in 541 consecutive unrelated patients referred for long QT syndrome genetic testing. *Heart Rhythm*, **2**, 507-517.
180. Donger, C., Denjoy, I., Berthet, M., Neyroud, N., Cruaud, C., Bennaceur, M., Chivoret, G., Schwartz, K., Coumel, P. and Guicheney, P. (1997) KVLQT1 C-terminal missense mutation causes a forme fruste long-QT syndrome. *Circulation*, **96**, 2778-2781.
181. Tanaka, T., Nagai, R., Tomoike, H., Takata, S., Yano, K., Yabuta, K., Haneda, N., Nakano, O., Shibata, A., Sawayama, T. *et al.* (1997) Four novel KVLQT1 and four novel HERG mutations in familial long-QT syndrome. *Circulation*, **95**, 565-567.
182. Chouabe, C., Neyroud, N., Guicheney, P., Lazdunski, M., Romey, G. and Barhanin, J. (1997) Properties of KvLQT1 K+ channel mutations in Romano-Ward and Jervell and Lange-Nielsen inherited cardiac arrhythmias. *EMBO J*, **16**, 5472-5479.
183. Chen, S., Zhang, L., Bryant, R.M., Vincent, G.M., Flippin, M., Lee, J.C., Brown, E., Zimmerman, F., Rozich, R., Szafranski, P. *et al.* (2003) KCNQ1 mutations in patients with a family history of lethal cardiac arrhythmias and sudden death. *Clin Genet*, **63**, 273-282.
184. Shimizu, W., Horie, M., Ohno, S., Takenaka, K., Yamaguchi, M., Shimizu, M., Washizuka, T., Aizawa, Y., Nakamura, K., Ohe, T. *et al.* (2004) Mutation site-specific differences in arrhythmic risk and sensitivity to sympathetic stimulation in the LQT1 form of congenital long QT syndrome: multicenter study in Japan. *J Am Coll Cardiol*, **44**, 117-125.
185. Wang, Q., Curran, M.E., Splawski, I., Burn, T.C., Millholland, J.M., VanRaay, T.J., Shen, J., Timothy, K.W., Vincent, G.M., de Jager, T. *et al.* (1996) Positional cloning of a novel potassium channel gene: KVLQT1 mutations cause cardiac arrhythmias. *Nat Genet*, **12**, 17-23.
186. van den Berg, M.H., Wilde, A.A., Robles de Medina, E.O., Meyer, H., Geelen, J.L., Jongbloed, R.J., Wellens, H.J. and Geraedts, J.P. (1997) The long QT syndrome: a novel missense mutation in the S6 region of the KVLQT1 gene. *Hum Genet*, **100**, 356-361.
187. Itoh, T., Tanaka, T., Nagai, R., Kikuchi, K., Ogawa, S., Okada, S., Yamagata, S., Yano, K., Yazaki, Y. and Nakamura, Y. (1998) Genomic organization and mutational analysis of KVLQT1, a gene responsible for familial long QT syndrome. *Hum Genet*, **103**, 290-294.
188. Deschenes, D., Acharfi, S., Pouliot, V., Hegele, R., Krahn, A., Daleau, P. and Chahine, M. (2003) Biophysical characteristics of a new mutation on the KCNQ1 potassium channel (L251P) causing long QT syndrome. *Can J Physiol Pharmacol*, **81**, 129-134.
189. Whorton, M.R. and MacKinnon, R. (2011) Crystal structure of the mammalian GIRK2 K+ channel and gating regulation by G proteins, PIP2, and sodium. *Cell*, **147**, 199-208.
190. Yuan, P., Leonetti, M.D., Hsiung, Y. and MacKinnon, R. (2012) Open structure of the Ca2+ gating ring in the high-conductance Ca2+-activated K+ channel. *Nature*, **481**, 94-97.
191. Lomize, M.A., Lomize, A.L., Pogozheva, I.D. and Mosberg, H.I. (2006) OPM: orientations of proteins in membranes database. *Bioinformatics*, **22**, 623-625.

תקציר

משפחת העל של תעלות יוניות תלויות מתח ודומותיהן היא אחת הקבוצות הגדולות של חלבונים המעורבים בהולכת אותות. כל נציג של משפחת העל מכיל מתחם יחודי המשמש להולכת יונים באופן סלקטיבי. חלק מהתעלות במשפחה מכילות מתחמי בקרה שונים אשר מגיבים לשינויים במתח הממברנלי, שינויים בריכוז של מולקולות קטנות שונות או גירויים אחרים. בנוסף, הפעילות של התעלות היוניות יכולה לעבור וויסות על ידי חלבוני בקרה. מנגנוני המודולציה של התעלות היוניות נחקרים רבות על מנת להבין את העקרונות הבסיסיים של תהליכים אלה. יתרה מזאת, מנגנוני המודולוציה נחקרים על מנת לסייע בפיתוח תרופות שיעזרו להתגבר על תפקוד לקוי של התעלות במחלות. במהלך המחקר התמקדתי בשתי משפחות של תעלות יוניות: תעלות אשלגן תלויות מתח ותעלות יוניות תלויות נוקליאוטידים ציקליים. בפרויקט הראשון חקרתי תעלת אשלגן תלוית מתח הקרויה Kv7.2 ומבוטאת בעיקר בנוירונים. לתעלה זו תפקיד חשוב בבקרת האקסיטביליות של הנוירונים; מולקולות קטנות אשר מגבירות את פעילותה מפותחות כיום כתרופות פוטנציאליות לטיפול במחלת הנפילה ובכאב. במסגרת המחקר מידלתי מבנה תלת מימדי של המתחם הממברנלי של התעלה וביצעתי חישובי דוקינג של מולקולה משפעלת קטנה הנקראת NH29 לתוך המודל המבני של Kv7.2 שיצרתי. מודל האינטראקציה החישובי בין NH29 ו Kv7.2 אושש בניסויים. כמן כן, הצעתי אינטראקציות הגורמות לשפעול התעלה על ידי המולקולה הקטנה. בפרויקט נוסף חקרתי את האינטארקציה בין התעלה ההומנית Kv7.1 וחלבון הבקרה שלה KCNE1. Kv7.1 גם היא תעלת אשלגן תלוית מתח, והיקשרות של KNCE1 משנה את פעילותה בצורה משמעותית. מידלתי מבנה תלת מימדי של הקומפלקס והראתי שהוא מתאים ניסויי מיפוי בעזרת קשרים דיסולפידים. על סמך המודל הצעתי פרשנות של הנתונים האלקטרופיזיולוגיים של שני מוטנטים של KCNE1 אשר עוצבו בכדי לבחון את המודל המבני של הקומפלקס. בנוסף, ביצעתי אנליזה של תנודות של Kv7.1 בהיעדר

ובנוכחות של KCNE1 בעזרת מודלים של רשתות אלסטיות. הצעתי מנגנונים אפשריים אשר מסבירים את ההשפעות הידועות של KCNE1 על הפעילות של Kv7.1. בפרוייקט נוסף, מידלתי מבנה תלת מימדי של תעלה הומנית תלוית נוקליאוטידים ציקליים המבוטאת בתאי מדוך. מוטציות בתעלה זו גורמות לאקרומטופסיה המאופיינת בעיוורון צבעים, רגישות לסינוור, ניסטגמוס וירידה בחדות הראיה. השתמשתי במודל המבני על מנת להציע הסבר מולקולרי למוטציות הגורמות מחלה. כמו כן, חקרתי תנועות גלובליות של התעלה בעזרת מודלים של רשתות אלסטיות. האנליזה גילתה ממצאים מעניינים אודות מנגנוני הפתיחה של התעלה.

עבודה זו נעשתה בהדרכת

פרופ' ניר בן טל

אוניברסיטת תל אביב

Tel-Aviv University

מחקר חישובי של תעלות יוניות הומניות נבחרות

חיבור לשם קבלת התואר "דוקטור לפילוסופיה"

מאת יאנה גופמן

הוגש לסנאט אוניברסיטת תל אביב

מאי 2012